Study of tunable narrow-band THz and high-intensity channeling radiation sources with a 50 MeV class photo-injector

JIBONG HYUN

Doctor of Philosophy

Department of Accelerator Science
School of High Energy Accelerator Science
The Graduate University for Advanced Studies,
SOKENDAI

SOKENDAI
(The Graduate University for Advanced Studies)

Study of tunable narrow-band THz and high-intensity channeling radiation sources with a 50 MeV class photo-injector

by

Jibong Hyun

A thesis submitted in partial fulfillment for the
degree of Doctor of Philosophy

in the
School of High Energy Accelerator Science
Department of Accelerator Science

December 2018

Declaration of Authorship

I, Jibong Hyun, declare that this thesis titled, 'Study of tunable narrow-band THz and high-intensity channeling radiation sources with a 50 MeV class photo-injector' and the work presented in it are my own. I confirm that:

- This work was done wholly or mainly while in candidature for a research degree at this University.
- Where any part of this thesis has previously been submitted for a degree or any other qualification at this University or any other institution, this has been clearly stated.
- Where I have consulted the published work of others, this is always clearly attributed.
- Where I have quoted from the work of others, the source is always given. With the exception of such quotations, this thesis is entirely my own work.
- I have acknowledged all main sources of help.
- Where the thesis is based on work done by myself jointly with others, I have made clear exactly what was done by others and what I have contributed myself.

Signed: Hyun Ji Bong

Date: 12/10/2018

SOKENDAI
(The Graduate University for Advanced Studies)

Abstract

School of High Energy Accelerator Science
Department of Accelerator Science

Doctor of Philosophy

by Jibong Hyun

This thesis describes the generation of frequency tunable narrow-band THz radiation and energy tunable quasi-monochromatic hard X-rays using a 50 MeV class photo-injector. We produce micro-bunched beams using a slit-mask and a chicane and then generate THz radiation by sending them to a metallic foil or passing through a small wiggler. As for hard-X-ray generation, we employ channeling radiation (CR) which can emit quasi-monochromatic hard X-rays with a single crystal and an electron beam with an energy of below 100 MeV. We performed each demonstration experiment to verify the theory and simulations at the FAST (Fermi Accelerator Science and Technology) facility in Fermilab. The results of the experiments on the micro-bunching were in agreement with those of the theory and simulations. On the other hand, the expected energy spectrum could not be obtained due to the pile-up of the detectors. We performed particle tracking simulations with GEANT4 and identified that the X-ray detectors measured bremsstrahlung radiated from beam pipe caused by the dark currents from the photo cathode, and also detected the characteristic X-rays of lead around the detectors emitted by the bremsstrahlung. In this thesis, the details on the theory, the simulation results, the experiment results of THz/CR are described, and the suggestions for the next experiments through the considerations are also shown.

Acknowledgements

This doctoral thesis would not be completed without support and help from wonderful peoples at Fermi National Accelerator Laboratory (FNAL) and High Energy Accelerator Research Organization/SOKENDAI (KEK/SOKENDAI).

First and foremost, I am grateful to my dear supervisor Dr. Tanaji Sen at FNAL for accepting me as a visiting graduate student and for his advice, support, encouragement for three years. He led me in the right direction when I faced with a serious dilemma and also led me to correct understandings of beam physics through useful discussions with him.

I would like to thank Prof. Philippe Piot at Northern Illinois University (NIU) for helping me with ELEGANT, ASTRA, IMPACT-T codes and supporting me in simulations and experiments. He accurately answered everything whenever I asked him on beam physics, experimental methods, and computer programming.

My sincere thanks to Dr. Charles Thangaraj, Dr. Randy Thrman-Keup, and Dr. Alex Lumpkin for useful discussions in experiments and simulations on micro-bunched beams. I discussed with Charles micro-bunched beam production and the detection. THz radiation was measured using a Martin-Puplett interferometer with a pyrometer designed and assembled by Randy. I tried to measure micro-bunched beams with a streak camera with Alex.

The experiments could not be performed without the machine commissioning. I wish to express my thank to the FAST commissioning group, Dr. Jamie Santucci, Dr. Darren Crawford, Dr. Dean (chip) Edstrom Jr., Dr. Jinhao Ruan, Dr. Alexander Romanov, and Dr. Daniel Broemmelsiek for their contribution to the FAST operation. I also discussed with Jinhao simulation results and the machine time before and during the experiments. I would like to thank Dr. Daniel Mihalcea for the useful discussion on simulation results of CR and THz radiation and also helped me with IMPACT-T code. GEANT4 applications for electron channeling was supplied by Dr. E. Bagli (INFN).

I am very thankful to Dr. Vladimir Shiltsev, Dr. Alexander Valishev, and Dr. Sergei Nagaitsev for your cooperation and understanding of my experiments at the FAST injector.

I would like to thank Prof. Nobukazu Toge, Assoc. prof. Mitsuhiro Yoshida, and Assoc. prof. Masanori Satoh, and Dr. Takuya Natsui for useful discussions and advice. I am grateful to Dr. Zhang Rui and Dr. Kazama Shingo for recommending me to go abroad to study beam physics. I was able to have an enjoyable student life (hiking, table tennis,

soccer, Food Party, BBQ, traveling...) thanks to my best friends, Akira Inoue, Daisuke Satoh, Shibuya Tatsunori, Moriai Yasuaki, Shohei Otsuki, Hayato Okamoto, and Yoshito Saito.

This doctoral study was supported by "The Short-Stay Study Abroad Program" and "INTERNSHIP-PROGRAM IN 2017" from SOKENDAI and by Fermi Research Alliance, LLC under Contract No. DE-AC02-07CH11359 with the U.S. Department of Energy, Office of Science, Office of High Energy Physics.

Contents

Declaration of Authorship i

Abstract ii

Acknowledgements iii

List of Figures viii

List of Tables xi

Abbreviations xii

1 Introduction 1
- 1.1 THz radiation . . . 2
- 1.2 Channeling radiation . . . 4

2 Beam dynamics 6
- 2.1 Equation of Motion of a charged particle . . . 6
- 2.2 Transfer matrices . . . 7
  - 2.2.1 Drift space . . . 8
  - 2.2.2 Quadrupole magnet . . . 8
  - 2.2.3 Dipole magnet . . . 9
    - 2.2.3.1 Sector magnet . . . 9
    - 2.2.3.2 Rectangular magnet . . . 10
- 2.3 Beam matrices . . . 10
- 2.4 Phase space ellipse . . . 11
  - 2.4.1 Twiss parameters α, β, and γ . . . 11
  - 2.4.2 Beam emittance . . . 12
    - 2.4.2.1 Two dimensional beam emittance . . . 12
    - 2.4.2.2 Four dimensional beam emittance . . . 13

3 Accelerator Facility for experiments 14
- 3.1 FAST Photoinjector . . . 15

4 Magnetic chicane 19

4.1 Chicane parameters from path length difference . . . 20
4.2 Maximum dispersion in the chicane . . . 23
4.3 Coherent Synchrotron Radiation . . . 24

5 Energy spread and beam emittance 26
5.1 Method of energy spread measurement . . . 26
5.2 Method of transverse emittance measurement . . . 27
5.2.1 Error propagation . . . 29

6 Theory and simulations for THz radiation with micro-bunched beams 30
6.1 Theory of an energy-chirped beam . . . 31
6.2 Theory of a micro-bunched beam . . . 33
6.2.1 Frequency dependence on energy chirp . . . 35
6.2.2 Observing micro-bunching in the transverse plane . . . 36
6.3 Beam optics for the micro-bunched beam production . . . 38
6.4 Simulations of micro-bunched beam production with ELEGANT . . . 40
6.5 Simulations of micro-bunched beam observation with ELEGANT . . . 44
6.6 Simulations of micro-bunched beam production with flat beams . . . 46
6.6.1 Canonical angular momentum beam . . . 46
6.6.2 Flat beam . . . 47
6.6.3 Removing an angular momentum . . . 48
6.6.4 Generating flat beams . . . 49
6.7 Generation of THz radiation . . . 52
6.7.1 Transition radiation . . . 52
6.7.2 Energy density enhanced with a small wiggler . . . 54
6.8 Detection of THz radiation . . . 56
6.8.1 Michelson and Martin Puplett interferometers . . . 56
6.8.2 Bolometer and Pyroelectric detector . . . 59

7 THz radiation experiments 60
7.1 RF phases at the minimum energy spread . . . 60
7.2 Micro-bunched beam production and measurements . . . 61
7.3 Micro-bunched beam measurements with pyrometers . . . 65
7.4 Bremsstrahlung from the slit-mask and beam pipe . . . 68
7.5 Radiation shielding for upcoming THz radiation experiments . . . 70
7.6 Experimental setup for upcoming THz radiation experiments . . . 74
7.7 Summary of THz radiation experiments . . . 76

8 Optics design and simulations for Channeling Radiation 77
8.1 Beam optics solutions for CR . . . 81
8.1.1 Beam optics solutions for high brightness CR . . . 81
8.1.2 Beam optics solutions for high yield CR . . . 86
8.2 Beam optics solutions with misalignment and magnetic field error . . . 88
8.3 Background from bremsstrahlung . . . 91
8.4 Electron beam distributions after crystal . . . 96
8.5 Compton scattering for X-ray detector . . . 99

9 Channeling Radiation Experiments 103

9.1 Setup for CR experiments 103
9.2 CR experiments 105
9.3 Summary of CR experiments 109

10 Conclusions **110**

Bibliography **112**

List of Figures

3.1 Layout of the FAST's facility. . . . 14
3.2 Layout of the FAST photoinjector. . . . 18

4.1 Layout of a magnet chicane. . . . 20

6.1 Phase space along the beamline. . . . 30
6.2 Fundamental frequency depending on energy chirps. . . . 36
6.3 Spacing ($8\sigma_z$) and width (Δz) of micro-bunched beams as a function of $\sqrt{\beta_x \epsilon_x}$ at the slit-mask for different energy chirps. . . . 39
6.4 Beta and dispersion functions at $h = -7$ m^{-1} for CC1 chirp. . . . 39
6.5 Longitudinal phase space and bunching factor at X121 at the maximum compression (h~5.6 m^{-1}). . . . 41
6.6 Longitudinal phase spaces for each energy chirp at X121. . . . 41
6.7 Longitudinal distributions at CC1 chip ($h = \pm 7\,\mathrm{m}^{-1}$), CC2 chirp ($h = \pm 9\,\mathrm{m}^{-1}$), and CC1&CC2 chips ($h = \pm 16\,\mathrm{m}^{-1}$). . . . 42
6.8 Frequency spectra for CC1 chip ($h = \pm 7\,\mathrm{m}^{-1}$), CC2 chirp ($h = \pm 9\,\mathrm{m}^{-1}$), CC1&CC2 chips ($h = \pm 16\,\mathrm{m}^{-1}$), and the longitudinal maximum compression ($h \sim 5.6\,\mathrm{m}^{-1}$). . . . 43
6.9 Fundamental frequency as a function of energy chirp. . . . 44
6.10 The transverse distributions at h=-7 m^{-1} at $X120$ and $X121$ when the K_S-value of the skew quadrupole is set equal to -5 m^{-2}. . . . 45
6.11 Vertical spacing as a function of K_S-values of the skew quadrupole. . . . 45
6.12 Beam distributions for each energy chip before the chicane. . . . 51
6.13 Bunching factors for each energy chirp after the chicane. . . . 51
6.14 Sketch of the transition radiation. . . . 52
6.15 Energy density spectrum from two radiation sources with two chirp settings using CC1 and CC2. . . . 55
6.16 Sketch of a Michelson interferometer. . . . 58
6.17 Schematic of a Martin-Puplett interferometer. . . . 58
6.18 Simplified bolometer (left) and pyroelectric detector (right). . . . 59

7.1 Vertical beam sizes at X124 depending on RF phases. . . . 62
7.2 Vertical beam distributions at the minimum energy spread at X124. . . . 63
7.3 Beam distributions at the slit-mask (X115) after horizontal beam focus. . . . 63
7.4 Vertical beam sizes at X120 before (top) and after (bottom) additional focusing. . . . 64
7.5 Beam distributions at X120 at each RF phase of CC1 when the slit-mask is inserted and the skew quadrupole magnet is set to 0.9 A. . . . 65

7.6 Vertical spacing depending on the current of the skew quadrupole magnet at (CC1, CC2)=(0°, +30°) and (+30°, 0°). 65
7.7 Beamline geometry and pyrometers. 66
7.8 The autocorrelation function (top) and the frequency spectrum (bottom) for the maximum longitudinal compression of the beam. 67
7.9 The autocorrelation functions with pyrometers and the frequency spectra when the electron beam bunch is lengthened. 67
7.10 Electron beam (left) and energy (right) distributions after the slit-mask. . 68
7.11 Transverse distributions of Electrons, photons, neutrons, and positron distributions at z=4 m (around the pyrometers). 69
7.12 Energy distributions of Electrons, photons, neutrons, and positron distributions at z=4 m (around the pyrometers). 69
7.13 THz detector system with the Michelson interferometer and a bolometer. 70
7.14 Simulation geometries for different radiation shielding places. 71
7.15 Electron distributions for each case at the bolometer. 72
7.16 Photon distributions for each case at the bolometer. 72
7.17 Positron distributions for each case at the bolometer. 73
7.18 Neutron distributions for each case at the bolometer. 73
7.19 The Michelson interferometer installed upstream of the Martin-Puplett interferometer. 75
7.20 A He-cooled bolometer (HDL-5 model, IRLabs). 75

8.1 Initial population depending on beam divergences for different states of n=0, 1, 2, and 3 at incident angle of 0 degree. 80
8.2 Photon yields for beam divergences of 0.1, 0.3, 0.9, and 1.1 mrad. 80
8.3 Optics functions of the transport line when beam sizes at crystal are minimum for 1 pC, 20 pC, and 200 pC. 83
8.4 Beam sizes at the crystal depending on the beta functions for 1 pC, 20 pC, and 200 pC. 84
8.5 Beam size distributions at the crystal for different momentum spreads for 20 pC when the beta functions at the crystal are 3 mm. 85
8.6 Beam optics for the high yield solution along the transport line from the last cavity to the beam dump. 87
8.7 Orbit corrections with steering magnets for the high brightness optics (upper plots (a) and (b)) and the high yield optics (bottom plots (c) and (d)) for 200 pC. 89
8.8 Transverse central orbit along the beamline for the high brightness optics (upper plots (a) and (b)) and the high yield optics (bottom plots (c) and (d)) after the orbit correction for 200 pC. 90
8.9 Layout showing goniometer and the detector. 91
8.10 Angular distributions of photons emitted in the forward direction and in the detector with an acceptance of 2 mrad. 93
8.11 Bremsstrahlung spectra in the forward direction (blue) and in the detector (red). 93
8.12 Number of photons hitting the detector depending on beam divergences and beam sizes of incident electrons. 93
8.13 Bremsstrahlung spectra for different electron energies of 43 MeV, 60 MeV, 80 MeV, and 100 MeV. 95

8.14 The expected X-ray spectrum including the background for difference estimates of the CR photon number. 95
8.15 Angular distributions of a 43 MeV electron beam before and after going through the diamond crystal with the thickness of 168 μm. 98
8.16 Beam positions and sizes (x, y) after the non-channeled (left) and the channeled (right) electron beam in the diamond crystal. 98
8.17 Energy distributions of the electron beam before and after the diamond crystal. 98
8.18 Differential cross-section (upper) and photon energy (lower) depending on scattering angle. 100
8.19 Layout of the detector. 101
8.20 Three major types of photon interaction with matter. 101
8.21 The number of Compton scattered photons and the energy in the detector for different crystals. 102

9.1 The goniometer with the Al foil and the diamond crystal, and the clear aperture installed in the beamline. 104
9.2 Layout of the CR experimental setup. 104
9.3 Dark current as a function of the beam energy after the RF gun. 105
9.4 Beam optics before (upper) and after (bottom) the beam focus at the diamond crystal. 106
9.5 The two detector counts depending on a bunch charge current. 107
9.6 Radiation spectra measured with the forward (green dots) and the Compton (blue dots) detectors. 108
9.7 Radiation spectrum going into the Compton detector (red line) and bremsstrahlung spectra from the stainless steel with a thickness of 1.7 mm simulated with GEANT4. 108
9.8 Bremsstrahlung (red lines) from the beam duct in the chicane and characteristic X-rays (blue lines) from lead going into the X-ray detectors. . . 108

List of Tables

3.1 Injector parameters . . . 17
3.2 Magnet parameters for a 50 MeV electron beam. . . . 17

6.1 The final energy chirps for different RF phase in CC1 and CC2. . . . 33
6.2 Micro-bunch widths, spacing, and fundamental frequencies calculated analytically with Eq. (6.21), (6.23), and (6.24), respectively. . . . 36
6.3 Micro-bunch widths, spacing, and fundamental frequencies for each energy chirp. . . . 44
6.4 Normalized beam emittances and emittance ratios for h=-7, -10, -17 simulated with ASTRA and ELEGANT. . . . 50
6.5 K-values of skew quadrupole magnets (Q106, Q107, Q111) for h=-7, -10, -17 simulated with ELEGANT and calculated with Eq. (6.47-6.49). Values in parentheses show the K-values estimated with the analytical equations. 50

7.1 Energy chirps corresponding to CC1 RF phases. . . . 64

8.1 X-ray energies generated for a diamond crystal and 43 MeV electrons. . . . 79
8.2 Twiss parameters, normalized emittances, and energy spreads for 1, 20, and 200 pC at 8 m from the photocathode, from ASTRA simulations. . . . 81
8.3 Minimum beam sizes, beam divergences, and beta functions at the crystal for the different charges. . . . 85
8.4 Average brilliances at each bunch charge for high brightness solutions. . . . 85
8.5 Photon fluxes at each bunch charge for high brightness solutions. . . . 85
8.6 Beam sizes and beta functions for a beam divergence of 0.1 mrad at the crystal. . . . 86
8.7 Photon fluxes at each bunch charge for a beam divergence of 0.1 mrad at the crystal. . . . 86
8.8 Alignment and field errors for the quadrupole magnets. . . . 88
8.9 Beam sizes and beta functions at the crystal achieved for the high brightness optics using the quadrupole magnets with the misalignments and field errors. . . . 89
8.10 The number of background photons registered in the detector for three charges. . . . 92
8.11 Number of photons generated in the forward direction for different electron energies of 43 MeV, 60 MeV, 80MeV, and 100 MeV. . . . 95
8.12 The number of background photons per second registered in the detector for three charges. . . . 100

Abbreviations

FAST	**F**ermilab **A**ccelerator **S**cience and **T**echnology
IOTA	**I**ntegrable **O**ptics **T**est **A**ccelerator
CsTe	**Ce**sium **Te**lluride
CR	**C**hanneling **R**adiation
YAG	**Y**ttrium **A**luminum **G**arnet
CTR	**C**oherent **T**ransition **R**adiation
TR	**T**ransition **R**adiation
LSC	**L**ongitudinal **S**pace **C**harge
CAM	**C**anonical **A**ngular **M**omentum
MPI	**M**artin-**P**uplett **I**nterferometer
MI	**M**ichelson **I**nterferometer
BS	**B**rem**S**strahlung
CdTe	**Cd**mium **Te**lluride
PVC	**P**oly**V**inyl **C**hloride
PMMA	**P**oly**M**ethyl **M**eth**A**crylate

Chapter 1

Introduction

Particle accelerators have been utilized in not only high energy physics for an understanding of the universe but also in the medical field for cancer therapy and in material science for materials analysis, and are one of the essential tools in a wide range of scientific and industrial fields. Synchrotron radiation from an accelerator, which can generate light with a range of wavelengths, is especially a powerful radiation source since users can choose a high intensity specific wavelength depending on their experimental purposes. Recently, using FELs, we can obtain the high intensity coherent light with a wide energy range except for THz and hard X-ray ranges. Also, micron wavelength radiation or radio waves have been studied for a long time and already utilized as radars, communication tools, and microwave ovens which are our familiar items.

The development and application of THz and hard X-ray regions are left behind compared with other wavelength ranges. A while ago, it was difficult to generate THz radiation whose frequency range is from 0.1 THz (λ=0.3 mm) to 30 THz (λ=10 μm) due to technical difficulties. Recently, THz sources with lasers and/or accelerators have been proposed and developed [1–16], however, they cannot be said to be a compact high intensity radiation source with frequency tunability. As for hard X-rays with an energy of over 100 keV, broadband hard X-rays can be generated by bending 8 GeV class electron beams, while the generation of quasi-monochromatic hard X-rays requires an insertion device and monochromators. Therefore, experiments such as high energy fluorescent X-ray spectroscopy need to be performed in a limited number of high energy synchrotron radiation facilities such as national laboratories.

The final goal is to develop a compact, energy tunable, and high intensity THz and hard X-ray sources for applications in many fields. The objectives of this thesis are 1) to propose the feasible THz/hard X-ray sources which can generate narrow-band THz waves with a frequency of over 1 THz and quasi-monochromatic hard X-rays in an

energy range from 50 keV to 110 keV, and 2) to demonstrate that the proposed methods can be a compact and frequency tunable high intensity THz/hard X-ray sources. The demonstration experiments on THz and hard X-ray generation were performed at the FAST (Fermi Accelerator Science and Technology) facility [17, 18] in Fermilab.

The method to generate narrow-band THz radiation in a small accelerator facility is the use of a slit-mask and a chicane. We create a micro-bunched beam by combining them to emit narrow-band THz radiation. On the other hand, we employ channeling radiation (CR) which can emit quasi-monochromatic hard X-rays with a single crystal and an electron beam with an energy of below 100 MeV [19–22]. These are simple methods, which does not require an insertion device. We use electron beams with an energy of at most 50 MeV, as the footprint of an accelerator facility depends on the electron beam energy due to the number of accelerating structures and thickness of radiation shielding around the accelerator.

In following Section 1.1 and 1.2, the details of our ideas for each radiation source are described. In Chapter 2, the beam dynamics including transfer and beam matrices of each magnet installed in the beamline, Twiss parameters, and beam emittance are described. In Chapter 3 and 4, the FAST injector, the beam, and machine parameters are shown. We introduce measurements of energy spread and a beam emittance in Chapter 5. The theory, the particle tracking simulations, and the experimental results for THz radiation with micro-bunched beams are presented in Chapter 6 and 7. In Chapter 8 and 9, we present the simulation and experimental results of CR. In Chapter 10, conclusions are described.

1.1 THz radiation

THz radiation has features of non-ionizing and high transmission through non-metal materials such as clothes, paper, plastic. Moreover, many materials have characteristic absorption spectra in the THz range. Therefore, THz radiation has been utilized in fundamental research in material, biological, and engineering science. In a THz source based on a combination of a laser and a crystal, the crystal damage for the high power laser becomes the problem. Also, THz radiation emitted by CSR and Transition radiation with an accelerator is spectrally broadband [14, 23, 24]. We would like to develop a tunable narrow-band THz radiation source for applications such as molecular spectroscopy, imaging, resonant control. One of the methods to emit narrow-band THz radiation with an accelerator is the use of an undulator which is an insertion device [10, 25], however, it requires high construction cost.

In order to generate narrow-band THz radiation in a compact accelerator facility, we focused on a simple method of producing a micro-bunched beam using a slit-mask and a chicane which is one of the standard components in an accelerator [26–28]. The transverse slicing of a bunch by the slit-mask installed in the chicane is transformed into the longitudinal plane taking advantage of dispersion at the slit-mask. Also, a magnetic chicane consisting of four dipole magnets can lengthen or shorten to an appropriate comb structure required to generate THz radiation. The advantage with this method is that narrow-band THz radiation with frequency tunability can be emitted by choosing RF phases in the cavities. Moreover, intense THz radiation can be generated due to a high bunch repetition rate.

We also considered an observation method of micro-bunched beams. In general, micro-bunch beams are monitored using a streak camera and an RF deflector. As we create the micro-bunched beam with a spacing of ∼0.3 mm, a streak camera cannot measure it correctly due to the resolution. Also, an RF deflector requires high production cost and beamline space. Therefore, we monitor the micro-bunched beam with a skew quadrupole magnet placed downstream of the slit-mask in the chicane. We can see modulations in the vertical plane after the chicane when the skew quadrupole magnet is turned on, since the skew quad creates a vertical dispersion, and the vertical plane of the electron beam after the chicane has information on horizontal separation at the skew quad.

For generating higher intensity THz radiation with higher narrow-band frequencies, we considered the use of a flat beam and a wiggler. The theory of a micro-bunched beam says that $\beta_x\varepsilon_x$ at the slit-mask should be as small as possible for clear longitudinal separations of a micro-bunched beam (ideally δ-function). This leads to an increase in the bunching factor at higher harmonics (frequency). As a result, the intensity at higher frequencies will be also increased. We simulated the production of a flat beam and obtained an emittance ratio of $\varepsilon_y/\varepsilon_x = 200$ at FAST. Through simulations with the flat beam, we found that narrow-band radiation with high bunching factors at high frequencies is emitted. Moreover, to amplifier the intensity, we calculated the energy density [J/THz] when the micro-bunched beam passes through a small wiggler. As a result, the energy density from the wiggler can be increased about 500 times higher than that from CTR. In this thesis, the details of the theory, simulations, and experiment results are present, and also the setup of a bolometer used in the upcoming experiments are described.

1.2 Channeling radiation

Channeling radiation (CR) can be generated when high energy charged particles such as electrons and positrons pass through a single crystal parallel to a crystal plane or axis [29]. The electron motion in the crystal is similar to that in an undulator, therefore, generated X-rays are quasi-monochromatic and high energy for an electron beam with an energy of below 100 MeV. For instance, CR can emit X-rays with an energy of 100 keV using a ∼50 MeV energy electron beam [30, 31]. By comparison, synchrotron radiation (SR), is currently the main X-ray source, requires a few GeV electron beam to generate X-rays of 100 keV. For an inverse Compton scattering, an electron beam energy of ∼75 MeV is needed for a laser wavelength of 1 μm. Therefore, CR has the potential to be used for a compact quasi-monochromatic hard X-ray source. In the 1980s and the 1990s, CR generation experiments with a ∼50 MeV electron beam and a diamond and a silicon crystals were carried out [30–33]. However, the high photon flux could not be radiated due to a high emittance beam. Recently, a photocathode RF gun can produce a lower emittance beam than that emitted by a thermal electron gun ∼30 years ago, and we can also obtain a high quality single crystal.

We used a diamond crystal because of its low atomic number Z, high Debye temperature, and large thermal conductivity. The crystal is oriented so that the electron beam propagates parallel to the (110) plane of the crystal. The electron beam energy of 43 MeV is chosen to generate hard X-rays, and then expected X-ray energies are 51 keV, 67.5 keV, and 110 keV with each energy spread of about 10%. We detect them using the CdTe X-123 (Amptek) pin diode detector that can measure X-rays with an energy range of 5 keV-150 keV. We set the target yield as 10^9 photons/s that is the minimum required to be applicable as a hard X-ray source in scientific fields.

Recently, the theoretical model of CR was improved with the model of de-channeling and re-channeling characterized by a free parameter n_f [34]. The n_f was determined using data measured at CR experiments in the ELBE facility. As a result, within 20% error bars, the theoretical CR yields are in agreement with those measured at 14, 17, and 30 MeV in the ELBE facility. The CR yields expected at the FAST facility have been already calculated and reported in [34, 35]. We need to verify the updated model and improve the CR theory using data measured at ∼50 MeV in the FAST facility to resolve the remaining discrepancy between experiments and theory.

We performed more detailed calculations of the CR yields including bremsstrahlung background from the diamond crystal with GEANT4, simulations of beam optics for high yield and high brightness operations, and consideration of the Compton spectrometer as the second detector to avoid pile-up effects during high charge operations [22, 36]. In

this thesis, the detailed simulation results and the results of CR experiments performed in the FAST facility, and the analysis are presented.

Chapter 2

Beam dynamics

In an accelerator, charged particles are transported using various types of magnets for beam steering and focusing. The evolution of beam trajectories under the Lorentz force along a beamline is called the beam optics (or beam dynamics). In this section, we introduce linear beam dynamics which describes the motion of ensembles of particles in an accelerator. The basic beam parameters such as a beam emittance, Twiss parameters, and transfer matrices (mathematical formulas) of several magnets used in an accelerator are also explained.

2.1 Equation of Motion of a charged particle

A charged beam in electromagnetic fields experiences a force known as the Lorentz force, and the beam trajectory is deflected. When a particle with a charge q moving a velocity $\boldsymbol{v}$ passes through a magnet with an electromagnetic field $\boldsymbol{E}$ and a magnetic field $\boldsymbol{B}$, the Lorentz force acting on the particle is [37–39]

$$\boldsymbol{F} = \frac{d\boldsymbol{P}}{dt} = q(\boldsymbol{E} + \boldsymbol{v} \times \boldsymbol{B}), \tag{2.1}$$

where $\boldsymbol{P}$ is the momentum of the particle, and Newton's law of motion ($\boldsymbol{F}$=$\dot{\boldsymbol{P}}$) is used. According to the theory of special relativity, the relation between the particle momentum $\boldsymbol{P}$ and the particle velocity $\boldsymbol{v}$ is

$$\boldsymbol{P} = \frac{m\boldsymbol{v}}{\sqrt{1 - \frac{v^2}{c^2}}} = \frac{m\boldsymbol{v}}{\sqrt{1 - \beta^2}} = \gamma m\boldsymbol{v}. \tag{2.2}$$

Trajectories and beam sizes of charged beams with a relativistic velocity are controlled with magnetic fields $\boldsymbol{B}$ such as a dipole and a quadrupole magnet. When a charged

beam is bend using a dipole magnet, a relation between the beam energy and the dipole magnet can be written as $P = qB\rho$, where q is the charge of a particle and ρ is the bending radius. For an electron beam, we have

$$P[\mathrm{GeV/c}] \simeq 0.2998\mathrm{B[T]}\rho[\mathrm{m}]. \tag{2.3}$$

In general, a beam energy is measured by bending an electron beam with a dipole magnet.

In accelerator physics, the motion of a particle is described with a six-dimensional phase space with coordinates [40, 41]

$$\boldsymbol{X}(s) = \left[x(s),\ x'(s),\ y(s),\ y'(s),\ z(s),\ \delta\right]^T, \tag{2.4}$$

s: a position along a reference trajectory $\boldsymbol{X}(0)$,
x, y: the horizontal and vertical displacements from the reference trajectory,
$x' = dx/ds$, $y' = dy/ds$: the horizontal and vertical angles from the reference trajectory,
z: the longitudinal displacement from $s = 0$,
$\delta = dP/P_0$: a relative momentum deviation from the reference momentum P_0.

When a charged particle at position s_0 is transported to another position s_f after passing through elements of magnets and drift space, the phase space of the charged beam $\boldsymbol{X}(s_f)$ can be written as [42]

$$\boldsymbol{X}(s_f) = M_n \cdot M_{n-1} \cdot \ldots \cdot M_1 \cdot \boldsymbol{X}(s_0), \tag{2.5}$$

where M_i $(i = 1, ..., n)$ are the 6×6 transfer matrices of magnets and drift spaces consisting of the beamline, and the determinant of all transfer matrices in linear beam optics is always $\det M_i$=1.

2.2 Transfer matrices

The six dimensional phase space of a charged particle transformed from the initial positron i to the final position f in a beamline can be shown with multiplications of transfer matrices M of elements of an accelerator, as mentioned in Eq. (2.5). Here, the linear transfer matrices of drift space, quadrupole magnet, dipole magnet are described.

Assuming that we use the transverse magnetic field of dipole magnets $\boldsymbol{B}(x, y, z) = (0, B_y, 0)$ and quadrupole magnets $\boldsymbol{B}(x, y, z) = (B_x, B_y, 0)$ in cartesian coordinates,

transverse motions of a particle can be written as [39, 41]

$$\frac{d^2x}{ds^2} + K_x(s)x(s) = \frac{1}{\rho}\frac{\Delta P}{P}, \quad \frac{d^2y}{ds^2} + K_y(s)y(s) = 0, \tag{2.6}$$

$$K_x(s) = -\frac{B'}{B\rho} + \frac{1}{\rho^2}, \quad K_y(s) = \frac{B'}{B\rho}, \tag{2.7}$$

where $B'=\partial B_x/\partial y=\partial B_y/\partial x$ represents the gradient of a quadrupole magnet. The transfer matrices of each element of an accelerator can be obtained by solving Eq. (2.6). Also, the magnetic fields B_x and B_y of each magnet are obtained by solving Maxwell equations.

2.2.1 Drift space

An electron beam in a drift space travels in the beamline without acting on a magnetic field: $\boldsymbol{B}(x, y, z) = (0, 0, 0)$ and $1/\rho = 0$. From Eq. (2.6) and (2.7), $\frac{d^2x(s)}{ds^2}$=0 and $\frac{d^2y(s)}{ds^2}$=0. As a result, we obtain $x(L)$=$x(0)$+$Lx'(0)$ and $y(L)$=$y(0)$+$Ly'(0)$, where L is the distance of the drift space. Therefore, a transfer matrix M_{drift} of a drift space is

$$M_{drift} = \begin{pmatrix} 1 & L & 0 & 0 & 0 & 0 \\ 0 & 1 & 0 & 0 & 0 & 0 \\ 0 & 0 & 1 & L & 0 & 0 \\ 0 & 0 & 0 & 1 & 0 & 0 \\ 0 & 0 & 0 & 0 & 1 & \frac{L}{\gamma^2} \\ 0 & 0 & 0 & 0 & 0 & 1 \end{pmatrix}, \tag{2.8}$$

where $L/\gamma^2(=M_{56})$ is close to zero for high energy electron beams.

2.2.2 Quadrupole magnet

Quadrupole magnets are used to control (focusing and de-focusing) electron beam sizes, and the transverse motions of an electron beam in a quadrupole magnet (ρ=0) from Eq. (2.6) and (2.7) are $\frac{d^2x}{ds^2} - \frac{B'}{B\rho}x$=0 and $\frac{d^2y}{ds^2} + \frac{B'}{B\rho}y$=0. A transfer matrix M_{quad} of a quadrupole magnet with a magnetic length L can be driven by solving these equations

for the horizontal and vertical planes.

$$M_{quad} = \begin{pmatrix} \cos(\sqrt{K}L) & \frac{\sin(\sqrt{K}L)}{\sqrt{K}} & 0 & 0 & 0 & 0 \\ -K\sin(\sqrt{K}L) & \cos(\sqrt{K}L) & 0 & 0 & 0 & 0 \\ 0 & 0 & \cosh(\sqrt{|K|}L) & \frac{\sinh(\sqrt{|K|}L)}{\sqrt{|K|}} & 0 & 0 \\ 0 & 0 & \sqrt{|K|}\sinh\sqrt{|K|}L & \cosh(\sqrt{|K|}L) & 0 & 0 \\ 0 & 0 & 0 & 0 & 1 & \frac{L}{\gamma^2} \\ 0 & 0 & 0 & 0 & 0 & 1 \end{pmatrix}. \quad (2.9)$$

The magnetic fields in quadrupole magnets act to focus the electron beam in one plane (x or y) and defocus in the other plane.

2.2.3 Dipole magnet

Dipole magnets with a bending radius ρ and a bending angle θ, used to bend electron beams, are divided into two types: rectangular and sector magnets. The rectangular magnet has edge focus, which is the same function as a quadrupole magnet at the entrance and exit of the magnets, while the sector magnet does not have the edge focus at the end faces.

2.2.3.1 Sector magnet

When a beam goes through a sector magnet, the central trajectory of the beam enters and exits perpendicular to the entrance and the exit of the magnet. From Eq. (2.6), (2.7), and the z-component in Eq. (2.1), the transverse and longitudinal motions are given by $\frac{d^2x}{ds^2} \sim -\frac{x}{\rho^2} + \frac{1}{\rho}\frac{\Delta P}{P}$, $\frac{d^2y}{ds^2}=0$, and $\frac{d^2z}{ds^2}=-\frac{1}{\rho}\frac{dx}{ds}$. The general solution in the horizontal plane is the summation of the homogeneous and inhomogeneous equations. As a result, a transfer matrix M_{sec} of a sector magnet is given by

$$M_{sec} = \begin{pmatrix} \cos\theta & \rho\sin\theta & 0 & 0 & 0 & \rho(1-\cos\theta) \\ -\frac{\sin\theta}{\rho} & \cos\theta & 0 & 0 & 0 & \sin\theta \\ 0 & 0 & 1 & L & 0 & 0 \\ 0 & 0 & 0 & 1 & 0 & 0 \\ -\sin\theta & -\rho(1-\cos\theta) & 0 & 0 & 1 & -\rho(\theta-\sin\theta) \\ 0 & 0 & 0 & 0 & 0 & 1 \end{pmatrix}. \quad (2.10)$$

Comparing this matrix with Eq. (2.9), electron beams passing through a sector magnet are focused in the horizontal plane, while the motion of the beam in the vertical plane is the same as a drift space.

2.2.3.2 Rectangular magnet

A rectangular magnet is a dipole magnet with an edge angle of Φ at the entrance and the exit of a sector magnet. The central trajectory of a beam goes into the entrance and the exit of the rectangular magnet at an edge angle $\Phi = \theta/2$, and then edge focusing like a quadrupole magnet acts on the beam at the end faces. The deflecting angle by the edge is given by $\frac{x\tan\Phi}{\rho}$, and the transfer matrix M_{edge} of the edge focusing can be written as

$$M_{edge} = \begin{pmatrix} 1 & 0 & 0 & 0 & 0 & 0 \\ \frac{1}{\rho}\tan(\frac{\theta}{2}) & 1 & 0 & 0 & 0 & 0 \\ 0 & 0 & 1 & 0 & 0 & 0 \\ 0 & 0 & -\frac{1}{\rho}\tan(\frac{\theta}{2}) & 1 & 0 & 0 \\ 0 & 0 & 0 & 0 & 1 & 0 \\ 0 & 0 & 0 & 0 & 0 & 1 \end{pmatrix}. \tag{2.11}$$

A transfer matrix M_{rectan} of a rectangular magnet, can be given by M_{rectan}=M_{edge} · M_{sector} · M_{edge}, results in

$$M_{\text{rectan}} = \begin{pmatrix} 1 & \rho\sin\theta & 0 & 0 & 0 & \rho(1-\cos\theta) \\ 0 & 1 & 0 & 0 & 0 & 2\tan(\frac{\theta}{2}) \\ 0 & 0 & 1-\theta\tan(\frac{\theta}{2}) & \rho\theta & 0 & 0 \\ 0 & 0 & -\frac{1}{\rho}\tan(\frac{\theta}{2})(2-\theta\tan(\frac{\theta}{2})) & 1-\theta\tan(\frac{\theta}{2}) & 0 & 0 \\ -2\tan(\frac{\theta}{2}) & -\rho(1-\cos\theta) & 0 & 0 & 1 & -\rho(\theta-\sin\theta) \\ 0 & 0 & 0 & 0 & 0 & 1 \end{pmatrix}. \tag{2.12}$$

2.3 Beam matrices

The 6×6 matrix $\boldsymbol{X_2}$ after an electron beam passes through an element of an accelerator with a transfer matrix M is given by $\boldsymbol{X_2}$=$M\boldsymbol{X_1}$, where $\boldsymbol{X_1}$ represents the initial phase space of an electron beam, and then the transposed matrix becomes $\boldsymbol{X_2^T}$=$\boldsymbol{X_1^T}M^T$. By averaging and multiplying these equations, we have $\langle \boldsymbol{X_2}\boldsymbol{X_2^T}\rangle = M\langle \boldsymbol{X_1}\boldsymbol{X_1^T}\rangle M^T$. Here,

we define a beam matrix $\sigma(s)$

$$\sigma(s) = \langle \boldsymbol{X}\boldsymbol{X}^{\boldsymbol{T}} \rangle = \begin{pmatrix} \langle x^2 \rangle & \langle xx' \rangle & \langle xy \rangle & \langle xy' \rangle & \langle xz \rangle & \langle x\delta \rangle \\ \langle xx' \rangle & \langle x'^2 \rangle & \langle x'y \rangle & \langle x'y' \rangle & \langle x'z \rangle & \langle x'\delta \rangle \\ \langle xy \rangle & \langle x'y \rangle & \langle y^2 \rangle & \langle yy' \rangle & \langle yz \rangle & \langle y\delta \rangle \\ \langle xy' \rangle & \langle x'y' \rangle & \langle yy' \rangle & \langle y'^2 \rangle & \langle y'z \rangle & \langle y'\delta \rangle \\ \langle xz \rangle & \langle x'z \rangle & \langle yz \rangle & \langle y'z \rangle & \langle z^2 \rangle & \langle z\delta \rangle \\ \langle x\delta \rangle & \langle x'\delta \rangle & \langle y\delta \rangle & \langle y'\delta \rangle & \langle z\delta \rangle & \langle \delta^2 \rangle \end{pmatrix}. \tag{2.13}$$

The beam sizes $\sigma_{x,y}$ are defined by the square root of the $\langle x^2 \rangle$ and $\langle y^2 \rangle$. When a beam travels an element with a transfer matrix M from the initial position s_1, the sigma matrix $\sigma(s_2)$ can be calculated as $\sigma(s_2) = M\sigma(s_1)M^T$.

2.4 Phase space ellipse

An electron beam in a beamline consists of many particles and travels oscillating transversally around the central trajectory. In this section, we describe the properties of transverse motions of the electron beam.

2.4.1 Twiss parameters α, β, and γ

As mentioned before, the basic horizontal motion of an electron beam for $\Delta P/P$=0 is $x''(s) + K_s(s)x(s)$=0 from Eq. (2.6), where $x(s)$ is betatron oscillation which represents a transverse oscillation around the central trajectory of the beam. The general solution of this equation can be written as $x(s)$=$a\sqrt{\beta_x(s)}\cos(\psi_x(s) - \psi_{x_0})$, where $\psi_x(s)$=$\int_0^s \frac{ds}{\beta_x(s)}$ is the phase function, β_x is the beta function known as the amplitude function, and a and ψ_{x0} are constants of integration [41, 43]. Then, $x'(s)$ is

$$x'(s) = -a\sqrt{\gamma(s)}\sin(\psi_x(s) - \psi'_{x_0}), \tag{2.14}$$

$$\Rightarrow \gamma = \frac{1+\alpha^2(s)}{\beta(s)}, \quad \alpha = -\frac{1}{2}\frac{d\beta(s)}{ds}. \tag{2.15}$$

2.4.2 Beam emittance

When the horizontal and the vertical motions do not have correction each other, the general solutions of the beam trajectory are

$$x(s) = a\sqrt{\beta_x(s)}\cos(\psi_x(s) - \psi_{x_0}), \tag{2.16}$$

$$x'(s) = -\frac{\alpha}{\beta}x - \frac{a}{\sqrt{\beta}}\sin(\psi_x(s) - \psi_{x_0}). \tag{2.17}$$

From these equations, we have $\beta x'(s) + \alpha x(s) = -a\sqrt{\beta}\sin(\psi_x(s) - \psi_{x_0})$. Therefore, we can obtain the following relation

$$\frac{x^2 + (\beta x' + \alpha x)^2}{\beta} = a^2 \quad (= \text{constant}). \tag{2.18}$$

This shows the equation of an ellipse, and the area of this ellipse S is $S = \pi a^2$. This a^2 is called an emittance, and it is written with ε. From Eq. (2.18), we have

$$\gamma(s)x^2 + 2\alpha(s)x'x + \beta(s)x'^2 = \varepsilon. \tag{2.19}$$

This is called the Courant-Snyder invariant and is described with Twiss parameters: $\alpha(s)$, $\beta(s)$, and $\gamma(s)$. This shape of the ellipse varies along a beamline, but the area stays constant. Also, we consider the maximum values in Eq. (2.16) and (2.17) and take average values of them,

$$\langle x^2 \rangle = \varepsilon\beta, \quad \langle x'^2 \rangle = \varepsilon\gamma, \quad \langle xx' \rangle = -\varepsilon\alpha. \tag{2.20}$$

2.4.2.1 Two dimensional beam emittance

From Eq. (2.13), a 2×2 beam matrix $\sigma(s)_{2\times2}$ can be expressed as

$$\sigma(s)_{2\times2} = \begin{pmatrix} \langle x^2 \rangle & \langle xx' \rangle \\ \langle xx' \rangle & \langle x'^2 \rangle \end{pmatrix} = \varepsilon \begin{pmatrix} \beta(s) & -\alpha(s) \\ -\alpha(s) & \gamma(s) \end{pmatrix}. \tag{2.21}$$

We take a determinant of this equation,

$$\det\sigma(s)_{2\times2} = \langle x^2 \rangle\langle x'^2 \rangle - \langle xx' \rangle^2 = \varepsilon^2(\beta\gamma - \alpha^2) = \varepsilon^2, \tag{2.22}$$

$$\Rightarrow \varepsilon^{2D} = \sqrt{\det\sigma_{2\times2}}. \tag{2.23}$$

ε^{2D} ($=\varepsilon_x$, ε_y) is called a two dimensional emittance or a projected emittance, which is obtained by treating the transverse motions (x, y) of the beam, separately even if the beam is coupled in the horizontal and vertical planes. The x-y coupling causes an

increase in the 2D emittance $\varepsilon_{x,y}$ since the beam with the x-y coupling is projected onto the horizontal and vertical planes. This 2D emittance $\varepsilon_{x,y}$ can be obtained measuring beam sizes varying the strength of a quadrupole magnet ("Q-scan method") or using wire scanner [44].

2.4.2.2 Four dimensional beam emittance

From Eq. (2.13), a 4×4 sigma matrix σ_{4D} is given by

$$\sigma_{4\sigma} = \begin{pmatrix} \langle x^2 \rangle & \langle xx' \rangle & \langle xy \rangle & \langle xy' \rangle \\ \langle xx' \rangle & \langle x'^2 \rangle & \langle x'y \rangle & \langle x'y' \rangle \\ \langle xy \rangle & \langle x'y \rangle & \langle y^2 \rangle & \langle yy' \rangle \\ \langle xy' \rangle & \langle x'y' \rangle & \langle yy' \rangle & \langle y'^2 \rangle \end{pmatrix}. \tag{2.24}$$

This matrix shows that an electron beam has a correlation (x-y coupling) between the horizontal and the vertical planes which is caused by misalignment of magnets and a solenoid coil [37]. The $\sigma_{4\times4}$ can be diagonalized with a symplectic matrix U which makes the change of coordinates [45],

$$\overline{\sigma}_{4\mathrm{D}} = U\sigma_{4\mathrm{D}}U^T = \begin{pmatrix} \varepsilon_1 & 0 & 0 & 0 \\ 0 & \varepsilon_1 & 0 & 0 \\ 0 & 0 & \varepsilon_2 & 0 \\ 0 & 0 & 0 & \varepsilon_2 \end{pmatrix}, \quad U = \begin{pmatrix} 0 & 1 & 0 & 0 \\ -1 & 0 & 0 & 0 \\ 0 & 0 & 0 & 1 \\ 0 & 0 & -1 & 0 \end{pmatrix}. \tag{2.25}$$

We have a following relation by the determination of Eq. (2.24) and (2.25),

$$\det(\sigma_{4\mathrm{D}}) = \det(\overline{\sigma}_{4\mathrm{D}}) = \varepsilon_1^2\varepsilon_2^2 \quad \Rightarrow \quad \varepsilon^{4\mathrm{D}} = \sqrt{\det(\sigma_{4\mathrm{D}})} = \sqrt{\det(\overline{\sigma}_{4\mathrm{D}})} = \varepsilon_1\varepsilon_2 \tag{2.26}$$

ε^{4D} $(=\varepsilon_1\varepsilon_2)$ is called a four dimensional emittance or an intrinsic emittance [46–48]. Also, the relation between 2D emittances and 4D emittances is

$$\varepsilon_1\varepsilon_2 \leq \varepsilon_x\varepsilon_y. \tag{2.27}$$

When the beam does not have the x-y coupling correlation, the projected emittance is equal to the 4D emittance. Moreover, the coupling constant which is a ratio of the 4D and 2D emittances can be defined as

$$C = \sqrt{\frac{\varepsilon_x\varepsilon_y}{\varepsilon_1\varepsilon_2}} - 1 \geq 0. \tag{2.28}$$

For a decoupling beam $C = 0$, and for a coupling beam $C > 0$.

Chapter 3

Accelerator Facility for experiments

We performed THz and Channeling radiation experiments at the electron photoinjector of the Fermilab Accelerator Science and Technology (FAST) facility [18]. The FAST facility consists of the injector, superconducting accelerating structures for beam acceleration into the rest of the linac or to a storage ring. Figure 3.1 shows the layout of the FAST's facility. The storage ring is called IOTA (Integrable Optics Test Accelerator), which is built for research on nonlinear integrable optics, beam dynamics of space charge effects and their compensation, and beam cooling [17]. We carried out the experiments in the 50 MeV linac section (low energy beamline). In this section, we introduce the photoinjector and beam parameters for our experiments.

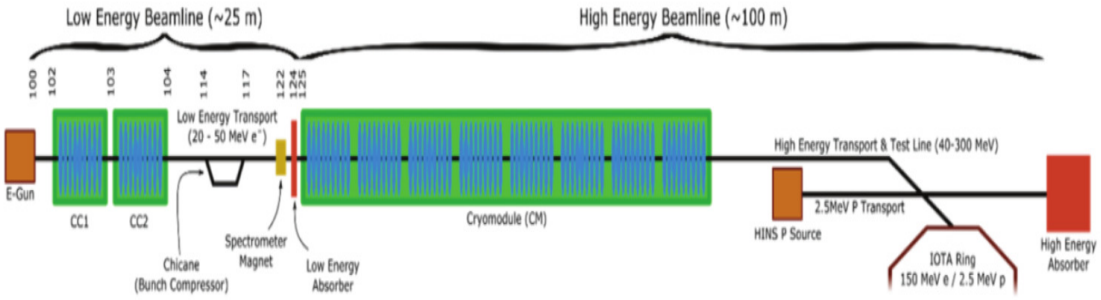

FIGURE 3.1: The layout of the FAST's facility [17].

3.1 FAST Photoinjector

The 50 MeV section (low energy bamline) of the photoinjector consists of a Cs_2Te photocathode RF gun with a normal conducting 1.5 cell cavity, two TESLA style 9-cell superconducting cavities, normal and skew quadrupole magnets, a chicane, a vertical bending magnet for beam extraction, and a beam dump. The layout and basic parameters of the photoinjector are shown in Figure 3.2 and Table 3.1.

The photocathode of the FAST injector is composed of a 10 mm diameter molybdenum disk coated with the semiconductor Cs_2Te. Each electron bunch is produced by irradiating the photocathode with an ultraviolet laser pulse with a wavelength of 263 nm. A bunch train has 3000 bunches, has a duration of 1 ms and the train repeats at 5 Hz. The RF gun, which is identical to the one developed at DESY for the FLASH facility [49], is operated at a peak accelerating gradient of 45 MeV/m and can accelerate electrons to ∼5 MeV. Also, it is surrounded by two identical solenoid coils (bucking and main coils) to focus the electron beam transversely or to control the magnetic field at the cathode, as shown in the left side in Fig. 3.2.

The main solenoid coil downstream of the cathode is used to cancel the defocusing effect at the exit of the RF gun and to suppress the emittance growth induced by the space charge effect. However, a nonzero axial magnetic field on the cathode imparts angular momentum and hence angular divergence which leads to emittance growth. A bucking solenoid coil is used to cancel the magnetic field from the main solenoid on the photocathode ($B_z(z = 0) = 0$). The optimum coil currents are found by minimizing the measured beam emittance. The expected normalized beam emittance, longitudinal bunch length, and energy spread after the RF gun are about <2 μm [50], 3 ps, and <0.2 % at 200 pC, respectively.

On the other hand, an electron beam needs to have finite angular momentum (a magnetized beam) for generating a flat beam ($\varepsilon_x/\varepsilon_y \neq 1$). Also, a high emittance ratio requires strong magnetic fields ($B_z(z = 0) \neq 0$) on the cathode, mentioned in Sec. 6.6. We realize a strong magnetic field on the photocathode by the combination of the two solenoid coils whose peak fields are 0.28 T at the maximum current of 500 A, and then the emittance ratio will be achieved to be over 200 [51–53].

The electron beam with an energy of 5 MeV after the RF gun is accelerated up to ∼50 MeV through the two superconducting structures (CC1 and CC2) in their own cryomodules cooled to 2 K. The accelerating gradients of CC1 and CC2 are ∼16 MV/m and ∼20 MV/m, respectively. Usable RF phases of them range from -35 degrees to 35 degrees and we produce an energy chirped beam using off-crest RF phases. Also,

all cavities (RF gun and CC1&2) in the FAST photoinjector are operated at an RF frequency of 1.3 GHz with a repetition rate of 5 Hz.

The electron beams with an energy of 50 MeV after CC2 travel through three skew quadrupole magnets to remove the angular momentum from a magnetized beam and five normal quadrupole magnets and are sent either to the chicane or the straight line corresponding to requirements for each experiment. The four dipole magnets consisting of the chicane provide bending angles of (-, +, +, -) 18 degrees, respectively, yielding a longitudinal dispersion of M_{56}. M_{56} is the matrix element that connects the path difference to the energy deviation and is given by $M_{56} = \int \frac{\eta_x}{\rho} ds = -0.18$ m, where ρ is the bend radius of each dipole magnet. In the middle of the chicane, a slit-mask with spacings and widths of 950 μm and 50 μm and a skew quadrupole magnet with an effective length of 128 mm are installed for the THz experiments.

After the chicane, a chamber with a goniometer was installed for the channeling radiation experiments. The goniometer, was developed at the Helmholtz Zentrum Dresden Rossendorf (HZDR), has an Al foil for detector calibration, a diamond crystal for CR radiation, and a clear aperture for beam commissioning. Details of this goniometer will be mentioned in Sec. 9.1. The electron beams are bent by the dipole magnet positioned downstream of the goniometer into the beam dump. This dipole magnet provides a kick of 22.5 degrees and requires an integrated field of 640 G-m at a 50 MeV beam energy.

The normal and skew quadrupole magnets used to control the electron beam sizes and transverse beam couplings in the beamline have a maximum gradient of 6.6 T/m at an energy of 50 MeV, their bore diameter is 54.6 mm, and the effective magnet length is 167 mm. Also, eight steering magnets are inserted in the beamline to correct the electron beam trajectory. Each steering magnet is capable of a maximum kick of 7.5 mrad to a 50 MeV electron beam. Table 3.2 shows magnet parameters for a 50 MeV electron beam. The effective magnetic length of the skew quadrupole magnet in the chicane is different from that of the other skew quads in the straight line, as mentioned above.

Several yttrium aluminum garnet (YAG) screens and electromagnetic beam-position monitors (BPMs) are available along the beamline to respectively measure the beam transverse profile and beam centroid position. Two YAG screen monitors (at X120 and X121) are positioned before and after the goniometer, and we estimate the beam sizes at the crystal by using these two monitors and the transfer matrix. Also, an Al foil is installed at X121 to generate transition radiation for THz radiation experiments. The Al foil is placed close to the X121 screen monitor. A screen monitor at X124 inserted downstream of the vertical bending magnet is used to obtain the beam energy and the energy spread by measuring the beam size and the vertical shift of the electron beam.

TABLE 3.1: Injector parameters

Parameters	Value
Beam energy after gun	5 MeV
Maximum beam energy	<50 MeV
Bunch charge (Nominal)	<10 fC - 3.2 nC (200 pC)
Bunch frequency (Nominal)	0.5-9 MHz (3 MHz)
RF repetition (Nominal)	1-5 Hz (5 Hz)
Macropulse duration	1 ms
Accelerating frequency	1.3 GHz
Normalized emittance	$\sim$2 μm
Peak operational gradients in (CC1, CC2)	(16 , 20) MV/m
Bunch length (Nominal)	0.9 - 70 ps (5 ps)
Uncorrelated energy spread	<0.2%
Chicane longitudinal dispersion M_{56}	-0.18 m
Chicane horizontal dispersion η	0.32 m

TABLE 3.2: Magnet parameters for a 50 MeV electron beam.

Magnets	Max. current	Max. magnet field	Kick angle	Effective length (bore diameter)
Solenoid coil (main and bucking)	500 A	0.28 T	—	—
Vertical dipole magnet	7.7 A	640 G-m	22.5 mrad	265.3 mm
Steering magnet	7.6 A	12.5 G-m	7.5 mrad	—
Dipole magnet (chicane)	—	—	18 degrees	264.7 mm
Quadrupole magnet	9.0 A	6.6 T/m	—	167 mm (54.6 mm)

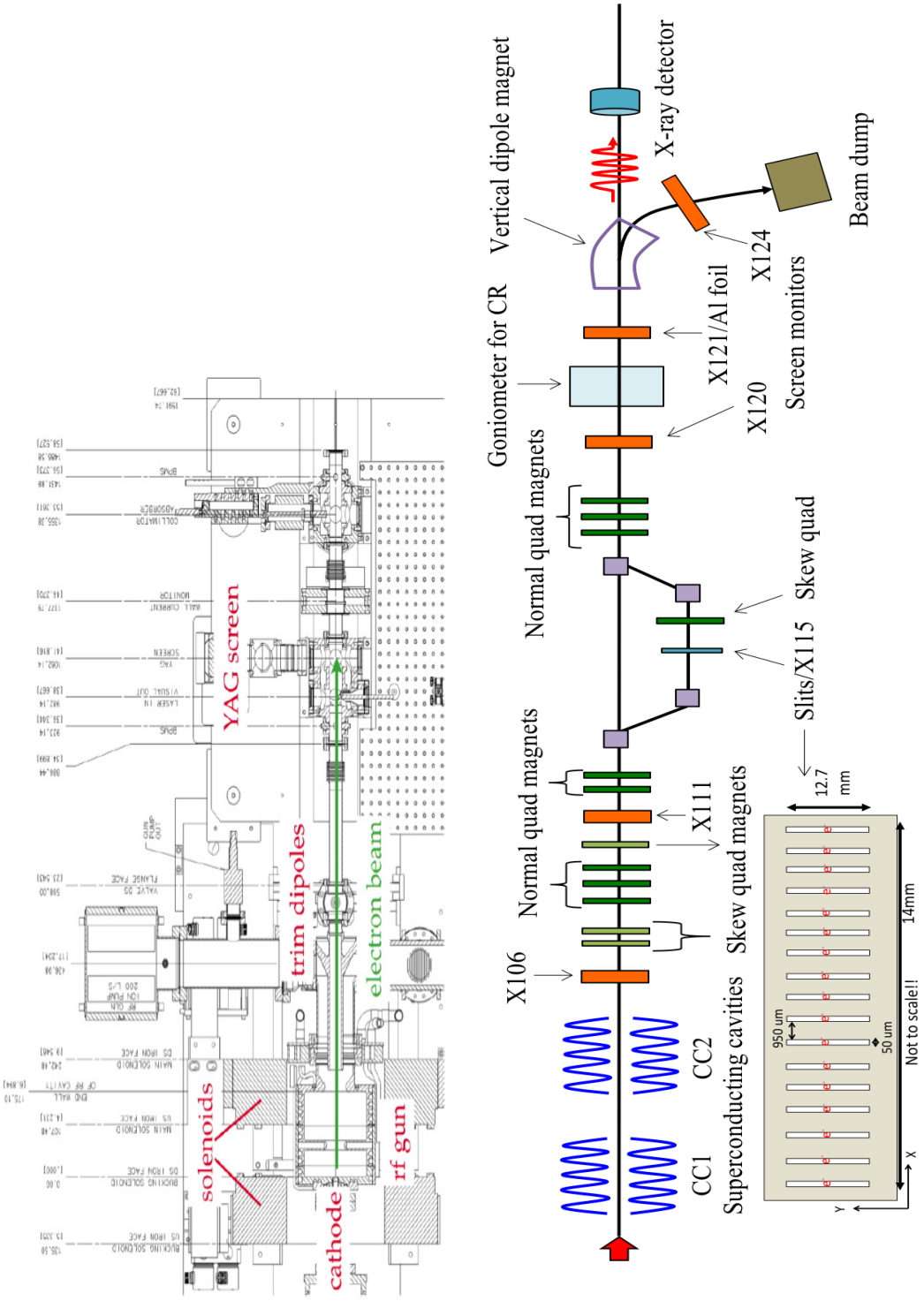

FIGURE 3.2: Layout of the FAST photoinjector. The left figure represents the RF gun and the 5MeV beamline [17], and the right figure represents the overview of the 50 MeV beamline.

Chapter 4

Magnetic chicane

A magnetic chicane consists of four identical dipole magnets which have the same magnetic field, magnetic length, and bending angle. Each dipole magnet is placed so that the polarities of the first and the fourth dipole magnets are opposite with respect to those of the second and third dipole magnets, which is a symmetric geometry at the center of the chicane [40]. In a chicane, dispersion occurs due to dipole magnets and is canceled at the exit of the chicane. Figure 4.1 shows a simplified magnetic chicane. The magnetic chicane is generally used for relative bunch lengthening or shortening of an electron beam or for energy collimation [54–58]. We use the chicane for bunch compression and/or de-compression in THz generation experiments. In the CR experiments we use it for mitigating the dark current generated at the photocathode using the energy difference between the dark current and the main electron beam.

The particle trajectory traveling through a chicane depends on the particle energy. The colored lines in Fig. 4.1 represent particle trajectories with different energies: higher energy, mean energy, lower energy. In a chicane, higher energy particles (green line) go through the inside of the central trajectory of the mean energy particles (blue line). Conversely, lower energy particles (red line) pass through the outside of the central trajectory [40]. When an electron beam with a correlation between the longitudinal position and energy (energy chirped beam) enters a magnetic chicane, it is shortened or lengthened longitudinally at the exit of the chicane. The compression ratio depends on values of an energy chirp h and a chicane parameter M_{56}. Here, a magnetic chicane composing of four rectangular magnets installed in the FAST beamline is described.

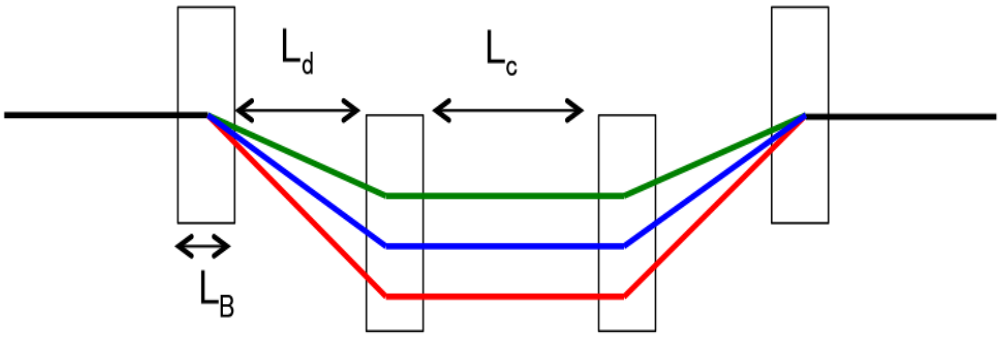

FIGURE 4.1: Layout of a magnet chicane. Red, blue, and green lines represent particle trajectories with different energies.

4.1 Chicane parameters from path length difference

The path length S_1 of a reference trajectory from the entrance of the first dipole magnet to the exit of the fourth dipole magnet is

$$S_1 = 4\frac{L_B}{\sin\theta_0}\theta_0 + 2\frac{L_d}{\cos\theta_0} + L_c, \tag{4.1}$$

where L_B is the magnetic length, L_d is the distance between the first dipole and the second dipole magnets, L_c is the distance between the second dipole and third dipole magnets, and θ_0 is the bending angle of the dipole magnets. Also, the difference of the path length for an energy spread δ (off-momentum) is

$$S_2 = 4\frac{L_B}{\sin\theta_1}\theta_1 + 2\frac{L_d}{\cos\theta_1} + L_c. \tag{4.2}$$

Here, θ_1 means the bending angle for off-momentum ($\delta \neq 0$), and there is the following relation between the two bending angles,

$$\theta_1 = \frac{\theta_0}{1+\delta}. \tag{4.3}$$

The difference of the path length for different energy particles in the chicane can be written as

$$\begin{aligned} \Delta S &= S_2 - S_1 = 4L_B\left(\frac{\theta_1}{\sin\theta_1} - \frac{\theta_0}{\sin\theta_0}\right) + 2L_d\left(\frac{1}{\cos\theta_1} - \frac{1}{\cos\theta_0}\right) \\ &\sim 2L_B\frac{\theta_1^2 - \theta_0^2}{3} + L_d\left(\theta_1^2 - \theta_0^2\right). \end{aligned} \tag{4.4}$$

Using Eq. (4.3), ΔS is

$$\begin{aligned}\Delta S &= \frac{2}{3}L_B\left[\left(\frac{\theta_0}{1+\delta}\right)^2-\theta_0^2\right]+L_d\left[\left(\frac{\theta_0}{1+\delta}\right)^2-\theta_0^2\right] \\ &= \theta_0^2\left[\left(\frac{1}{1+\delta}\right)^2-1\right]\left(\frac{2}{3}L_B+L_d\right). \end{aligned} \tag{4.5}$$

Also, for a small momentum deviation, the following approximation can be used

$$\left(\frac{1}{1+\delta}\right)^{-2} \sim 1-2\delta+3\delta^2-4\delta^3+\cdots. \tag{4.6}$$

As a result, Eq. (4.5) becomes

$$\Delta S \sim -2\theta_0^2\delta\left(\frac{2}{3}L_B+L_d\right)+3\delta^2\theta_0^2\left(\frac{2}{3}L_B+L_d\right)-4\delta^3\theta_0^2\left(\frac{2}{3}L_B+L_d\right). \tag{4.7}$$

In general, the difference of the path length between the reference particle and the particle with the energy spread δ can be written as

$$\Delta S(=S_2-S_1) \sim M_{56}\delta+T_{566}\delta^2+U_{5666}\delta^3+o(\delta^4), \tag{4.8}$$

where $M_{56}, T_{566}, U_{5666}$ are 1st, 2nd, and 3rd order longitudinal dispersions in the chicane, respectively. By comparing Eq. (4.7) and Eq. (4.8), we can get the following relations

$$M_{56} = -2\theta_0^2\left(\frac{2}{3}L_B+L_d\right). \tag{4.9}$$

$$T_{566} = 3\theta_0^2\left(\frac{2}{3}L_B+L_d\right) = -\frac{3}{2}M_{56}. \tag{4.10}$$

$$U_{5666} = -4\theta_0^2\left(\frac{2}{3}L_B+L_d\right) = 2M_{56}. \tag{4.11}$$

Here, $M_{56}<0,\ T_{566}>0,\ U_{5666}<0$

The longitudinal position of an electron beam after the chicane is

$$z_f = z_1+\Delta S. \tag{4.12}$$

Also, the energy spread is generally [59, 60]

$$\delta = a\delta_0+h_1z_1+h_2z_1^2+h_3z_1^3+\cdots, \tag{4.13}$$

where a is the damping factor, h_1 is the 1^{st} order energy chirp, h_2 is the 2^{nd} order energy chirp, and h_3 is the 3^{rd} order energy chirp. The detail of the energy chirp is described

in Sec. 6.1. By substituting Eq. (4.8) into Eq. (4.12), z_f becomes

$$\begin{aligned} z_f &\sim z_1 + M_{56}\delta + T_{566}\delta^2 + U_{5666}\delta^3 + \cdots \\ &\sim z_1 + M_{56}(a\delta_0 + h_1 z_1 + h_2 z_1^2) + T_{566}(a\delta_0 + h_1 z_1 + h_2 z_1^2)^2 \\ &\quad + U_{5666}(a\delta_0 + h_1 z_1 + h_2 z_1^2)^3 + \cdots \\ &= M_{56}a\delta_0 + (1 + M_{56}h_1)z_1 + (M_{56}h_2 + T_{566}h_1^2)z_1^2 + \cdots . \end{aligned} \tag{4.14}$$

When the electron beam is assumed to be a Gaussian distribution in the longitudinal direction, the rms bunch length can be given by

$$\sigma_{z_f} = \sqrt{M_{56}^2 a^2 \sigma_{\delta_0}^2 + (1 + M_{56}h_1)^2 \sigma_{z_1}^2 + (h_2 M_{56} + T_{566}h_1^2)^2 \sigma_{z_1}^2 + \cdots}, \tag{4.15}$$

For the full compression of the bunch length, the second and third terms in Eq. (4.15) should be zero. Therefore, the conditions for the maximum bunch compression are

$$1 + M_{56}h_1 = 0 \;\Rightarrow\; M_{56} = -\frac{1}{h_1}, \tag{4.16}$$

$$M_{56}h_2 + T_{566}h_1^2 = 0 \;\Rightarrow\; T_{566} = -\frac{h_2}{h_1^2}M_{56}. \tag{4.17}$$

Then, the minimum bunch length is given by

$$\sigma_{z_f,min} \sim a|M_{56}|\sigma_{\delta_0}. \tag{4.18}$$

Using Eq. (4.15), the ratio C of the initial bunch length $\sigma_{z_f}$to the final bunch length σ_{z_1} can be written as

$$C = \frac{\sigma_{z_f}}{\sigma_{z_1}} = \sqrt{M_{56}^2 a^2 \left(\frac{\sigma_{\delta_0}}{\sigma_{z_1}}\right)^2 + (1 + M_{56}h_1)^2 + (h_2 M_{56} + T_{566}h_1^2)^2 + \cdots}, \tag{4.19}$$

If the initial energy spread and other higher order terms can be ignored, the linear compression factor $\frac{1}{C_0}$ becomes

$$\frac{1}{C_0} = \frac{1}{|1 + M_{56}h_1|}. \tag{4.20}$$

To realize the high compression ratio, the chirp h_1 and the longitudinal dispersion M_{56} need to be chosen so that $1 + M_{56}h_1 = 0$ (Eq. (4.16)).

4.2 Maximum dispersion in the chicane

In a chicane, the dispersion between the second and the third dipole magnets is maximum and has a constant value. The transfer matrix M_{mid} at the center between the two dipole magnets can be written as

$$M_{mid} = \mathrm{Drift}(\frac{\mathrm{d}_2}{2})\ \mathrm{Dipole}(\rho, \theta_0)\ \mathrm{Drift}(\mathrm{d}_1)\ \mathrm{Dipole}(-\rho, -\theta_0) \tag{4.21}$$

where d_1 is the drift space between the first and the second dipole magnets, d_2 is the drift space between the second and the third dipole magnets. The transfer matrix M_{mid} at the center of the chicane becomes

$$\mathrm{M_{mid}} = \begin{pmatrix} 1 & M_{12} & 0 & 0 & 0 & M_{16} \\ 0 & 1 & 0 & 0 & 0 & 0 \\ 0 & 0 & M_{33} & M_{34} & 0 & 0 \\ 0 & 0 & M_{43} & M_{44} & 0 & 0 \\ 0 & M_{52} & 0 & 0 & 1 & M_{56} \\ 0 & 0 & 0 & 0 & 0 & 1 \end{pmatrix}. \tag{4.22}$$

$$M_{12} = d_1 + \frac{d_2}{2} + 2\rho \sin\theta_0, \tag{4.23}$$

$$M_{16} = -2 \tan\frac{\theta_0}{2}(d_1 + \rho \sin\theta_0), \tag{4.24}$$

$$M_{33} = \cos 2\theta_0 - \frac{(d_1 + d_2)\sin 2\theta_0}{2\rho} + \frac{d_1 d_2 \sin^2\theta_0}{2\rho^2}, \tag{4.25}$$

$$M_{34} = d_1 \cos^2\theta_0 + \rho \sin 2\theta_0 + \frac{d_2 \cos 2\theta_0}{2} - \frac{d_1 d_2 \sin 2\theta_0}{4\rho}, \tag{4.26}$$

$$M_{43} = \frac{\sin\theta_0\,(-2\rho\cos\theta_0 + d_1 \sin\theta_0)}{\rho^2}, \tag{4.27}$$

$$M_{44} = \cos 2\theta_0 - \frac{d_1 \sin 2\theta_0}{2\rho}, \tag{4.28}$$

$$M_{52} = M_{16}, \tag{4.29}$$

$$M_{56} = 4\tan^2\frac{\theta_0}{2}(d_1 + \rho\sin\theta_0) - 2\rho(\theta_0 - \sin\theta_0). \tag{4.30}$$

The maximum dispersion η_{max} in the chicane is

$$\eta_{max} = M_{16} = -2\tan\frac{\theta_0}{2}(d_1 + \rho\sin\theta_0). \tag{4.31}$$

Also, the transfer matrix $M_{chicane}$ of the chicane is

$$M_{chicane} = \mathrm{Dipole}(-\rho, -\theta_0)\ \mathrm{Drift}(\mathrm{d}_1)\ \mathrm{Dipole}(\rho, \theta_0)\ \mathrm{Drift}(\frac{\mathrm{d}_2}{2})\ M_{mid} \tag{4.32}$$

$$= \begin{pmatrix} 1 & M_{12} & 0 & 0 & 0 & 0 \\ 0 & 1 & 0 & 0 & 0 & 0 \\ 0 & 0 & M_{33} & M_{34} & 0 & 0 \\ 0 & 0 & M_{43} & M_{44} & 0 & 0 \\ 0 & 0 & 0 & 0 & 1 & M_{56} \\ 0 & 0 & 0 & 0 & 0 & 1 \end{pmatrix}. \tag{4.33}$$

$$\begin{aligned}
M_{12} &= 2d_1 + d_2 + 4\rho\sin\theta_0, \\
M_{33} = M_{44} &= \frac{2d_1^2\rho + 4d_1d_2\rho\cos 2\theta_0 - 2\rho\left(d_1^2 + 2d_1d_2 - 4\rho^2\right)\cos 4\theta_0}{8\rho^3} \\
&\quad + \frac{-2d_1^2d_2\sin 2\theta_0 + d_1^2d_2\sin 4\theta_0 - 8d_1\rho^2\sin 4\theta_0 - 4d_2\rho^2\sin 4\theta_0}{8\rho^3}, \\
M_{34} &= \frac{(2\rho\cos 2\theta_0 - d_1\sin 2\theta_0)\left(2d_1\rho + 2(d_1+d_2)\rho\cos 2\theta_0 + (-d_1d_2 + 4\rho^2)\sin 2\theta_0\right)}{4\rho^2}, \\
M_{43} &= \frac{\sin\theta_0\left(-2\rho\cos\theta_0 + d_1\sin\theta_0\right)\left(d_1d_2 + \left(-d_1d_2 + 4\rho^2\right)\cos 2\theta_0 - 2\left(d_1+d_2\right)\rho\sin 2\theta_0\right)}{4\rho^2}, \\
M_{56} &= 8\tan^2\frac{\theta_0}{2}(d_1 + \rho\sin\theta_0) - 4\rho(\theta_0 - \sin\theta_0).
\end{aligned} \tag{4.34}$$

The dispersion at the exit of the chicane is $\eta = 0$ due to $M_{16} = 0$ in Eq. (4.33). Therefore, the chicane composing of the rectangular magnets is an achromatic optics - the transverse phase space varianles are independent of the energy. Since the drift space d_1 is

$$d_1 = \frac{L_d}{\cos\theta_0}, \tag{4.35}$$

M_{56} can be written as

$$\begin{aligned}
M_{56} &\sim 2\theta_0^2(L_d + L_B) - \frac{2L_B\theta_0^2}{3} \\
&= 2\theta_0^2\left(L_d + \frac{2}{3}L_B\right).
\end{aligned} \tag{4.36}$$

The absolute value of Eq. (4.36) agrees with Eq. (4.9).

4.3 Coherent Synchrotron Radiation

When electron beams are bent with a magnet such as a dipole magnet, synchrotron radiation (SR) is emitted [61, 62]. The radiation wavelength λ which depends on the beam energy is given by $\lambda \sim \rho/\gamma^3$, where ρ is the bending radius of a dipole magnet. Radiation emitted at wavelengths λ larger than the bunch length σ, is called the coherent synchrotron radiation (CSR), whose intensity is enhanced [23, 24]. For $\sigma_z \ll \rho/\gamma^3$, the

radiation is fully coherent. CSR moving with speed of light can catch up with the bunch head after a distance $s = (24\rho^2\sigma_z)^{1/3}$, causes emittance growth of an electron beam and an increase in energy spread of an electron beam. The energy change along a bunch length with a Gaussian distribution due to the CSR wake field I_0 per dipole magnet can be written as [63]

$$\frac{dE}{cdt} = -\frac{2Nr_0m_0c^2}{\sqrt{2\pi}(3\rho^2\sigma_z^4)^{1/3}} I_0\left(\frac{z}{\sigma_z}\right), \tag{4.37}$$

$$I_0(x) = \int_x^{-\infty} \frac{dx'}{(x-z')}\frac{\partial}{\partial x'} e^{-x'^2/2}. \tag{4.38}$$

where r_0 is the classical electron radius, m_0c^2 is the rest mass energy of an electron, and N is the number of electrons. The characteristic of the CSR wake I_0 is that the head of the bunch gains energy while the tail loses energy [63]. Integrating Eq. (4.37) over the whole bunch, the energy change ΔE and the rms energy spread are given by [64, 65]

$$\langle \Delta E \rangle = \int_{-\infty}^{\infty} d(\xi)\lambda(\xi)\frac{dE(\xi)}{cdt} \sim -0.35\frac{Nr_eL_B}{\gamma(\rho^2\sigma_z^4)^{1/3}}, \tag{4.39}$$

$$\sigma_E = \frac{2Nr_0m_0c^2L_B}{\sqrt{2\pi}(3\rho^2\sigma_z^4)^{1/3}}\sqrt{\langle I_0(x)^2\rangle - \langle I_0(x)\rangle^2} \sim 0.23\frac{Nr_eL_B}{\gamma(\rho^2\sigma_z^4)^{1/3}}, \tag{4.40}$$

where L_B is the dipole length. CSR is significant for a bunch with high charge, low energy and a short bunch length, and when the bending radius is short.

CSR kick to an electron beam causes projected emittance growth but the slice emittance does not change. From Eq. (2.23), the beam emittance kicked by CSR can be computed as [66]

$$\begin{aligned}\varepsilon &= \sqrt{\langle x^2\rangle\langle x'^2\rangle - \langle xx'\rangle^2} \\ &= \sqrt{\langle (x_0+\eta\delta_{CSR})^2\rangle\langle (x_0'+\eta'\delta_{CSR})^2\rangle - \langle (x_0+\eta\delta_{CSR})(x_0'+\eta'\delta_{CSR})\rangle^2} \\ &\sim \varepsilon_0\sqrt{\left(1+\frac{H}{\varepsilon_0}\delta_{CSR}^2\right)},\end{aligned} \tag{4.41}$$

where

$$H = \frac{\eta^2 + (\beta\eta' + \alpha\eta)^2}{\beta} \tag{4.42}$$

Here, ε_0 is the emittance without the CSR effect to the electron beam and δ_{CSR} is the energy spread induced by CSR. Therefore, the projected emittance is increased due to the CSR effects. From Eq. (4.41) and (4.42), the projected emittance growth caused by CSR can be minimized when the H function is small (which requires low dispersion), and some CSR mitigation methods have been proposed in [65, 67].

Chapter 5

Energy spread and beam emittance

Here, we introduce methods to obtain the energy spread of an electron beam and a four-dimensional beam emittance. An electron beam traveling through a solenoid coil and a tilted magnet has transverse ($x-y$ planes) beam coupling. The projected emittance (2D emittance) of an electron beam with thia coupling is larger than the intrinsic beam emittance. To obtain a small beam emittance, the beam coupling should be corrected. Also, the generation of a flat beam requires the removal of the x-y' and x'-y correlations from a magnetized beam. When a four-dimensional beam matrix is identified, a four-dimensional beam emittance can be obtained from the square root of the determinant of the beam matrix, and also the beam coupling can be corrected.

5.1 Method of energy spread measurement

The energy spread can be obtained by focusing beam at a location with dispersion. The beam size at a screen monitor in the dispersive place is given by [42]:

$$\sigma = \sqrt{\varepsilon\beta + (\eta\sigma_\delta)^2}, \tag{5.1}$$

where ε is the beam emittance, β is the beta function, η is the dispersion, and σ_δ is the rms energy spread at the screen monitor. When the beta function is focused at the screen monitor so that $\varepsilon\beta$ is smaller than $(\eta\sigma_\delta)^2$, the beam size at the screen monitor is approximately written as

$$\sigma \sim |\eta\sigma_\delta| \quad \Rightarrow \quad |\sigma_\delta| = \frac{\sigma}{|\eta|}. \tag{5.2}$$

Therefore, the energy spread can be measured by minimizing the beam size (beta function) at a screen monitor in a dispersive place. Also, the dispersion η is decided by the bending angle and the bending radius of the dipole magnet. In the FAST beamline, the energy spread is measured with the YAG screen at X124 installed downstream of the vertical dipole magnet, see Fig. 3.2.

5.2 Method of transverse emittance measurement

Assuming a straight section without dispersion (M_{16}=0). The beam matrices $\sigma_{s_0}, \sigma_{s_1}$ at two locations s_0, s_1 are related as $\sigma_{s_1} = M\sigma_{s_0}M^{\mathrm{T}}$, where M is the transfer matrix between s_0 and s_1. The transfer matrix M can be calculated from linear optics. Assuming no linear tranverse coupling between the two locations, the observable second moments at the two locations are related as

$$\langle x^2\rangle_{s_1} = M_{11}^2\langle x^2\rangle_{s_0} + 2M_{11}M_{12}\langle xx'\rangle_{s_0} + M_{12}^2\langle x'^2\rangle_{s_0}, \tag{5.3}$$

$$\langle y^2\rangle_{s_1} = M_{33}^2\langle y^2\rangle_{s_0} + 2M_{33}M_{34}\langle yy'\rangle_{s_0} + M_{34}^2\langle y'^2\rangle_{s_0}, \tag{5.4}$$

$$\langle xy\rangle_{s_1} = M_{11}M_{33}\langle xy\rangle_{s_0} + M_{12}M_{33}\langle x'y\rangle_{s_0} + M_{11}M_{34}\langle xy'\rangle_{s_0} + M_{12}M_{34}\langle x'y'\rangle_{s_0} \tag{5.5}$$

These can be written symbolically as

$$\vec{b} = A \cdot \vec{Z} \tag{5.6}$$

where $\vec{b}$ represents the measured moments at s_1, A is a matrix with the elements shown above and $\vec{Z}$ represents the unknown second moments at s_0 which are to be found. Since $\langle x^2\rangle$, $\langle y^2\rangle$, and $\langle xy\rangle$ can be measured with a beam screen monitor in one measurement, we should measure them with more than three different beam optics configurations to obtain a precise emittance. Using the χ^2-method, the 10 independent elements in $\vec{Z}$ at s_0 are reconstructed [68]:

$$\chi^2 = \sum_{i=1}^{n}\left(\frac{observed\ value_{(i)} - expected\ value_{(i)}}{standard\ deviation_{(i)}}\right)^2. \tag{5.7}$$

The "$expected\ value_{(i)}$" (the right-hand side of Eq. (5.3)$\sim$(5.5)) can be sought by minimizing χ^2. If we have n measurements of the 3 observable moments, we have the $3n$ dimensional vector

$$\vec{b} = \left[\langle x_{(1)}^2\rangle \cdots \langle x_{(n)}^2\rangle \ \ \langle y_{(1)}^2\rangle \cdots \langle y_{(n)}^2\rangle \ \ \langle xy_{(1)}\rangle \cdots \langle xy_{(n)}\rangle\right]_{s_1}^{\mathrm{T}}, \tag{5.8}$$

The unknown moments at s_0 are represented as the 10 dimensional vector

$$\vec{Z} = \left[\langle x_0^2\rangle \ \langle x x_0'\rangle \ \langle x_0'^2\rangle \ \langle y_0^2\rangle \ \langle y y_0'\rangle \ \langle y_0'^2\rangle \ \langle x y_0\rangle \ \langle x' y_0\rangle \ \langle x y_0'\rangle \ \langle x' y_0'\rangle\right]^{\mathrm{T}}_{s_0}, \tag{5.9}$$

(5.10)

The $3n \times 10$ dimensional matrix A has as its nth block the 3 rows as

$$\begin{bmatrix} M_{11}^{2(n)} & 2M_{11}^{(n)}M_{12}^{(n)} & M_{12}^{2(n)} & 0 & 0 & 0 & 0 & 0 & 0 & 0 \\ 0 & 0 & 0 & M_{33}^{2(1)} & 2M_{33}^{(n)}M_{34}^{(n)} & M_{34}^{2(n)} & 0 & 0 & 0 & 0 \\ 0 & 0 & 0 & 0 & 0 & 0 & M_{11}^{(n)}M_{33}^{(n)} & M_{12}^{(n)}M_{33}^{(n)} & M_{11}^{(n)}M_{34}^{(n)} & M_{12}^{(n)}M_{34}^{(n)} \end{bmatrix} \tag{5.11}$$

Eq. (5.7) can be written as

$$\chi^2 = \sum_{i=1}^{3n}\left[b_i - \sum_{j=1}^{10} A_{ij}Z_j\right]^2 \tag{5.12}$$

To minimize $(A\cdot\vec{Z}-\vec{b})^2$, the partial derivatives of χ^2 should be zero.

$$\begin{pmatrix} \partial\chi^2/\partial Z_1 \\ \cdots \\ \partial\chi^2/\partial Z_{10} \end{pmatrix}_{s_1} = 2\begin{pmatrix} \sum_{i=1}^{3n}\sum_{j=1}^{10} A_{ij}A_{i1}Z_j \\ \cdots \\ \sum_{i=1}^{3n}\sum_{j=1}^{10} A_{ij}A_{i10}Z_j \end{pmatrix} - 2\begin{pmatrix} \sum_{i=1}^{3n} b_iA_{i1} \\ \cdots \\ \sum_{i=1}^{3n} b_iA_{i10} \end{pmatrix} = \begin{pmatrix} 0 \\ \cdots \\ 0 \end{pmatrix}. \tag{5.13}$$

Therefore, $A^TA\vec{Z} = A^T\vec{b}$, and we have for the desired moments at s_0, the solution

$$\vec{Z} = (A^TA)^{-1}A^T\vec{b}, \tag{5.14}$$

where $(A^TA)^{-1} = C$ is a symmetric $3n \times 3n$ covariance matrix. Since $\sigma^{4D}(=Z)$ can be found, the 4D emittance and twiss parameters at s_0 can be computed with Eq. (2.26) and Eq. (2.21).

5.2.1 Error propagation

The error of any scalar function $f(Z)$ is given by $\sigma_f^2 = (\nabla_Z f)^T C (\nabla_Z f)$, where C is the covariance matrix [43]. Here, f and $\nabla_Z f$ are

$$f = \begin{pmatrix} \beta_{x0} \\ \alpha_{x0} \\ \epsilon_{x0}^{2D} \\ \beta_{x0} \\ \alpha_{x0} \\ \epsilon_{x0}^{2D} \end{pmatrix}, \quad \nabla_Z f = \begin{pmatrix} \frac{\partial \beta_{x0}}{\partial \langle Z_1 \rangle} & \frac{\partial \alpha_{x0}}{\partial \langle Z_1 \rangle} & \frac{\partial \epsilon_{x0}}{\partial \langle Z_1 \rangle} & \frac{\partial \beta_{y0}}{\partial \langle Z_1 \rangle} & \frac{\partial \alpha_{y0}}{\partial \langle Z_1 \rangle} & \frac{\partial \epsilon_{y0}}{\partial \langle Z_1 \rangle} \\ \frac{\partial \beta_{x0}}{\partial \langle Z_2 \rangle} & \frac{\partial \alpha_{x0}}{\partial \langle Z_2 \rangle} & \frac{\partial \epsilon_{x0}}{\partial \langle Z_2 \rangle} & \frac{\partial \beta_{y0}}{\partial \langle Z_2 \rangle} & \frac{\partial \alpha_{y0}}{\partial \langle Z_2 \rangle} & \frac{\partial \epsilon_{y0}}{\partial \langle Z_2 \rangle} \\ \frac{\partial \beta_{x0}}{\partial \langle Z_3 \rangle} & \frac{\partial \alpha_{x0}}{\partial \langle Z_3 \rangle} & \frac{\partial \epsilon_{x0}}{\partial \langle Z_3 \rangle} & \frac{\partial \beta_{y0}}{\partial \langle Z_3 \rangle} & \frac{\partial \alpha_{y0}}{\partial \langle Z_3 \rangle} & \frac{\partial \epsilon_{y0}}{\partial \langle Z_3 \rangle} \\ \frac{\partial \beta_{x0}}{\partial \langle Z_4 \rangle} & \frac{\partial \alpha_{x0}}{\partial \langle Z_4 \rangle} & \frac{\partial \epsilon_{x0}}{\partial \langle Z_4 \rangle} & \frac{\partial \beta_{y0}}{\partial \langle Z_4 \rangle} & \frac{\partial \alpha_{y0}}{\partial \langle Z_4 \rangle} & \frac{\partial \epsilon_{y0}}{\partial \langle Z_4 \rangle} \\ \frac{\partial \beta_{x0}}{\partial \langle Z_5 \rangle} & \frac{\partial \alpha_{x0}}{\partial \langle Z_5 \rangle} & \frac{\partial \epsilon_{x0}}{\partial \langle Z_5 \rangle} & \frac{\partial \beta_{y0}}{\partial \langle Z_5 \rangle} & \frac{\partial \alpha_{y0}}{\partial \langle Z_5 \rangle} & \frac{\partial \epsilon_{y0}}{\partial \langle Z_5 \rangle} \\ \frac{\partial \beta_{x0}}{\partial \langle Z_6 \rangle} & \frac{\partial \alpha_{x0}}{\partial \langle Z_6 \rangle} & \frac{\partial \epsilon_{x0}}{\partial \langle Z_6 \rangle} & \frac{\partial \beta_{y0}}{\partial \langle Z_6 \rangle} & \frac{\partial \alpha_{y0}}{\partial \langle Z_6 \rangle} & \frac{\partial \epsilon_{y0}}{\partial \langle Z_6 \rangle} \end{pmatrix}. \tag{5.15}$$

Since the diagonal elements of σ_f^2 are $\sigma_{f_i} = \sqrt{f_{ii}}$, we have

$$\sigma_{f_1} = \sigma_{\beta_{x_0}}, \ \sigma_{f_2} = \sigma_{\alpha_{x_0}}, \ \sigma_{f_3} = \sigma_{\epsilon_{x0}^{2D}}, \tag{5.16}$$

$$\sigma_{f_4} = \sigma_{\beta_{y_0}}, \ \sigma_{f_5} = \sigma_{\alpha_{y_0}}, \ \sigma_{f_6} = \sigma_{\epsilon_{y0}^{2D}}. \tag{5.17}$$

Chapter 6

Theory and simulations for THz radiation with micro-bunched beams

We generate THz radiation with micro-bunched electron beams produced using a slit-mask placed within a magnetic chicane in the FAST photoinjector. Figure 6.1 shows the FAST injector and the phase space along the beamline. Using the slit-mask in the chicane, we create a longitudinally micro-bunched beam after the chicane by transversely slicing an energy chirped electron bunch at a location with horizontal dispersion. We describe the theory related to the micro-bunched beam structure, the beam optics, the simulation results of the micro-bunched beam and the expected THz spectra using coherent transition radiation (CTR) and a wiggler, as well as a method for observing the micro-bunched beam on a transverse screen monitor.

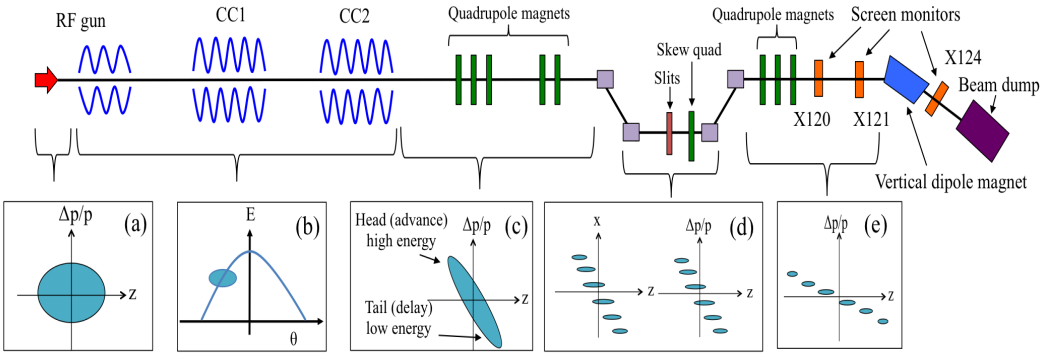

FIGURE 6.1: Phase space along the beamline.

6.1 Theory of an energy-chirped beam

An energy chirp represents a correlation between bunch length z and energy spread δ, which is defined by $h = \partial\delta/\partial z|_{z=0}$. An energy chirped beam can be produced by accelerating an electron beam on an off-crest RF phase in a cavity ((b) in Fig. 6.1) and is required for beam lengthening and shortening longitudinally in a magnetic chicane [60, 69–71].

When an electron beam with an energy E_0 and an energy spread δ_0 is accelerated in the cavity CC1, the electron beam energy E_1 can be written by [59, 60]

$$E_1 = E_0(1+\delta_0) + eV_1\cos(kz+\phi_1), \tag{6.1}$$

where ϕ_1, eV_1, and k are the accelerating phase, the accelerating gain, and the RF wave number in the CC1 cavity, respectively, and z is the longitudinal position of a particle. The reference particles are at the longitudinal center ($z = 0$). We choose the wave number k and the rms bunch length σ_z so that $k\sigma_z < \phi_1$. Then, $\cos(kz+\phi_1)$ is

$$\cos(kz+\phi_1) \sim \cos\phi_1 - (\sin\phi_1)kz - \frac{1}{2}(\cos\phi_1)(kz)^2 + \frac{1}{6}\sin\phi_1(kz)^3 + \cdots. \tag{6.2}$$

Substituting Eq. (6.2) into Eq. (6.1), the beam energy E_1 after the CC1 is

$$E_1 = E_{1c} + E_0\delta_0 - eV_1(kz)\sin\phi_1 - \frac{eV_1(kz)^2}{2}\cos\phi_1 + \frac{eV_1(kz)^3}{6}\sin\phi_1 + \cdots. \tag{6.3}$$

$$E_{1c} = E_0 + eV_1\cos\phi_1. \tag{6.4}$$

An energy spread of an electron beam after going through CC1 is given by

$$\begin{aligned}\delta_1 &= \frac{E_1 - E_{1c}}{E_{1c}} \\ &= \left(\frac{E_0}{E_{c1}}\right)\delta_0 - \frac{eV_1k\sin\phi_1}{E_{1c}}z - \frac{eV_1k^2\cos\phi_1}{2E_{1c}}z^2 + \frac{eV_1k^3\sin\phi_1}{6E_{1c}}z^3 + \cdots.\end{aligned} \tag{6.5}$$

We can obtain each energy chirp by comparing Eq. (6.5) with Eq. (4.13),

$$a = \frac{E_0}{E_{1c}}, \tag{6.6}$$

$$h_1 = -\frac{eV_1k\sin\phi_1}{E_{1c}}, \tag{6.7}$$

$$h_2 = -\frac{eV_1k^2\cos\phi_1}{2E_{1c}}, \tag{6.8}$$

$$h_3 = -\frac{eV_1k^3\sin\phi_1}{6E_{1c}}. \tag{6.9}$$

When the electron beam after passing through CC1 is accelerated in the next cavity CC2, the electron beam energy E_2 is

$$\begin{aligned} E_2 &= E_{1c}(1+\delta_1) + eV_2\cos(kz+\phi_2) \\ &\sim E_{1c} + E_0\delta_0 - eV_1(kz)\sin\phi_1 - \frac{eV_1(kz)^2\cos\phi_1}{2} + \frac{eV_1(kz)^3\sin\phi_1}{6} \\ &+ eV_2\cos\phi_2 - (eV_2(kz)\sin\phi_2) - \frac{eV_2(kz)^2\cos\phi_2}{2} + \frac{eV_2(kz)^3\sin\phi_2}{6} + \cdots \\ \\ &= E_{2c} + E_0\delta_0 + (-eV_1k\sin\phi_1 - eV_2k\sin\phi_2)z \\ &+ \frac{(-eV_1k^2\cos\phi_1 - eV_2k^2\cos\phi_2)}{2}z^2 \\ &+ \frac{(-eV_1k^3\sin\phi_1 - eV_2k^3\sin\phi_2)}{2}z^3 + \cdots, \end{aligned} \tag{6.10}$$

where $E_{2c} = E_{1c} + eV_2\cos\phi_2$, and we used Eq. (6.2) and (6.5). Therefore, the energy spread δ_2 of the electron beam after CC2 is

$$\begin{aligned} \delta_2 &= \frac{E_2 - E_{2c}}{E_{2c}} \\ &\sim (\frac{E_0}{E_{2c}})\delta_0 - \frac{eV_1k\sin\phi_1 - eV_2k\sin\phi_2}{E_{2c}}z \\ &+ \frac{-eV_1k^2\cos\phi_1 - eV_2k^2\cos\phi_2}{2E_{2c}}z^2 \\ &+ \frac{-eV_1k^3\sin\phi_1 - eV_2k^3\sin\phi_2}{6E_{2c}}z^3 + \cdots \end{aligned} \tag{6.11}$$

From Eq. (4.13), each energy chirp of an electron beam after CC2 is

$$a = \frac{E_0}{E_{2c}}, \tag{6.12}$$

$$h_1 = -\frac{eV_1k\sin\phi_1 + eV_2k\sin\phi_2}{E_{2c}}, \tag{6.13}$$

$$h_2 = -\frac{eV_1k^2\cos\phi_1 + eV_2k^2\cos\phi_2}{2E_{2c}}, \tag{6.14}$$

$$h_3 = -\frac{eV_1k^3\sin\phi_1 + eV_2k^3\sin\phi_2}{6E_{2c}}, \tag{6.15}$$

where $E_{2c} = E_0 + eV_1\cos\phi_1 + eV_2\cos\phi_2$.

The energy chirp can be produced by accelerating with an off-crest phase in either one or both cavities. Since off-crest acceleration lowers the beam energy, the two accelerating voltages are changed to keep the final energy fixed at ~35 MeV which is the value for ϕ_1=ϕ_2=±35° at the peak voltage gradients shown in Table 3.1. The constant beam energy simplifies operation by requiring no tuning of the dipole strengths in the chicane for each choice of RF phases. The energy chirps calculated with Eq. (6.13)-(6.15) are

TABLE 6.1: The final energy chirps for different RF phase in CC1 and CC2. h_1, h_2, and h_3 are the 1st, 2nd, 3rd order energy chirps, respectively.

RF phase	Energy chirp		
(ϕ_1, ϕ_2) [deg.]	h_1 [m^{-1}]	h_2 [m^{-2}]	h_3 [m^{-3}]
(+35 , -35)	-16	-223	-2025
(0 , +35)	-9	-124	-1125
(+35 , 0)	-7	99	-900
(-35 , 0)	7	99	900
(0 , -35)	9	124	1125
(-35 , -35)	16	223	2025

summarized in Table 6.1. Also, from Eq. (4.13), the rms energy spread is given by $\sigma_\delta = a\sigma_{\delta_0} + h_1\sigma_z + h_2\sigma_z^2 + h_3\sigma_z^3 + \cdots$, so the influence of the higher energy chirps (h_2, h_3, ...) on the energy spread is likely to be negligible for the nominal bunch length of ~3 ps.

6.2 Theory of a micro-bunched beam

The energy-chirped beam from the two cavities is sent to the chicane where the horizontal dispersion has negative values ((a), (b), (c) in Fig. 6.1). Electrons in the chicane are separated horizontally with higher energy (lower energy) electrons passing through the inside (outside) of the ideal orbit. The slit-mask in the middle of the chicane splits the beam horizontally into sections ((d) in Fig. 6.1). Beam transmission through the slit-mask is expected to be around 5% from the ratio of the slit width W to the slit spacing D. The particles passing through a slit opening are fully transmitted since the beam divergence at the slit-mask (= 0.7 mrad) is much smaller than the opening angle $W/t = 0.1$ rad where t is the thickness of the slit, while the particles passing through the tungsten are scattered at large angles and lost downstream of the mask. We confirmed this transmission with GEANT4 simulations [72] and show the simulation results later in Fig. 7.10 in Sec. 7.4.

In the bunch lengthening mode of operation, higher energy electrons after the chicane are at the bunch head while the lower energy electrons are at the bunch tail. The horizontally separated bunch after the slit-mask is transformed into a longitudinally separated beam (or into micro-bunches) after the chicane ((e) in Fig. 6.1). The lengthening increases the longitudinal separation between the micro-bunches.

The longitudinal width and spacing of the micro-bunches can be found using the transfer matrix. From Eq. (4.22) in Sec. 4.2, the 4×4 transfer matrix with phase space variables (x, x', z, δ) of the dogleg (from the entrance of the chicane to the slit-mask in

the middle of the chicane) is

$$\begin{pmatrix} x \\ x' \\ z \\ \delta \end{pmatrix}_s = \begin{pmatrix} 1 & M_{12} & 0 & M_{16} \\ 0 & 1 & 0 & 0 \\ 0 & M_{52} & 1 & M_{56} \\ 0 & 0 & 0 & 1 \end{pmatrix} \begin{pmatrix} x \\ x' \\ z \\ \delta \end{pmatrix}_1 . \tag{6.16}$$

The matrix elements are written in Eq. (4.23) - (4.30). The horizontal position of a particle at the slit-mask is given by $x_s = x_c + M_{16}\delta_1$, where $x_c = x_1 + M_{12}x'_1$, and where (x_1, x'_1) are the horizontal coordinates of the particle at the chicane's entrance. The energy deviation (constant through the chicane) is $\delta_1 (= \delta_s) = \delta_0 + hz_1$, where δ_0 is the deviation due to the uncorrelated energy spread, h is the energy chirp, and z_1 is the longitudinal coordinate of the particle at the chicane entrance. In terms of the transverse positions and δ_0, this can be written as

$$z_1 = \frac{(x_s - x_c)}{hM_{16}} - \frac{\delta_0}{h}. \tag{6.17}$$

The transfer matrix MC for the complete chicane can be similarly written down. For our purposes, the non-zero elements of interest in the (x, x', z, δ) planes are

$$\begin{aligned} MC_{11} = 1, \quad MC_{12} = 2M_{12}, \quad MC_{22} = 1, \\ MC_{55} = 1, \quad MC_{56} = 2M_{56}, \quad MC_{66} = 1, \end{aligned} \tag{6.18}$$

where M_{12}, M_{56} are given by the expressions in Eq. (4.23) and (4.30). The other non-zero elements $(MC_{33}, MC_{34}, MC_{43}, MC_{44})$ are not needed here and are omitted.

The longitudinal coordinate z_2 after the chicane is

$$z_2 = z_1 + MC_{56}\delta_1 = \frac{(1 + hMC_{56})}{hM_{16}}(x_s - x_c) - \frac{\delta_0}{h}. \tag{6.19}$$

Since the full slit width W is smaller than the rms beam size, we can assume that the beam distribution in the slits is uniform.

$$\langle x_s^2 \rangle = \frac{W^2}{12}, \quad \langle x_c^2 \rangle = \varepsilon\beta_S, \quad \langle \delta_0^2 \rangle = \sigma_{\delta,U}^2, \tag{6.20}$$

where ε is the un-normalized horizontal emittance, β_S is the beta function at the slits, and $\sigma_{\delta,U}$ is the uncorrelated rms relative energy spread in the chicane. We obtain the rms length of a micro-bunch $\sigma_{z_2,MB}$ as

$$\sigma_{z,MB}^2 = \left[\frac{(1 + hMC_{56})}{h\eta}\right]^2 \times \left\{\frac{W^2}{12} + \varepsilon\beta_S\right\} + \frac{\sigma_{\delta,U}^2}{h^2}, \tag{6.21}$$

where $\eta = M_{16} = -2\tan(\theta_0/2)(d_1 + \rho\sin\theta_0)$ is the dispersion at the slits. In most cases, the contribution of the betatron size dominates, so that we have approximately

$$\sigma_{z,MB} \approx \frac{|(1+hMC_{56})|}{|\eta h|}\sqrt{\beta_S \varepsilon}. \tag{6.22}$$

Eq. (6.21) shows that $\varepsilon\beta_S$ and $\sigma_{\delta,U}$ should be small to minimize the length of each micro-bunch and therefore create larger longitudinal separations between the micro-bunches.

Denoting the horizontal position at the ith slit by x_s^i, we have on average $\langle x_s^i - x_s^{i-1}\rangle = D$ where D is the slit spacing, while $\langle x_C^I - x_C^{I-1}\rangle = 0$. Hence the average longitudinal separation $\langle\Delta z\rangle$ after the chicane between particles which pass through neighboring slits is

$$|\langle\Delta z\rangle| = |\langle(z_2^i - z_2^{i-1})\rangle| = \frac{D}{|h\eta|}(|1+hMC_{56}|). \tag{6.23}$$

Here we have dropped the completely negligible differences in energy between particles at neighboring slits. The micro-bunched beam's widths and spacings computed for each energy chip are summarized in Table 6.3 in Section 6.4.

6.2.1 Frequency dependence on energy chirp

THz radiation can be generated by allowing the micro-bunched beam to traverse an Al foil. The fundamental frequency f_0 is determined by the separation between the micro-bunches for a comb structure beam and is given by

$$f_0 = \frac{c}{|\langle\Delta z\rangle|} = \frac{c|h\eta|}{D|1+hMC_{56}|}. \tag{6.24}$$

This equation is valid as long as the separation satisfies $|\langle\Delta z\rangle| \gg MC_{56}\sigma_{\delta,U}$ which is generally true, except in the vicinity of the maximum compression where $\langle\Delta z\rangle \to 0$. Figure 6.2 shows the fundamental frequency as a function of the energy chirp. The fundamental frequency can be changed by varying the energy chirp. From Fig. 6.2, the fundamental frequencies are about 0.3 THz, 0.33 THz, and 0.38 THz at h=-7, -9, and -16 m^{-1}, respectively, and 1.82 THz, 1.27 THz, and 0.77 THz at h=7, 9, and 16 m^{-1}, respectively. The fundamental frequency is zero when there is no chirp at $h = 0\,\mathrm{m}^{-1}$ and goes to large values close to the maximum compression as $h \to 1/(MC_{56}) \sim 5.6\,\mathrm{m}^{-1}$. While positive h values lead to larger fundamental frequencies, they also compress the entire bunch structure and lead to overlap between micro-bunches, and the frequency spectra are broadband rather than narrow-band. Figure 6.2 also shows that the fundamental frequency changes slowly beyond $|h| \approx 20\ \mathrm{m}^{-1}$, so there is no advantage in going beyond these chirp values. Micro-bunch widths, spacing, and fundamental frequencies computed for each energy chirp are summarized in Table 6.2.

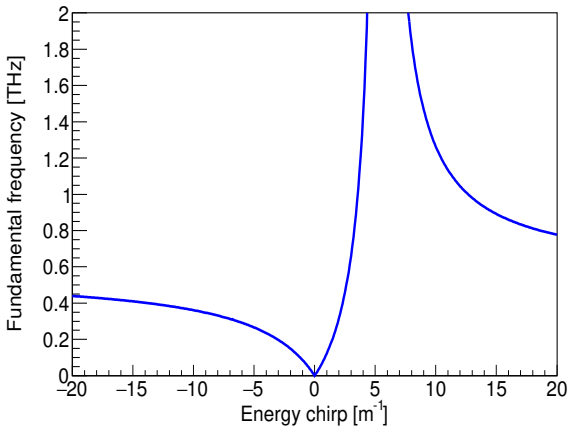

FIGURE 6.2: Fundamental frequency depending on energy chirps. The fundamental frequency becomes large near the maximum compression at $h = 5.6$ m^{-1}.

TABLE 6.2: Micro-bunch widths, spacing, and fundamental frequencies calculated analytically with Eq. (6.21), (6.23), and (6.24), respectively. $\phi_{i,rf} = 0°$ implies on-crest RF phase.

RF phase	Energy chirp	Width	Spacing	Fundamental freq.
$\phi_{1,rf}$, $\phi_{2,rf}$ [deg.]	[m^{-1}]	[mm]	[mm]	[THz]
(+35 , +35)	-16	0.09	0.72	0.42
(0 , +35)	-9	0.11	0.87	0.35
(+35 , 0)	-7	0.12	0.95	0.32
(-35 , 0)	7	0.02	0.11	2.73
(0 , -35)	9	0.03	0.19	1.54
(-35 , -35)	16	0.04	0.34	0.87

6.2.2 Observing micro-bunching in the transverse plane

A skew quadrupole magnet installed in the chicane can be used to confirm that a micro-bunched beam is produced prior to detecting the radiation. When the skew quadrupole is turned on in the chicane where the horizontal dispersion is non-zero, the vertical dispersion is generated downstream of the skew quadrupole via beam coupling. Due to the vertical dispersion after the chicane, the information on the beam separation in the horizontal plane (energy-plane) at the skew quadrupole is transferred to the vertical plane [73]. Using a Yttrium Aluminum Garnet (YAG) scintillating screen downstream of the chicane, we can observe the electron beam separation in the vertical plane. The vertical spacing can be found through the transfer matrix from the skew quadrupole in the chicane to the monitor downstream of the chicane. The phase space vectors at the

monitor and slit location are related via

$$\begin{pmatrix} x \\ x' \\ y \\ y' \\ z \\ \delta \end{pmatrix}_M = RM \cdot \begin{pmatrix} 1 & 0 & 0 & 0 & 0 & 0 \\ 0 & 1 & -k_S & 0 & 0 & 0 \\ 0 & 0 & 1 & 0 & 0 & 0 \\ -k_S & 0 & 0 & 1 & 0 & 0 \\ 0 & 0 & 0 & 0 & 1 & 0 \\ 0 & 0 & 0 & 0 & 0 & 1 \end{pmatrix} \begin{pmatrix} x \\ x' \\ y \\ y' \\ z \\ \delta \end{pmatrix}_S . \tag{6.25}$$

The non-zero components of the matrix RM are

$$RM_{11} = 1, \quad RM_{12} = M_{12} + d_M, \quad RM_{16} = -R_{16}, \quad RM_{22} = 1, \tag{6.26}$$

$$RM_{33} = \cos 2\theta - \frac{d_1}{2\rho}\sin 2\theta + \frac{d_M}{\rho^2}(d_1 \sin^2\theta - \rho \sin 2\theta), \tag{6.27}$$

$$RM_{34} = M_{34} + d_M M_{33}, \tag{6.28}$$

$$RM_{43} = M_{43}, \quad RM_{44} = \cos 2\theta + \frac{1}{2\rho^2}[d_1 d_2 \sin^2\theta - (d_1 + d_2)\rho \sin 2\theta], \tag{6.29}$$

$$RM_{52} = -M_{52}, \quad RM_{55} = 1, \quad RM_{56} = M_{56} + \frac{d_M}{\gamma^2}, \quad RM_{66} = 1, \tag{6.30}$$

where k_S is the inverse focal length of the skew quadrupole, d_M is the distance from the end of the chicane to the monitor, and the matrix elements M_{ij} are those in Eq. (4.23)-Eq. (4.30). The vertical position y_M at the monitor after the chicane is

$$\begin{aligned} y_M &= -k_S RM_{34} x_s + RM_{33} y_s + RM_{34} y'_s = y_{2,k_S=0} - k_S RM_{34} x_s. \\ y_{2,k_S=0} &= RM_{33} y_s + RM_{34} y'_s. \end{aligned} \tag{6.31}$$

Taking the effect of the slit-mask into account, the average vertical spacing is

$$\begin{aligned} \langle \Delta y \rangle &= \langle (y^i_{M_{k_S=0}} - y^{i-1}_{M_{k_S=0}}) - k_S RM_{34}(x^i_s - x^{i-1}_s) \rangle \\ &\Rightarrow |\langle \Delta y \rangle| = |k_S| D \; RM_{34}, \end{aligned} \tag{6.32}$$

where D is the horizontal spacing of the slits and we used $\langle (y^i_{M,k_S=0} - y^{i-1}_{M,k_S=0}) \rangle = 0$. The vertical average spacing is proportional to the strength of the skew quadrupole, increases with the distance d_M to the monitor but is independent of the chirp. The electron beam should be focused vertically at the monitor to observe clearly separated slit images because the separation, determined by the second term in Eq. (6.31), should be larger than the first term of this equation which is determined by the betatron beam size.

The slope of the vertical separation with skew quadrupole strength can be used to infer the longitudinal separation that would be produced in the absence of this quadrupole

via

$$|\langle \Delta z \rangle| = \left[\frac{|1 + hMC_{56}|}{|h\eta|} \right] \left(\frac{|\langle \Delta y \rangle|}{|k_S| RM_{34}} \right), \tag{6.33}$$

where the terms in square brackets depend on the energy chirp and the chicane while those in parentheses depend on the observations at the transverse screen monitor.

6.3 Beam optics for the micro-bunched beam production

In this section, we show the beam optics to produce a micro-bunched beam. The beam optics and particle tracking from the entrance of CC1 to the beam dump were simulated using "ELEGANT" [74]. As initial parameters before CC1, we used the beam parameters shown in Table 3.1 while the initial Twiss functions were $\beta_x = \beta_y = 4.89$ m, and $\alpha_x = \alpha_y = 0$. These beta functions are chosen so that the electron beam sizes at the entrance of CC1 are 1 mm in each plane. The electron beam is assumed to be Gaussian distribution in transverse and longitudinal directions. The accelerating voltages in CC1 and CC2 are tuned so that the electron beam energy stays constant at ∼35 MeV.

Clear separations of the micro-bunches after the chicane require the total width of a micro-bunch to be smaller than the micro-bunch spacing $\langle \Delta z \rangle$. We set $8\sigma_{z,MB} \sim \langle \Delta z \rangle$ by controlling β_x at the slit-mask. Figure 6.3 shows the relation between total widths ($8\sigma_z$) of micro-bunched beams and betatron beam size $\sqrt{\epsilon_x \beta_{x,S}}$ for different energy chirps calculated with Eq. (6.22) and (6.23). Here, MC_{56}=-0.18 m, η=0.32 m, and normalized emittance ϵ_x=2 μm were used. Dots and lines represent widths and spacings of micro-bunched beams, respectively. From Fig. 6.3, we chose $\beta_{x,S} = 0.5$ m at the slits so that the betatron beam size $\sqrt{\epsilon_x \beta_{x,S}} = 0.12$ mm at the intersection of $8\sigma_z$ and $\langle \Delta z \rangle$ for energy chirps except for those close to $h = +5.6$ m^{-1} at the maximum compression where $\langle \Delta z \rangle = 0$. When the energy chirps are $h = +7, +9\,\mathrm{m}^{-1}$, $\langle \Delta z \rangle$ is still quite small. Therefore, correspondingly small values of $\epsilon_x \beta_x$ and uncorrelated energy spread $\sigma_{\delta,U}$ are required to obtain a clearly separated longitudinal distribution after the chicane.

Figure 6.4 shows the beam optics from CC1 to the beam dump at $h = -7$ m^{-1} with a chirp only in CC1. The beam optics for different energy chirps shows similar behavior. The horizontal beta function for all cases is focused to about 0.5 m at the slit-mask. We also focused the vertical beam size at the screen monitor X120 downstream of the chicane to be as small as possible for clear separations of the vertical slit images when the skew quadrupole is turned on.

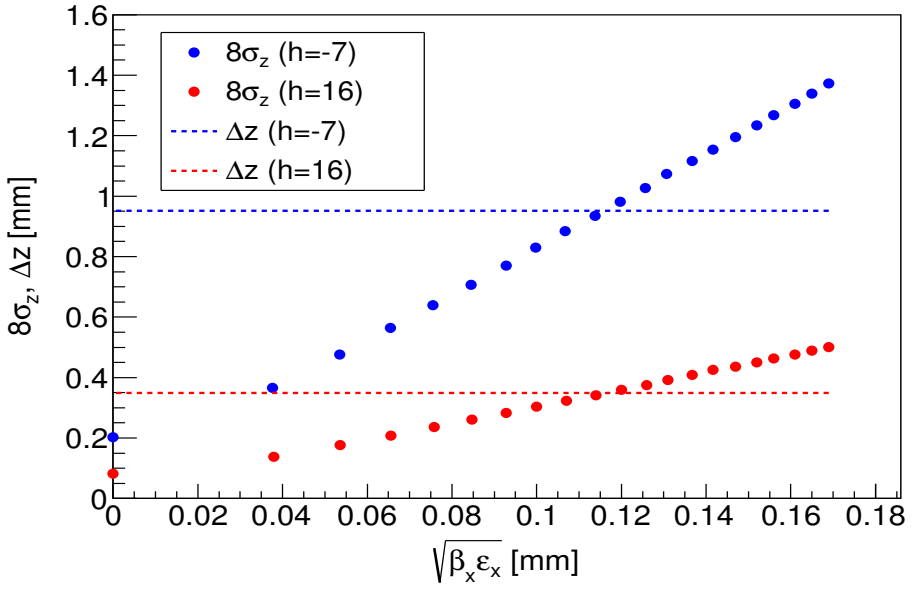

FIGURE 6.3: Spacing ($8\sigma_z$) and width (Δz) of micro-bunched beams as a function of $\sqrt{\beta_x \epsilon_x}$ at the slit-mask for different energy chirps. Dots and lines represent width and spacing of micro-bunched beams, respectively.

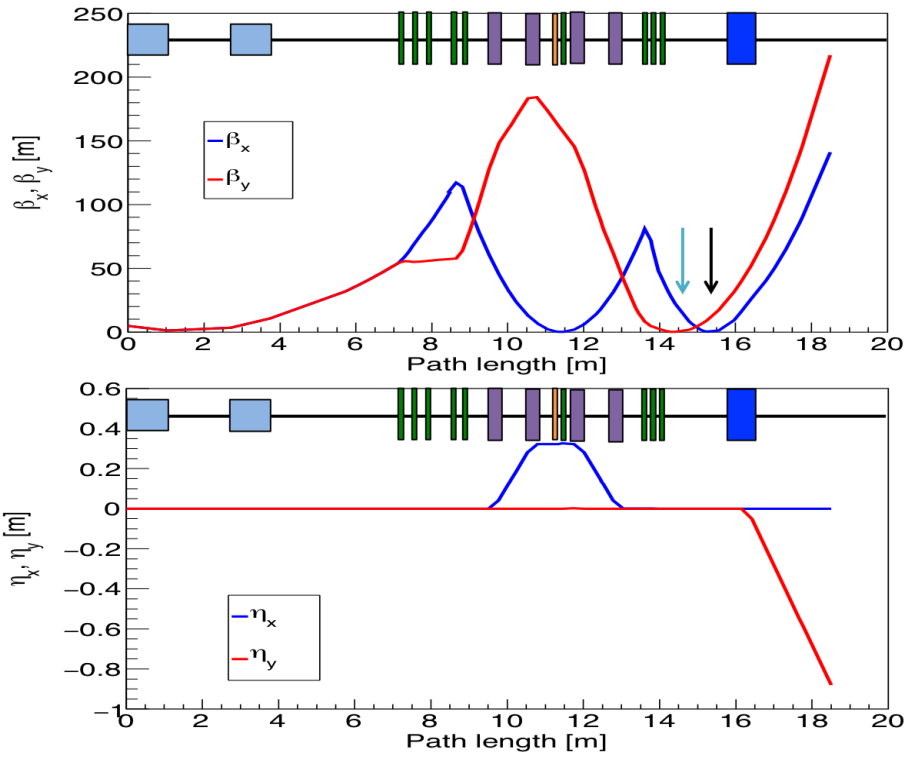

FIGURE 6.4: Beta and dispersion functions at $h = -7$ m^{-1} for CC1 chirp. Blue and red lines show horizontal and vertical planes respectively. Light blue, green, magenta boxes show the accelerating structures, (normal and skew) quadrupole magnets, and dipole magnet of the chicane, respectively. An orange and a blue boxes show the slit-mask and the vertical dipole magnet, respectively. The light blue and the black arrows represent the screen monitors at X120 and X121, respectively.

6.4 Simulations of micro-bunched beam production with ELEGANT

We performed particle tracking with ELEGANT including effects of the slit-mask, magnet nonlinearities, longitudinal space charge effects, and coherent synchrotron radiation (CSR) in the chicane. First, we simulated the longitudinal phase space and bunching factor without the slit-mask at X121 at the maximum compression (h∼5.6 m^{-1}), and the results are shown in Figure 6.5. The bunching factor is calculated with $B(\omega) = \frac{1}{N}\sqrt{(\sum_{i=1}^{N}\cos\omega t_i)^2 + (\sum_{i=1}^{N}\sin\omega t_i)^2}$ [74]. The bunch length of 1 mm is longitudinally compressed to 0.11 mm (0.36 ps) after passing through the chicane. Figure 6.6 and 6.7 show the longitudinal phase spaces and the longitudinal distributions at $h = \pm 7\,\mathrm{m}^{-1}$ (CC1 chirp), $h = \pm 9\,\mathrm{m}^{-1}$ (CC2 chirp), and $h = \pm 16\,\mathrm{m}^{-1}$ (CC1&2 chirps) at X121. Table 6.3 shows the width, micro-bunch spacing, and fundamental frequency obtained both by particle tracking and analytical calculations with Eq. (6.21), (6.22), and (6.23). The longitudinal distributions at h =-7, -9, and $\pm 16\,\mathrm{m}^{-1}$ are separated clearly but not at h =7 and 9 m^{-1}. Moreover, the spacing and width of micro-bunches at h =-7, -9, and $\pm 16\,\mathrm{m}^{-1}$ obtained by particle tracking agree with those computed with Eq. (6.21) and (6.22). For the two cases of h =7 and 9 m^{-1} (over-compressed modes), the overlaps between micro-bunches are caused by the small separation $\langle \Delta z \rangle$. Then, the width of micro-bunches is difficult to estimate from particle tracking correctly due to the large overlap.

Figure 6.8 shows the bunching factors obtained from FFTs of the longitudinal distributions for different energy chirps: h=±7, ±9, and ±16 m^{-1}. At h =-7, -9, and ±16 m^{-1}, narrow band frequency spectra are obtained due to well separated micro-bunches (see Fig. 6.7). We show the fundamental frequencies obtained by particle tracking and analytical calculations in Figure 6.9. The fundamental frequencies at the first peak obtained by particle tracking including longitudinal space charge effects are consistent with the results from Eq. (6.23). On the other hand, at h =7 and 9 m^{-1} where the micro-bunches overlap, the two frequency spectra have broad peaks, and there are differences in the fundamental frequencies between the simulations and the analytical results. The maximum frequencies, defined by the last clearly visible peak, are about 1.2 THz, 1.7 THz, and 2.2 THz at h =-7, -9, and -16 m^{-1}, respectively, and 3.2 THz, 3.7 THz, and 4.6 THz at h =7, 9, and 16 m^{-1}, respectively. Of course, the observed CTR spectra will be different from those shown in Fig. 6.8 with suppression at low frequencies from the finite size of the target, and at high frequencies due to the vacuum windows and the observed spectra will also depend on the detector's bandwidth.

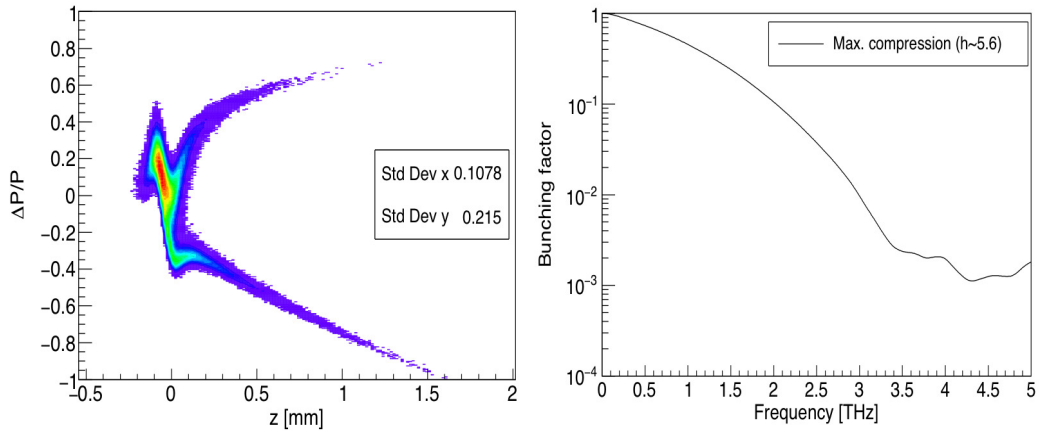

FIGURE 6.5: Longitudinal phase space and bunching factor at X121 at the maximum compression (h∼5.6 m^{-1}).

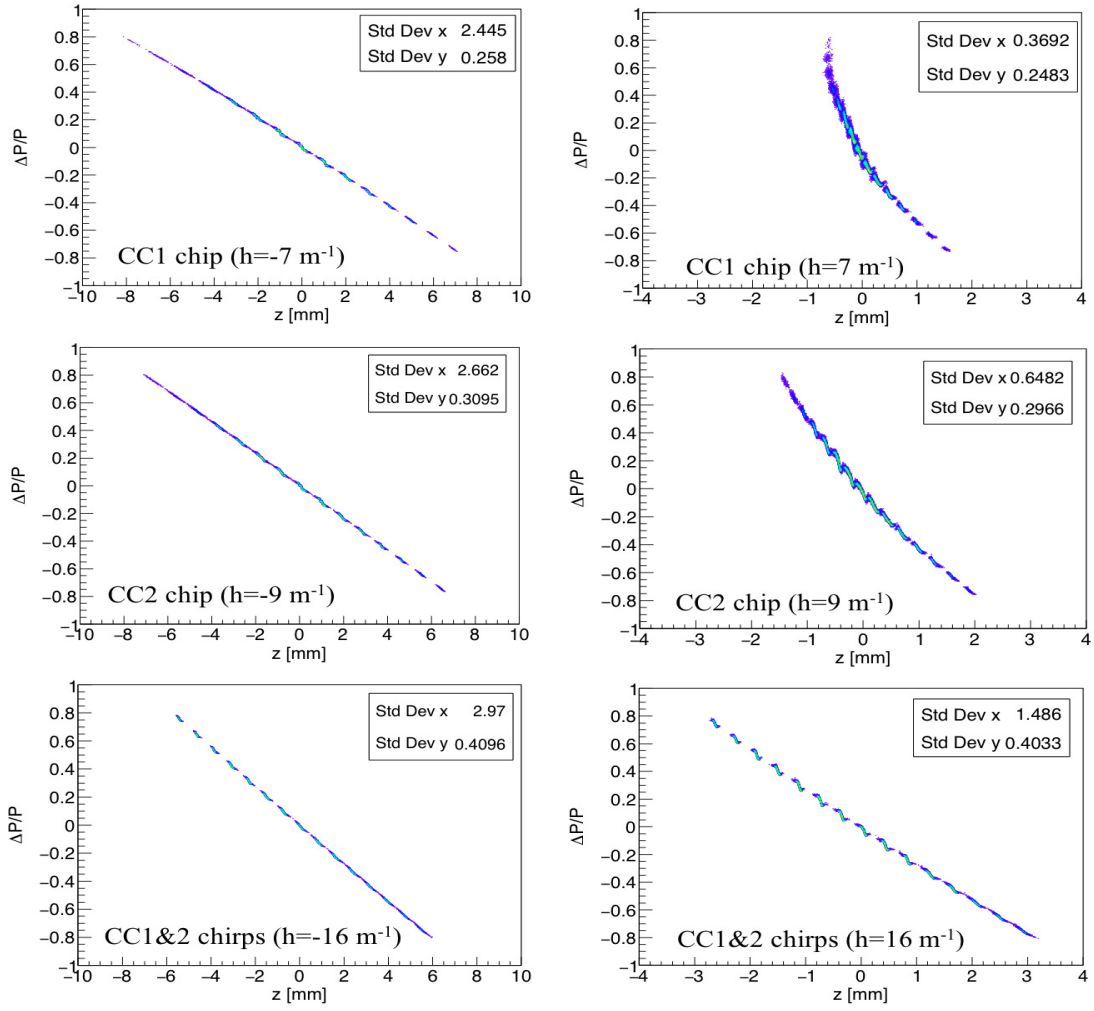

FIGURE 6.6: Longitudinal phase spaces for each energy chirp at X121. Left and right plots represent the bunch lengthening and shortening modes, respectively.

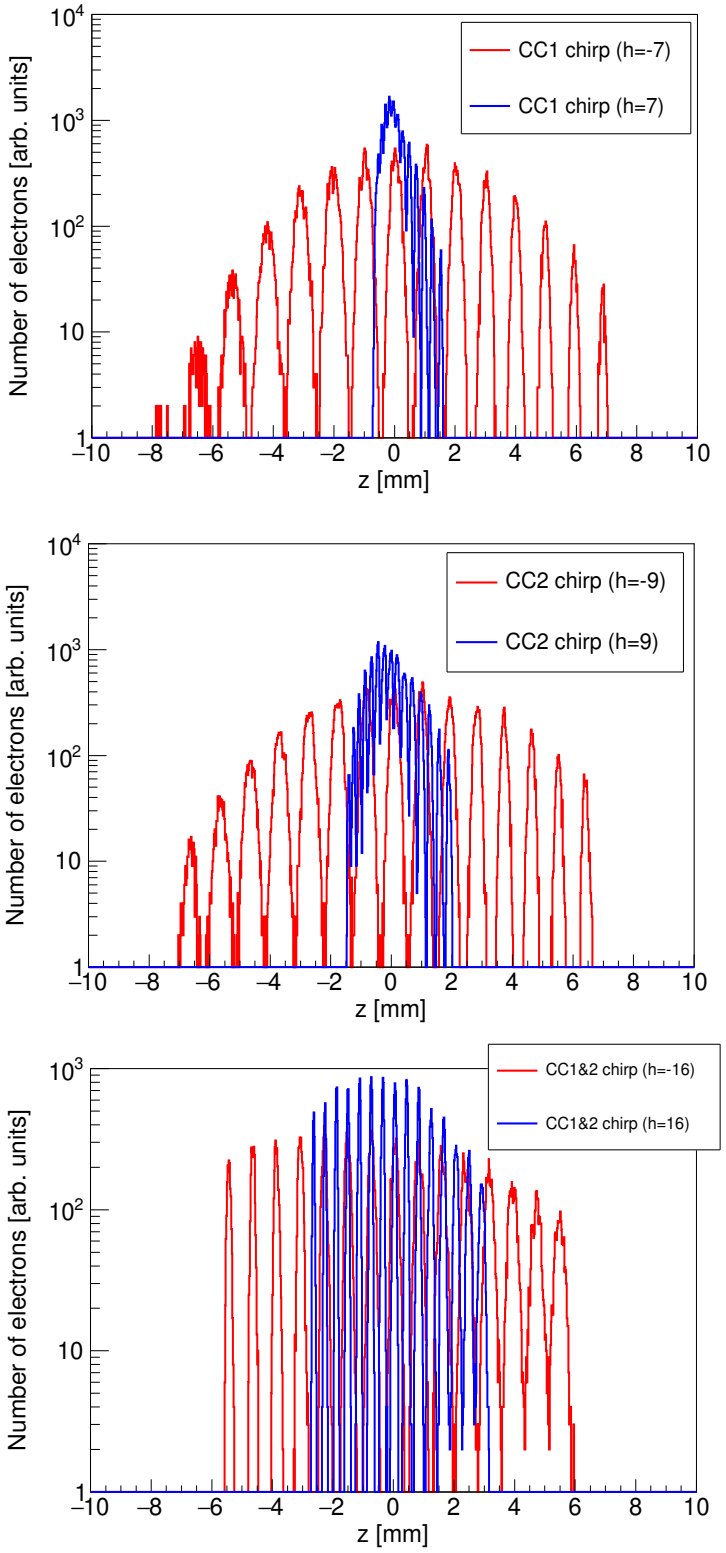

FIGURE 6.7: Longitudinal distributions at CC1 chip ($h = \pm 7\,\mathrm{m}^{-1}$), CC2 chirp ($h = \pm 9\,\mathrm{m}^{-1}$), and CC1&CC2 chips ($h = \pm 16\,\mathrm{m}^{-1}$). Red lines are the bunch lengthening mode, and blue lines are the over compressed mode.

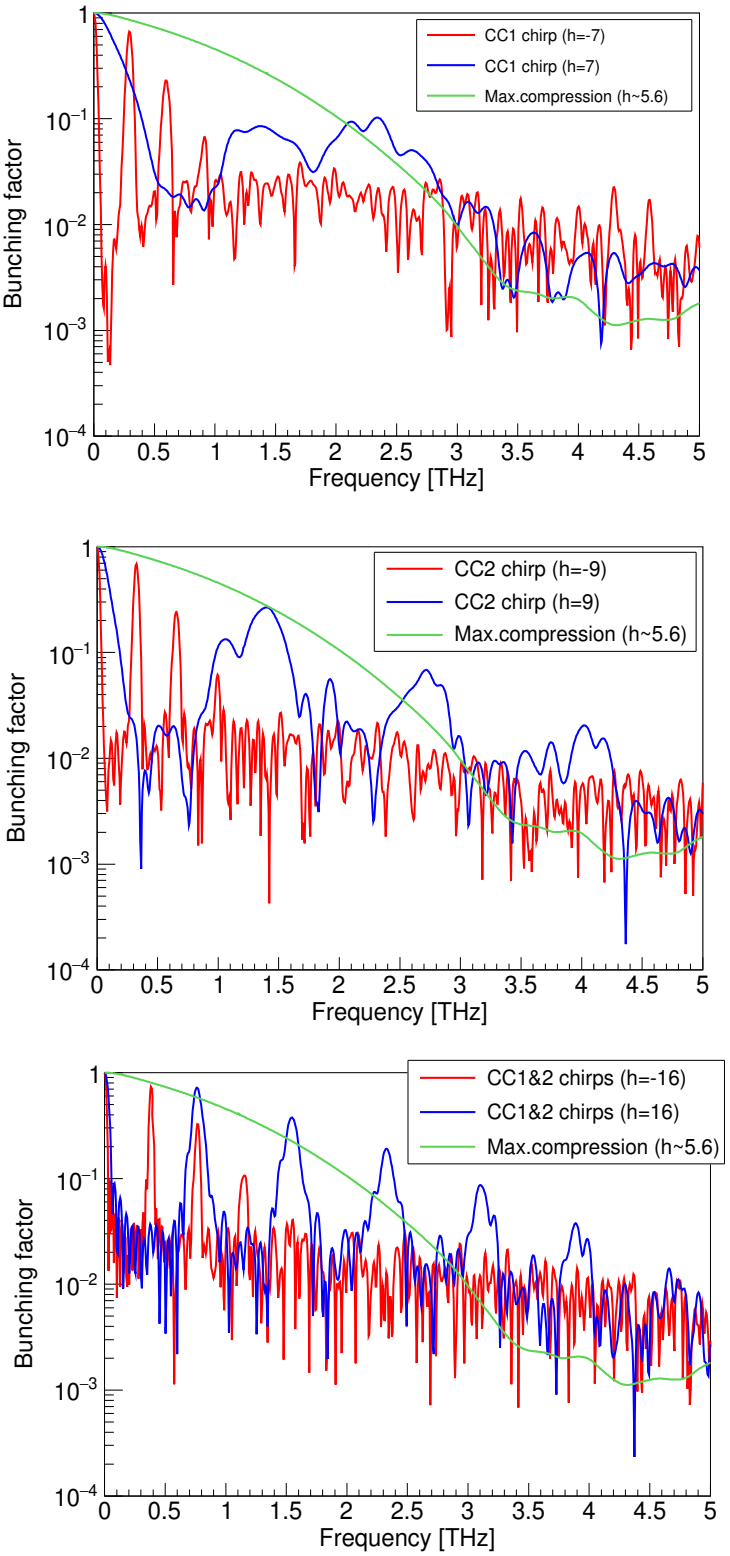

FIGURE 6.8: Frequency spectra for CC1 chip ($h = \pm 7\,\mathrm{m}^{-1}$), CC2 chirp ($h = \pm 9\,\mathrm{m}^{-1}$), CC1&CC2 chips ($h = \pm 16\,\mathrm{m}^{-1}$), and the longitudinal maximum compression ($h \sim 5.6\,\mathrm{m}^{-1}$). Red lines are the lengthening mode, blue lines are the over-compressed mode, and green lines are the max-compressed mode.

TABLE 6.3: Micro-bunch widths, spacing, and fundamental frequencies for each energy chirp. $\phi_{i,rf} = 0°$ implies on-crest RF phase. Values in parentheses show the results with longitudinal space charge (LSC), and calculated analytically with Eq. (6.21), (6.23), and (6.24), respectively. The initial bunch charge was 200 pC.

RF phase	Energy chirp	Width	Spacing	Fundamental freq.
$\phi_{1,rf}$, $\phi_{2,rf}$ [deg.]	[m^{-1}]	[mm]	[mm]	[THz]
(+35 , +35)	-16	(0.09, 0.09)	(0.78, 0.72)	(0.39, 0.42)
(0 , +35)	-9	(0.12, 0.11)	(0.92, 0.87)	(0.33, 0.35)
(+35 , 0)	-7	(0.13, 0.12)	(1.01, 0.95)	(0.30, 0.32)
(-35 , 0)	7	(0.04, 0.02)	(0.13, 0.11)	(2.33, 2.73)
(0 , -35)	9	(0.06, 0.03)	(0.22, 0.19)	(1.37, 1.54)
(-35 , -35)	16	(0.04, 0.04)	(0.39, 0.34)	(0.76, 0.87)

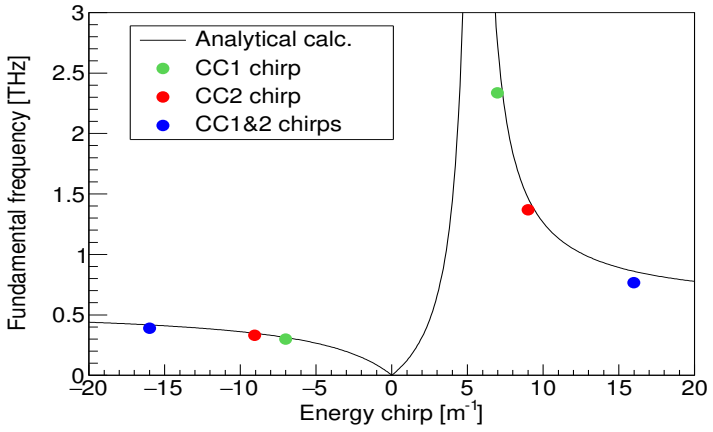

FIGURE 6.9: Fundamental frequency as a function of energy chirp.

6.5 Simulations of micro-bunched beam observation with ELEGANT

As discussed in Section 6.2.2, a skew quadrupole in the chicane generates vertical dispersion given by $\eta_y = -k_S R M_{34} \eta_x$ where η_x is the horizontal dispersion at the skew quadrupole. As a result, the micro-bunches are vertically separated after the chicane. Figure 6.10 shows the transverse distributions for k_S=-0.65 m^{-1} at X120 (left) and X121 (right) for h=-7m^{-1}. The distribution is tilted to the right to the beam coupling. The transverse distributions are similar, and the vertical spacings are the same for other chirp values, as predicted by Eq. (6.32). Figure 6.11 shows the vertical spacing of the electron beam depending on the strength of the skew quadrupole from particle tracking and from Eq. (6.32). The vertical spacing computed with Eq. (6.32) is consistent with that

from particle tracking. Also, the vertical spacing is proportional to the skew quadrupole strength as shown by this equation.

The micro-bunched beam at X121 in Fig. 6.10 is not symmetric with respect to $y = 0$ plane and has the different horizontal beam sizes in -y and +y directions. This means that the horizontal focusing strength is different in the bunch head and tail. The beam optics has the smallest horizontal beta function and a small vertical beta function at X121 by coincidence due to the vertical beam focus at X120, therefore, the electron beam is affected by the chromatic aberration. Since an electron beam with an energy chirp has a larger (and correlated) energy spread compared with a non-chirped beam, the chirped beam is sensitive to the chromatic aberration.

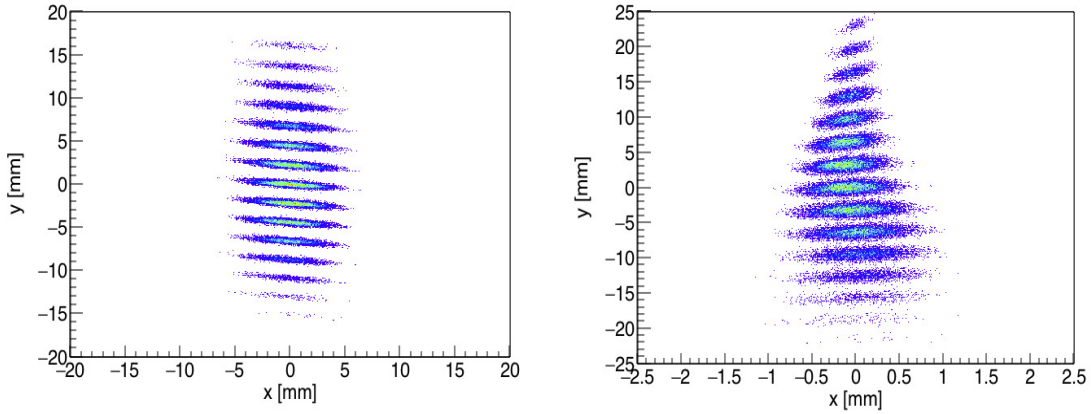

FIGURE 6.10: The transverse distributions at h=-7 m^{-1} at $X120$ and $X121$ when the K_S-value of the skew quadrupole is set equal to -5 m^{-2}. $K_S = k_S/L_Q$ where $L_Q = 0.13$ m is the length of the skew quadrupole.

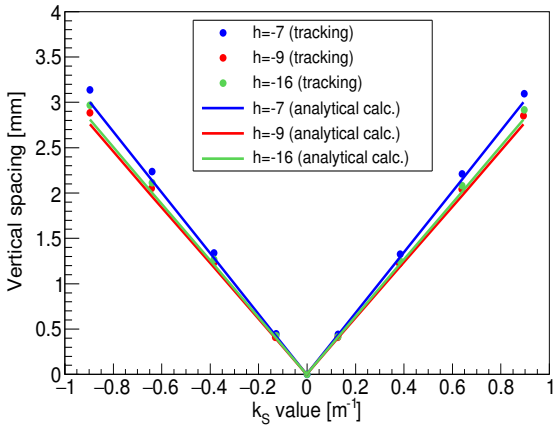

FIGURE 6.11: Vertical spacing as a function of K_S-values of the skew quadrupole. Dots and lines represent the results obtained by particle tracking and analytical calculation, respectively.

6.6 Simulations of micro-bunched beam production with flat beams

In Sec. 6.2, we showed that $\sqrt{\varepsilon_x \beta_x}$ at the slit-mask should be minimized to create a clearly separated micro-bunched beam longitudinally. Here, we consider that the use of flat beams ($\varepsilon_x \ll \varepsilon_y$) [75, 76] and perform simulations to create flat beams with energy chirps. Also, we simulate bunching factors of the micro-bunched beams of flat beams after the chicane with ASTRA and ELEGANT.

6.6.1 Canonical angular momentum beam

When an axial magnetic field on a photocathode is $B_z(z) \neq 0$, an electron beam produced at the photocathode has angular momentum and is said to be magnetized [37]. A beam envelope equation including space charge, beam emittance, and the angular momentum is given by [37]

$$\sigma'' - \frac{K}{4\sigma} - \frac{\varepsilon_u^2}{\sigma^3} - \frac{\mathcal{L}^2}{\sigma^3} = 0, \tag{6.34}$$

where K in the second term which represents the space charge effect is the perveance defined as $K = 2I/I_0\gamma^3$, where I is the absolute instantaneous beam current and I_0 is the Alfven current for electrons (∼17 kA), ε_u is the beam emittance, $\mathcal{L} = \langle L \rangle / 2p_z$, where p_z and $\langle L \rangle$ are the longitudinal momentum and the canonical angular momentum (CAM), respectively. The fourth term in Eq. (6.34) shows the canonical angular momentum and has the same effect as the beam emittance. Therefore, to generate a minimized emittance, the canonical angular momentum $\langle L \rangle$ needs to be zero or the fourth term should be smaller than the second and third terms.

A CAM dominated beam, means that the fourth term in Eq. (6.34) larger than the other terms, can be generated by immersing a photocathode in an axial magnetic field $B_z(z = 0)$. Then the average CAM $\langle L \rangle$ can be written as

$$\langle L \rangle = eB_z\sigma_c^2, \tag{6.35}$$

where σ_c is the rms beam size on the photocathode and B_z means $B_z(z = 0)$. An electron beam with a large average CAM requires a large magnetic field on the photocathode. As mentioned in Sec. 3.1, the bucking solenoid and main solenoid coils are installed in the FAST photoinjector, and $B_z(z = 0)$>0.2 T can be achieved on the cathode by a combination of the two solenoid coils.

6.6.2 Flat beam

An electron beam passing through a solenoid coil with $B_z(z=0) \gg 0$ has angular momentum, and then the 4×4 beam matrix Σ_0 and the four-dimensional beam emittance ε_m are given by [77]

$$\Sigma_0 \sim \begin{pmatrix} \langle x_0^2 \rangle & \langle x_0 x_0' \rangle & 0 & \mathcal{L} \\ \langle x_0 x_0' \rangle & \langle x_0'^2 \rangle & -\mathcal{L} & 0 \\ 0 & -\mathcal{L} & \langle x_0^2 \rangle & \langle x_0 x_0' \rangle \\ \mathcal{L} & 0 & \langle x_0 x_0' \rangle & \langle x_0'^2 \rangle \end{pmatrix}, \tag{6.36}$$

$$\begin{aligned} \varepsilon_m = \sqrt{|\Sigma_0|} &= \left(\langle x_0^2 \rangle \langle x_0'^2 \rangle - \langle x_0 x_0' \rangle^2\right) - \mathcal{L}^2 \\ &= \varepsilon_1^2 - \mathcal{L}^2, \end{aligned} \tag{6.37}$$

where ε_1 is the projected emittance, and $\langle xy \rangle$=0 and a round beam are assumed. Here, we consider a transport line with a transfer matrix M to remove the CAM from the electron beam. The beam matrix Σ_1 after the transport line is obtained from $\Sigma_1 = M\Sigma_0 M^T$. When the appropriate transfer matrix M is chosen to remove the CAM, the 4×4 sigma matrix Σ_1 and the four-dimensional emittance ε_f become [77]

$$\Sigma_1 \sim \begin{pmatrix} \langle x_1^2 \rangle & \langle x_1 x_1' \rangle & 0 & 0 \\ \langle x_1 x_1' \rangle & \langle x_1'^2 \rangle & 0 & 0 \\ 0 & 0 & \langle y_1^2 \rangle & \langle y_1 y_1' \rangle \\ 0 & 0 & \langle y_1 y_1' \rangle & \langle y_1'^2 \rangle \end{pmatrix}, \tag{6.38}$$

$$\begin{aligned} \varepsilon_f = \sqrt{\Sigma_1} &= \left(\langle x_1^2 \rangle \langle x_1'^2 \rangle - \langle x_1 x_1' \rangle\right) \left(\langle y_1^2 \rangle \langle y_1'^2 \rangle - \langle y_1 y_1' \rangle\right) \\ &= \varepsilon_+ \varepsilon_-. \end{aligned} \tag{6.39}$$

This transport keeps the four dimensional emittances cosntant. Therefore, equating Eq. (6.37) and (6.39)

$$\varepsilon_+ \varepsilon_- = \varepsilon_1^2 - \mathcal{L}^2. \tag{6.40}$$

From [78], there is a relationship on the trace invariant $I(\Sigma_0) = -\frac{1}{2} Tr(J_4 \Sigma_0 J_4 \Sigma_0)$, where J_4 is the four-dimensional symplectic matrix. Thus, we have

$$\begin{aligned} Tr(J_4 \Sigma_0 J_4 \Sigma_0) &= Tr(J_4 \Sigma_1 J_4 \Sigma_1), \\ \Rightarrow \varepsilon_+^2 + \varepsilon_-^2 &= 2(\varepsilon_1^2 + \mathcal{L}^2). \end{aligned} \tag{6.41}$$

From Eq. (6.38) and (6.41), we have

$$\varepsilon_{\pm} = \varepsilon_1 \pm \mathcal{L}. \tag{6.42}$$

The two beam emittances ε_+, ε_- are obtained, and for $\mathcal{L}$=0, the two beam emittances are consistent with the projected emittance ε_1.

An electron beam emitted at a photocathode immersed in an axial magnetic field has angular momentum, and the 4×4 beam matrix Σ_0 on the photocathode is given by [77]

$$\Sigma_0 \sim \begin{pmatrix} \sigma_0^2 & 0 & 0 & \mathcal{L} \\ 0 & \sigma_0'^2 + k\mathcal{L} & -\mathcal{L} & 0 \\ 0 & -\mathcal{L} & \sigma_0^2 & 0 \\ \mathcal{L} & 0 & 0 & \sigma_0'^2 + k\mathcal{L} \end{pmatrix}, \tag{6.43}$$

where $k = eB_z/2p_z$ and we assume $\langle xy \rangle = \langle x'y \rangle = \langle xy' \rangle = \langle xx' \rangle = \langle y'y' \rangle = 0$. Then, the projected emittance ε_1 is

$$\varepsilon_1 = \sqrt{\sigma_0^2\sigma_0'^2 + \sigma_0^2 k\mathcal{L}} = \sqrt{\varepsilon_{th}^2 + \mathcal{L}^2}, \tag{6.44}$$

where $\varepsilon_{th} = \sigma_0\sigma_0'$ represents the beam emittance at the photocathode. Therefore, the two beam emittances from Eq. (6.42) are

$$\varepsilon_{\pm} = \sqrt{\varepsilon_{th}^2 + \mathcal{L}^2} \pm \mathcal{L}. \tag{6.45}$$

For a CAM dominated beam $\mathcal{L} \gg \varepsilon_u$,

$$\varepsilon_+ \simeq 2\mathcal{L}, \quad \varepsilon_- \simeq \frac{\varepsilon_u^2}{2\mathcal{L}}. \tag{6.46}$$

6.6.3 Removing an angular momentum

The generation of a flat beam requires the removal of the canonical angular momentum from an electron beam, and it is known that the CAM can be removed using skew quadrupole magnets [78, 79]. In the FAST beamline, three skew quadrupole magnets to convert a magnetized beam into a flat beam have been installed between CC2 and the chicane (see Fig. (3.2)), and we can produce a flat beam with them. The K-values of the

three skew quadruple magnets can be approximately calculated by [78, 79]

$$q_1 = \pm\sqrt{\frac{-d_2 s_{11} + s_{12} - d_2 d_T s_{21} + d_T s_{22}}{d_2 d_T s_{12}}} \tag{6.47}$$

$$q_2 = -\frac{s_{12} + d_T s_{22}}{d_2 d_3 (1 + q_1 s_{12})} \tag{6.48}$$

$$q_3 = -\frac{q_1 + q_2 + d_2 q_1 q_2 s_{11} + s_{21}}{1 + (d_T q_1 + d_3 q_2) s_{11} + d_2 d_3 q_2 (q_1 + s_{21})} \tag{6.49}$$

where d_2 and d_3 are the distances between the first and the second, the second and the third skew quadrupole magnets, respectively, $d_T = d_2 + d_3$, and s_{ij} shows each element of the 2×2 matrix s consisting of Twiss parameters at the first skew quadrupole magnet [78, 79],

$$s = \begin{pmatrix} \alpha & \beta \\ -\frac{1+\alpha^2}{\beta} & -\alpha \end{pmatrix}. \tag{6.50}$$

6.6.4 Generating flat beams

We performed simulations to generate a flat beam with ASTRA and ELEGANT from the photocathode to the beam dump. First we made a magnetized electron beam at the photocathode and did the particle tracking to the first skew quadrupole magnet for each energy chirp using ASTRA, then we created flat beams by removing the CAM from the magnetized beams using three skew quadrupole magnets with ELEGANT.

We set the axial magnetic field at the photocathode to $B_z(z = 0)$=0.113-0.118 T [51, 53] and the beam size at the photocathode to σ_c=0.1 mm. Then, the $\mathcal{L}$ at the entrance of the skew quadrupole magnet can be calculated as

$$\mathcal{L} = \frac{eB_0\sigma_c^2}{2p_z} = 3.73 \times 10^{-7}\,\mathrm{m}. \tag{6.51}$$

Using ELEGANT, we removed the CAM from the magnetized beam and created flat beams for h=-7, h=-10, and h=-17. The obtained emittances and ratios are $\varepsilon_+ = (2.4 - 2.9) \times 10^{-7}$ m, $\varepsilon_- = 4.5 \times 10^{-5}$ m, $\varepsilon_-/\varepsilon_+ = 181 - 155$, respectively, and are shown in Table 6.4. Moreover, K-values of three skew quadrupole magnets simulated with ELEGANT and calculated with Eq. (6.47)-(6.49) are summarized in Table 6.5. The K-values simulated by particle tracking are almost consistent with those calculated with the analytical equations.

TABLE 6.4: Normalized beam emittances and emittance ratios for h=-7, -10, -17 simulated with ASTRA and ELEGANT.

Energy chirp [m^{-1}]	Nor. emittance (ε_+, ε_-) [m·rad]	emittance ratio
-7	(2.4×10^{-7}, 4.5×10^{-5})	187
-10	(2.5×10^{-7}, 4.5×10^{-5})	181
-17	(2.9×10^{-7}, 4.5×10^{-5})	155

TABLE 6.5: K-values of skew quadrupole magnets (Q106, Q107, Q111) for h=-7, -10, -17 simulated with ELEGANT and calculated with Eq. (6.47-6.49). Values in parentheses show the K-values estimated with the analytical equations.

Energy chirp [m^{-1}]	Q106 [m^{-2}]	Q107 [m^{-2}]	Q111 [m^{-2}]
-7	16.1 (15.3)	-13.6 (-12.8)	2.4 (2.7)
-10	8.8 (8.7)	-7.1 (-6.8)	2.2 (2.2)
-17	16.8 (15.9)	-14.4 (-13.4)	2.6 (3.0)

We also estimated the two beam emittances (ε_+, ε_-) and the emittance ratio using Eq. (6.46) and obtained

$$\varepsilon_+ = 1.7 \times 10^{-7}\,\mathrm{m}, \quad \varepsilon_- = 4.5 \times 10^{-5}\,\mathrm{m}, \tag{6.52}$$

$$\frac{\varepsilon_-}{\varepsilon_+} \sim 239. \tag{6.53}$$

Here, we used the Kim's model [80] to compute the emittance ε_{th} [81, 82],

$$\begin{aligned}
\varepsilon_{th} &< \frac{1}{\beta\gamma}\sqrt{\varepsilon_{thermal}^2 + \varepsilon_{rf}^2 + \varepsilon_{space\,charge}^2} \sim 4.8 \times 10^{-8}\,\mathrm{m\cdot mrad}, \quad (6.54)\\
\varepsilon_{thermal} &= \sigma_c\sqrt{\frac{2E_{kin}}{3m_0c^2}} = 0.677\,\mathrm{mm\cdot mrad},\\
\varepsilon_{rf} &= \frac{\alpha k^3\sigma_x^2\sigma_z^2}{\sqrt{2}} \sim 0.01\,\mathrm{mm\cdot mrad},\\
\varepsilon_{space\,charge} &= \frac{\pi}{4\alpha k}\frac{I}{I_A}\frac{\sigma_z}{3\sigma_x + 5\sigma_z} \sim 2.8\,\mathrm{mm\cdot mrad}.
\end{aligned}$$

The emittance at the first skew quadrupole magnet obtained in ASTRA simulation is 5.0×10^{-8} m, which is a value close to ε_{th} in Eq. (6.54). However, the emittance (ε_+) simulated by particle tracking are 1.5 times larger than that estimated with the analytical equations. As the chromatic aberration is ignored in the calculation, the difference of values might come from the nonlinear effect of quadrupole magnets.

Figure 6.12 shows that the beam distributions after the last skew quadrupole magnet at energy chirps of h=-7, -10, -17 m^{-1} simulated with ASTRA and ELEGANT. The S-shaped transverse distributions, are seen at $h = -7$ m^{-1} (CC1 chirp) and -17 m^{-1} (CC1&2 chirps), are caused by nonlinear RF kicks from cavities [83]. Moreover, we simulated bunching factors for each energy chirp with the flat beams. Figure 6.13 shows

the bunching factors for round and flat beams. For flat beams, we can see peaks at more higher frequencies compared with those for round beams.

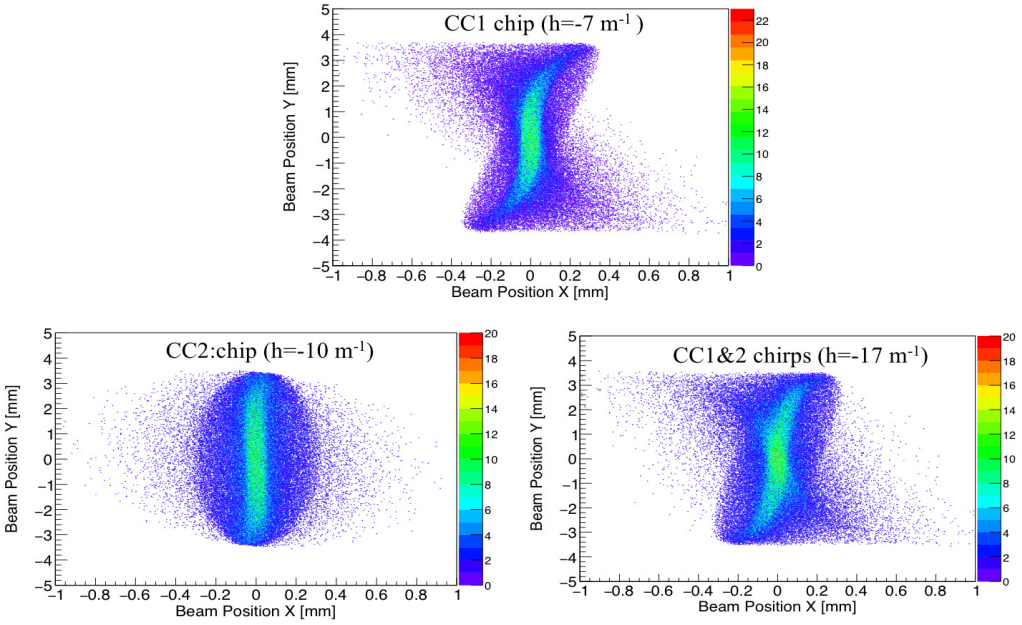

FIGURE 6.12: Beam distributions for each energy chip before the chicane.

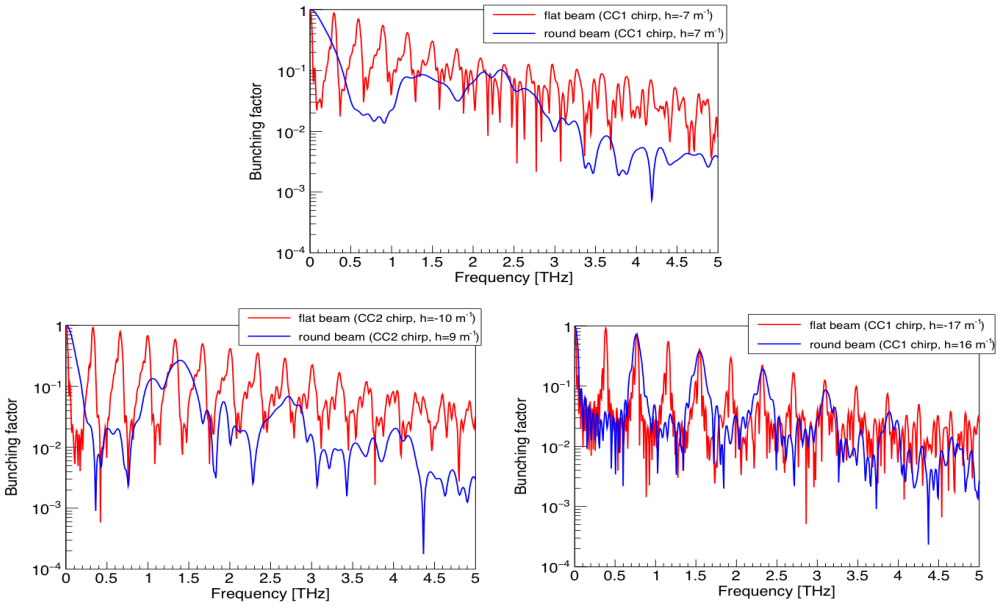

FIGURE 6.13: Bunching factors for each energy chirp after the chicane.

6.7 Generation of THz radiation

In general, two methods to generate THz radiation have been known: transition radiation (TR) with a thin metallic plate and synchrotron radiation with a dipole magnet. In this section, THz radiation production with TR and a wiggler consisting of a series of dipole magnets are described, and we also calculate the energy density [J/THz] of THz radiation generated from the micro-bunched beams with the two methods.

6.7.1 Transition radiation

When charged particles pass through the boundary of two media with different dielectric constants, transition radiation (TR) is emitted forward and backward directions with respect to the incident particles [84–86]. The schematic diagram of the transition radiation is shown in Figure 6.14. The transition radiation can be interpreted that it is emitted by an interaction between an electron and its image charge. We insert an Al foil tilted at 45 degrees at X121 and extract backward TR into a detector installed in the outside of the beamline. The spectral energy u of backward TR emitted by an electron per unit solid angle in SI units is

$$\frac{d^2u}{d\omega d\Omega} = \frac{e^2}{4\pi^3\epsilon_0 c}\frac{\beta^2\sin^2\theta}{(1-\beta^2\cos^2\theta)^2}, \tag{6.55}$$

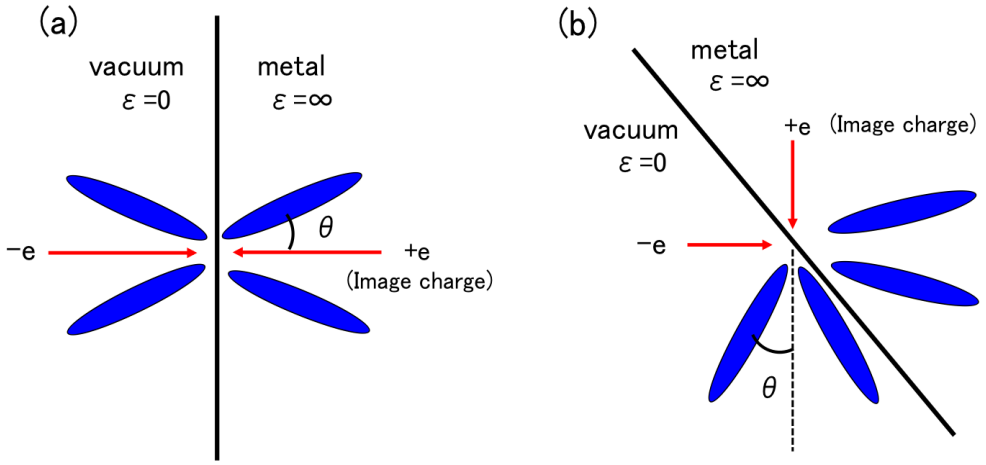

FIGURE 6.14: Sketch of the transition radiation. (a) and (b) represent normal incident and the oblique incident of 45 degrees.

where θ is the emission angle with respect to the incident electron beam and $\beta = v/c$. The spectral energy U for the number of electrons N is

$$\frac{d^2U}{d\omega d\Omega} = [N + N(N-1)F(\omega,\theta)]\,\frac{d^2u}{d\omega d\Omega}, \tag{6.56}$$

where $F(\omega,\theta)$ is a bunching factor depending on an electron distribution and is given by

$$F(\omega,\theta) = |f(\omega,\theta)|^2 = \left|\int\int\int f(r,z)exp(-i\boldsymbol{k}\cdot\boldsymbol{x})\right|^2 d^3x. \tag{6.57}$$

The three dimensional density distribution $f(r,z)$ of an electron bunch in Eq. (6.57) can be divided into longitudinal $h(z)$ and transverse $g(r)$ distributions of a bunch

$$f(r,z) = g(r)h(z). \tag{6.58}$$

Using the relation of $\boldsymbol{n}\cdot\boldsymbol{z} = z\cos\theta$ and $\boldsymbol{n}\cdot\boldsymbol{r} = r\sin\theta$, Eq. (6.57) becomes

$$\begin{aligned} F(\omega,\theta) &= \left|\int g e^{ikr\sin\theta}dr\int h e^{ikz\cos\theta}dz\right|^2 \\ &= \left|\int_0^{2\pi}\int_0^{\infty} g(\rho,\phi)e^{ik\rho\cos\phi\sin\theta}\rho d\rho d\phi\int_{-\infty}^{\infty} h(z)e^{ikz\cos\theta}dz\right|^2. \end{aligned} \tag{6.59}$$

We used $r = \rho\cos\phi$ in a cylindrical coordinate system. When an electron bunch is assumed to be a Gaussian distribution in transverse and longitudinal directions, g and h are

$$g(x,y) = \frac{1}{2\pi\sigma_\perp^2}e^{-(x^2+y^2)/2\sigma_\perp^2} \quad \Rightarrow \quad g(\omega) = e^{-(\omega\sigma_\perp\sin\theta/c)^2}, \tag{6.60}$$

$$h(z) = \frac{1}{\sqrt{2\pi}\sigma_z}e^{-z^2/2\sigma_z^2} \quad \Rightarrow \quad h(\omega) = e^{-(\omega\sigma_z/c)^2}, \tag{6.61}$$

where $\sigma_\perp$ and σ_z are transverse and longitudinal beam sizes. Therefore, the spectral energy U for the number of electrons N (Eq. (6.56)) can be written as

$$\frac{d^2U}{d\omega d\Omega} \simeq N^2 e^{-\left(\frac{\omega}{c}\right)^2\left(\sigma_\perp^2\sin^2\theta+\sigma_z^2\right)}\frac{d^2u}{d\omega d\Omega}. \tag{6.62}$$

Since peak widths of a micro-bunched beam are smaller than transverse beam sizes at a target foil, we have $\sigma_z \ll \sigma_\perp\sin\theta$. From Eq. (6.62), high intensity CTR requires small transverse beam sizes at the foil. As $e^{-1} \sim 0.37$, we would like to satisfied with

$$\left(\frac{\omega}{c}\right)^2\left(\sigma_\perp^2\sin^2\theta\right) \leq 1, \tag{6.63}$$

With $\sin\theta \simeq 1/\gamma$, $k = 2\pi/\lambda$, and $\omega = ck$, the critical frequency f_c which means a high frequency cut-off is

$$f_c = \frac{\gamma c}{2\pi\sigma_\perp}. \tag{6.64}$$

For an electron beam of ~35 MeV and the beam size of 1 mm at an Al foil, the high frequency cut-off is f_c~3.3 THz. On the other hand, when the longitudinal beam size is larger than the transverse beam sizes at the foil $\sigma_z \gg \sigma_\perp \sin\theta$, the critical frequency f_c is

$$f_c = \frac{c}{2\pi\sigma_z}. \tag{6.65}$$

The bunching factor is the indicator that TR is coherent for $F \to 1$ or incoherent for $F \to 0$. Therefore, when the bunching factor is close to one (coherent TR: CTR), the spectral energy emitted from the entire bunch is

$$\frac{d^2U}{d\omega d\Omega} \simeq N^2 F(\omega,\theta)\frac{d^2u}{d\omega d\Omega}. \tag{6.66}$$

Integrating Eq. (6.66) over the solid angle,

$$\frac{dU}{d\omega} \simeq N^2 \frac{e^2}{4\pi^3\epsilon_0 c}\left[\frac{1+\beta^2}{\beta}\ln\left(\frac{1+\beta}{1-\beta}\right) - 2\right] F(\omega,\theta). \tag{6.67}$$

Using the bunching factor shown in Fig. 6.8, the energy density in μJ/THz for two chirp settings using both CC1 and CC2 is shown in Figure 6.15. Here we assumed an initial bunch charge of 1 nC and 5% transmission, so that N=50 pC at the foil. The left plot in Fig. 6.15 shows that the energy density at the first harmonic with either chirp setting is about 0.15 μJ/THz. Three harmonics are visible up to ~3 THz for both settings, but the energy density falls more slowly with frequency for the compression setting (h=+16), as expected. The peaks in the spectrum are at (0.39, 0.75, 1.14) THz with bunch lengthening and at (0.75, 1.53, 2.14) THz with bunch compression. Since the coherent radiation energy scales with the square of the bunch charge and linearly with the bunching factor, it may be possible to increase the radiated energy from the above estimates by increasing the slit width for greater transmission which will also increase the overlap between the micro-bunches and reduce the bunching factor.

6.7.2 Energy density enhanced with a small wiggler

Instead of CTR, it is conceivable to use a wiggler [87, 88] as a broad-band source of radiation which has the advantage of higher photon flux but requires more space in the beamline. Here we provide an estimate of the energy density expected from a wiggler and compare it with the energy density from CTR. A wiggler can be considered as a

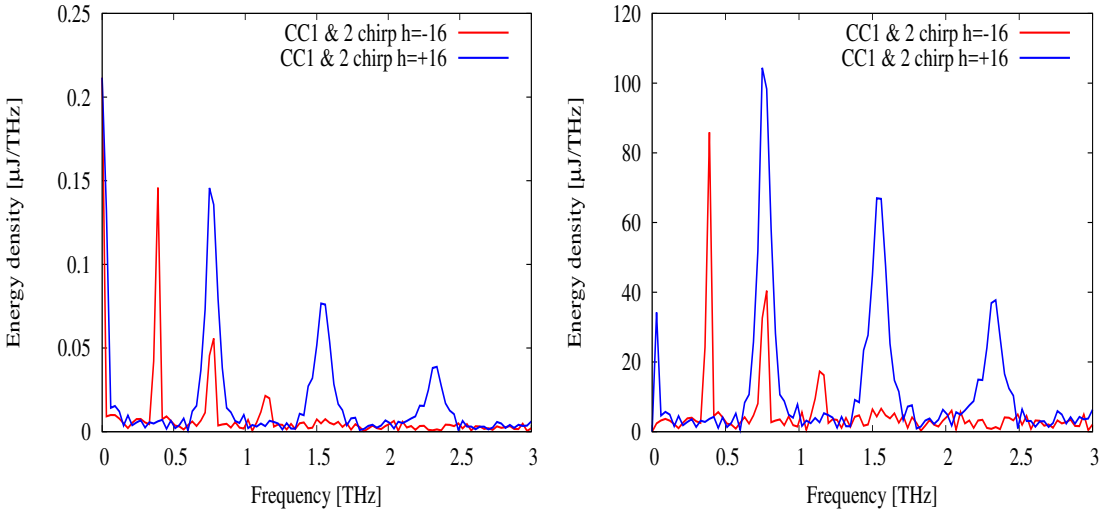

FIGURE 6.15: Energy density spectrum from two radiation sources with two chirp settings using CC1 and CC2. Charge per bunch at the radiator is 50 pC. Left: From CTR, Right: From a wiggler, $K = 2.8$, length = 1.5 m.

series of bending magnets. The photon flux emitted from a wiggler is the summation of the flux from each bending magnet. The energy spectrum u per frequency ω by one electron radiated from a bending magnet is [87, 88]

$$\left(\frac{du}{d\omega}\right)_{bend} = \frac{\sqrt{3}}{2}\alpha\gamma\hbar\left(\frac{\omega}{\omega_c}\right)\int_{\omega/\omega_0}^{\infty} K_{5/3}(u)du, \tag{6.68}$$

$$\omega_c = \frac{3}{2}\frac{\gamma^3 c}{\rho}, \tag{6.69}$$

where α is the fine structure constant, $\hbar$ is Planck's constant, $K_{5/3}$ is a Bessel function, ω_c is the critical frequency, and ρ is the bending radius of the dipole magnet. Therefore, for a wiggler with a series of N_p bending magnets (number of periods=$N_p/2$), the energy spectrum per one electron is given by

$$\left(\frac{du}{d\omega}\right)_{wiggler} \simeq N_p\left(\frac{du}{d\omega}\right)_{bend} = \frac{\sqrt{3}}{2}N_p\alpha\gamma\hbar\left(\frac{\omega}{\omega_c}\right)\int_{\omega/\omega_0}^{\infty} K_{5/3}(u)du. \tag{6.70}$$

Using Eq. (6.66), the coherent energy spectrum U generated from N electrons is

$$\begin{aligned}\left(\frac{dU}{d\omega}\right)_{wiggler} &\simeq N^2F(\omega,\,\theta)\left(\frac{du}{d\omega}\right)_{wiggler} \\ &= \frac{\sqrt{3}}{2}N_pN^2\alpha\gamma\hbar F(\omega,\,\theta)\left(\frac{\omega}{\omega_c}\right)\int_{\omega/\omega_0}^{\infty} K_{5/3}(u)du.\end{aligned} \tag{6.71}$$

If λ_W is the length of the wiggler period, then the parameter defining the wiggler strength is $K = 0.934\lambda_W[\mathrm{cm}]B_0[\mathrm{T}]$, where B_0 is the bending field [89]. Typically $K > 2.5$ describes the transition from a multiple harmonics undulator radiation to the broadband

wiggler radiation. For significant THz radiation, we require a low critical frequency ω_c, and a compact wiggler requires small values of λ_W, N_P. Choosing for an example calculation, $B_0 = 0.2$ T yields the critical frequency $f_c = 40.5$ kHz at the FAST energy and with $\lambda_W = 15$ cm, $K = 2.8$, and $N_P = 10$ results in a wiggler length of 1.5 m. The right plot in Fig. 6.15 shows the energy density spectrum using Eq. (6.71) and the bunching factor calculated above (see Fig. 6.8).

The energy density with the wiggler at the first harmonic reaches (86, 104) μJ/THz for $h = (-16, 16)$ respectively, nearly three orders of magnitude higher than from CTR. However, since the angular spread of wiggler radiation is larger ($\sim K/\gamma$) than that of CTR ($\sim 1/\gamma$), the energy deposited from a wiggler can be expected to be about two orders of magnitude larger.

6.8 Detection of THz radiation

As mentioned in Sec. 6.7, we generate CTR by sending electron beams to an Al foil installed in the beamline and transport it to an interferometer. In the FAST facility, a Martin Puplett interferometer (MPI) and pyroelectric detectors are placed near the vertical dipole magnet, which is used to measure bunch lengths of a longitudinally compressed beam. We tried to measure the THz radiation in experiments using them. Also, we are preparing a Michelson interferometer (MI) and a bolometer for the upcoming experiments. In this section, Michelson and Martin-Puplett interferometers and THz detectors which we use to measure frequency spectra are described.

6.8.1 Michelson and Martin Puplett interferometers

A Michelson interferometer (MI) consists of a beam splitter, a fixed flat mirror, a movable flat mirror, and a detector. Figure 6.16 shows a simplified diagram of a MI. An incident light beam is split into two beams by a beam splitter which has transmittance 50% and reflectance 50%, and then the two beams are sent to the fixed mirror and the movable mirror. The beams are recombined at the beam splitter after traveling the different routes. The intensity of the recombined light at the detector depends on the difference of path length from the beam splitter to each mirror.

When the two path lengths from the beam splitter to the mirrors L_1 and L_2 are equal or differ by a multiple of half the wavelength of light, the path length difference x between the recombined beams at the detector is zero. The intensity can be written as

$$I_{obs}(x) = \int_0^\infty 2R_0T_0I_0\left(1 + \cos(2\pi kx)\right) dk, \tag{6.72}$$

where I_0 is the intensity of the incident beam, R_0 and T_0 are reflection and transmission coefficients of the beam splitter, respectively. $I(x)$ is called the interferogram. Here, we assume that the transmission : reflection = 50% : 50%. Then,

$$I_{obs}(x) = \int_0^\infty \frac{I_0}{2}\left(1 + \cos(2\pi kx)\right) dk. \tag{6.73}$$

The change of the intensity at the detector is a contribution from the second therm I_{ac} of Eq. (6.73)

$$\begin{aligned} I_{ac} &= \int_0^\infty \frac{I_0(k)}{2}\cos(2\pi kx)dk. \\ &= \frac{1}{2}\int_0^\infty I_0(k)\frac{e^{ikx}+e^{-ikx}}{2}dk \\ &= \frac{1}{2}\int_{-\infty}^\infty I_0(k)e^{ikx}dk. \end{aligned} \tag{6.74}$$

Therefore, the incident light $I_0(k)$ can be computed from the interferogram Eq. (6.74) by the inverse Fourier transformation,

$$I_0(k) = 2\int_{-\infty}^\infty I_{ac}(x)e^{-2\pi kx}dx = 2\int_{-\infty}^\infty \left[I_{obs}(x) - I_{dc}(x)\right]e^{-2\pi kx}dx. \tag{6.75}$$

A Martin-Puplett interferometer (MPI) [90, 91] basically consists of two polarizers and a wire grid polarizer, and two rooftop mirrors. The schematic of a MPI, is similar to that of a MI, is shown in Figure 6.17. An incident beam of light is horizontally polarized by a polarizer, and it is then sent to a beamsplitter of a wire grid polarizer. The beamsplitter divides the incoming beam into two beams with the same intensities and polarizations perpendicular to each other. Each split beam of light is reflected by roof mirrors and comes to the beamsplitter again. With the final wire grid polarizer before the detectors, the beam is separated into horizontal and vertical polarizations, and then the two detectors detect each signal. When there is a different path length of the light, the recombined beam has elliptical polarization. Therefore, the intensities of horizontal and vertical polarizations are different after passing through the final polarizer. The intensities of the horizontal and vertical polarizations are $U_h(t)$ and $U_v(t)$ at the two detectors [90–92],

$$U_h(t) \propto \int_0^\infty I(\omega)\cos^2\frac{\omega t}{2}, \tag{6.76}$$

$$U_v(t) \propto \int_0^\infty I(\omega)\sin^2\frac{\omega t}{2}. \tag{6.77}$$

Also, we define the difference interferogram $\delta(x)$ normalized with the summation of the intensities measured each detector [90–92]

$$\delta(t) = \frac{U_h(t) - U_v(t)}{U_h(t) + U_v(t)} = \frac{\int_0^\infty I(\omega)\cos(\omega t)d\omega}{\int_0^\infty I(\omega)d\omega}. \tag{6.78}$$

Therefore, $I(\omega)$ can be computed by an inverse Fourier transformation of the different interferogram measured at the two detectors.

$$I(\omega) = \mathcal{F}^{-1}[\delta(t)]. \tag{6.79}$$

Comparing a MI with a MPI, for the MI, a part of a beam returns to the radiation source at the beam splitter. On the other hand, for the MPI, the beam intensity after the first polarizer is the same as that of the summation of horizontal and vertical polarizations at the detectors. Therefore, the precision of the MPI is higher than that of the MI, however, the MPI requires two detectors to measure the intensities of horizontal and vertical polarizations.

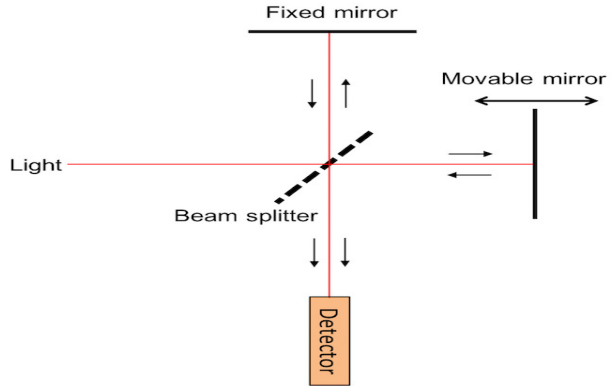

FIGURE 6.16: Sketch of a Michelson interferometer.

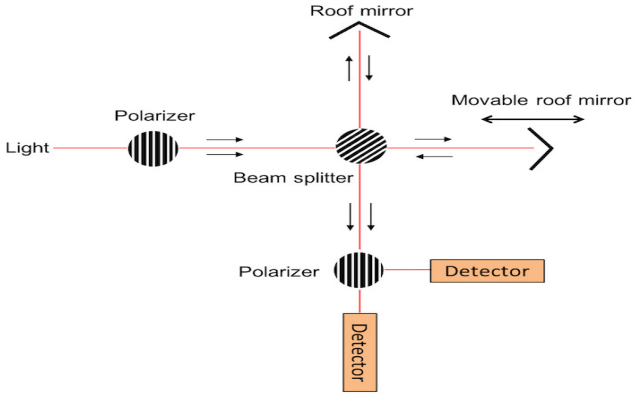

FIGURE 6.17: Schematic of a Martin-Puplett interferometer.

6.8.2 Bolometer and Pyroelectric detector

A bolometer [93] is a kind of thermal detector and is used to measure the power of infrared radiation. Figure 6.18 shows a simple semiconductor bolometer, which consists of an absorber, a thermistor, thermal links, and a heat sink. The absorber supported by two thermal links is away from the heat sink. Light going into a bolometer causes the absorber's temperature to increase and the resistance of the thermistor to decrease. We can know the power of incident light with the temperature change of the absorber obtained by measuring the voltage or the resistance of thermistor. The absorber's temperature becomes the same temperature as the heat sink via the thermal links. Also, the absorber's temperature is extremely sensitive to the thermal background. Therefore, the bolometer is used under vacuum at a low temperature to suppress the background noise.

A pyroelectric detector [93] shown in Fig. 6.18 converts radiation energy into an electrical signal with a ferroelectric material such as TGS or Lithium Tantalate with a large spontaneous electrical polarization depending on temperature. When radiation hits the material in the pyrometer, it causes temperature change of the material. Then, charges on the electrodes are generated due to the pyroelectric effect, and the thermal signal is converted into an electrical signal. As a result, we can obtain the voltage signal depending on the incident radiation energy. Also, a pyroelectric detector is operated at room temperature.

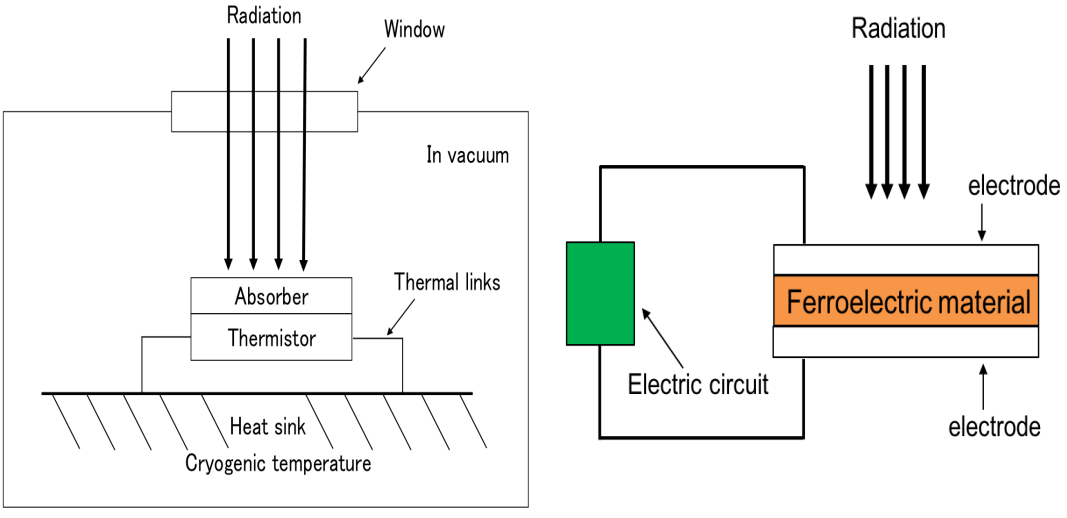

FIGURE 6.18: Simplified bolometer (left) and pyroelectric detector (right).

Chapter 7

THz radiation experiments

We produced micro-bunched beams with about 30 MeV electron beams at the FAST facility in 2017 and examined their characteristics with a skew quadrupole magnet in the chicane. The measured bunch spacing is in reasonable agreement with Eq. (6.32) derived in Sec. 6.2.2. We also tried to detect THz radiation by sending the micro-bunched beams to an Al foil installed downstream of the chicane, however, reproducible data were not obtained. The cause of failure was investigated with GEANT4 simulations . Consequently, we concluded that bremsstrahlung from the slit-mask and the beam pipe in the chicane was the major radiation source. In this section, the details of the experiments with the micro-bunched beams and GEANT4 simulations for bremsstrahlung estimation are described. Moreover, based on the GEANT4 simulations, we designed radiation shielding around the THz detector for the next THz radiation experiments and also determined to use a bolometer which can sensitively measure THz waves.

7.1 RF phases at the minimum energy spread

The transverse emittances were minimized by tuning the solenoid coils around the RF gun. The normalized emittances measured with the "Q-scan" method were (ε_x, ε_y)=($\sim$0.3 μm, $\sim$0.6 μm) at 100 pC/bunch. Similar transverse emittance was measured in the Photo Injector Test facility at DESY, Zeuthen site (PITZ) [50]. Moreover, we need to obtain the RF phases (ϕ_1^0, ϕ_2^0) of CC1 and CC2 at the minimum energy spread to know the energy chirp $h \sim 0$ as a criterion for producing energy chirped beams. All experiments except for the emittance measurement were performed with electron beams with a bunch charge of 200 pC. Using the energy spread measurement mentioned in Sec. 5.1, we identified the RF phases at the minimum energy spread by scanning RF phases of CC1 and CC2 and measured the vertical beam size for each phase at the screen

monitor X124 downstream of the vertical dipole magnet. Figure 7.1 shows the results of each RF phase scan. Here, we set the accelerating gradients of CC1 and CC2 to 14 MV/m. The RF phases at the minimum energy spread were (ϕ_1^0, ϕ_2^0)=(211 degrees, 270 degrees) where the beam size σ_y was the minimum. The on-crest RF phases are (ϕ_1^0, ϕ_2^0)=(214 degrees, 271 degrees), and the RF phases at the minimum energy spread are close to the on-crest RF phases.

Figure 7.2 shows the beam distributions (left images) at the minimum energy spread and the data fitting with the super-Gaussian (right plots) [94] which is effective for a profile with a higher peak and a longer tail than a Gaussian profile. The beam tails in figure 7.2 may be caused by the dark current emitted at the photocathode. The super-Gaussian fitting function is given by

$$f(y) = A \exp\left(-\left(\frac{(y-y_0)^2}{2\sigma_y^2}\right)^P\right), \tag{7.1}$$

where σ_y is the standard deviation and P is the order of the super-Gaussian. Fitting the beam sizes with the super-Gaussian function (Eq. (7.1)), we obtained the minimum energy spread of 5.5×10^{-4} for the electron beam with an energy of ∼34 MeV from

$$\sigma_{\delta_{\mathrm{CC1}}} = \frac{\sigma_y}{|\eta_y|} \simeq 5.5 \times 10^{-4}, \qquad \sigma_{\delta_{\mathrm{CC2}}} = \frac{\sigma_y}{|\eta_y|} \simeq 5.4 \times 10^{-4}. \tag{7.2}$$

The fitted P for each case is P_{cc1}=0.54 and P_{cc2}=0.48. The energy spread $\sigma_{\delta_{gun}}$ at the exit of the RF gun (∼5 MeV) is

$$\sigma_{\delta_{gun}} = 5.5 \times 10^{-4} \times \frac{34\,\mathrm{MeV}}{5\,\mathrm{MeV}} \sim 3.7 \times 10^{-3}. \tag{7.3}$$

We assumed that the electron beam has an energy spread of 0.2% after the gun, however, the energy spread $\sigma_{\delta_{gun}} = 0.37\%$ at about 5 MeV is larger than that we assumed.

7.2 Micro-bunched beam production and measurements

In the experiments, we produced an energy chirped beam with off-crest RF phases. When an electron beam is accelerated in an off-crest RF phase in CC1 or CC2, the electron beam energy is reduced. Therefore, we tune the accelerating voltages of CC1 so that the electron beam always has an energy of 30 MeV in an RF phase range of $-35^\circ \leq \phi_1, \phi_2 \leq 35^\circ$ relative to on-crest operation. We set the RF phases of CC1 and CC2 to the minimum energy spread and transmitted the electron beams to the chicane without particle loss. The beam position was then close to the center of the screen monitor X115 in the middle of the chicane. Since the beam position in the chicane

changes with energy, we maintained nearly constant energy for the different RF phases by choosing the accelerating voltages of the two cavities so that the electron beams always came to the same position at X115.

The dispersion of the chicane at the slit-mask is designed to be 0.32 m, as mentioned in Sec. 4.2. We focused the electron beam in the horizontal plane to be as small as possible at the slit-mask, and then the beam profile and the curve fitting are shown in Figure 7.3. By fitting the beam profile with the super-gaussian, the horizontal beam size $\sigma_x \sim 0.22$ mm and the fitted $P \sim 0.41$ can be obtained at the beam focus. The minimum horizontal beam size $\sigma_{x,min}$ at the slits where we can measure using the screen monitor can be computed as

$$\begin{aligned} \sigma_{x,min} &= \sqrt{\varepsilon_x \beta_x + (\eta_x \delta)^2} \simeq \eta_x \delta \\ &= 0.32 \text{ m} \times 5.5 \times 10^{-4} \times \frac{34 \text{ MeV}}{30 \text{ MeV}} \\ &\sim 0.2 \text{ mm}. \end{aligned} \tag{7.4}$$

The dispersion η_x at the slit-mask is 0.32 m, and δ is 5.5×10^{-4} at 34 MeV from Eq. (7.2). The beam size $\sigma_x = 0.22$ mm measured with the YAG screen is consistent with $\sigma_{x,min} = 0.2$ mm.

When the skew quadrupole magnet in the chicane is turned on, the vertical beam size becomes large due to the y-dispersion. We focused the vertical beam size at X120 downstream of the chicane using quadrupole magnets placed before and after the chicane. Figure 7.4 shows beam sizes at X120 before and after the increased focusing. The RF phases of CC1 and CC2 are set to (ϕ_1^0, ϕ_2^0) where the energy spread is minimum. The

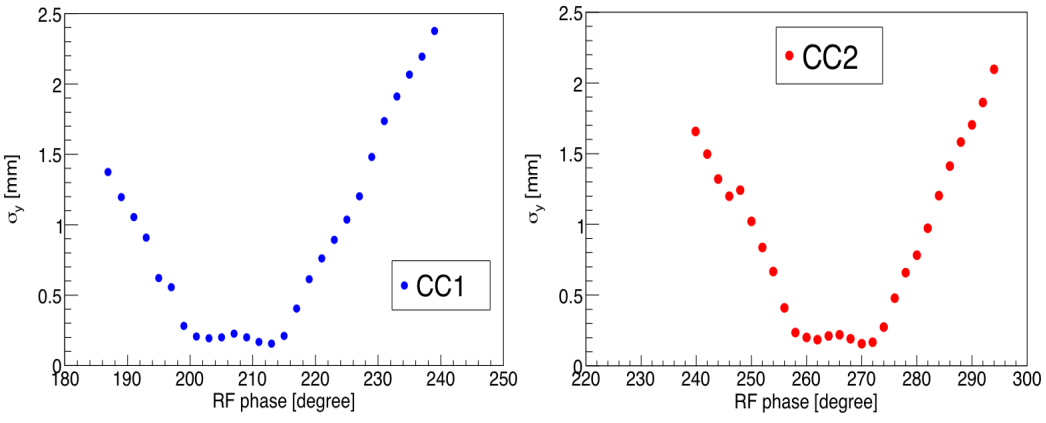

FIGURE 7.1: Vertical beam sizes at X124 depending on RF phases. Upper and bottom plots represent CC1 and CC2 phase scans, respectively.

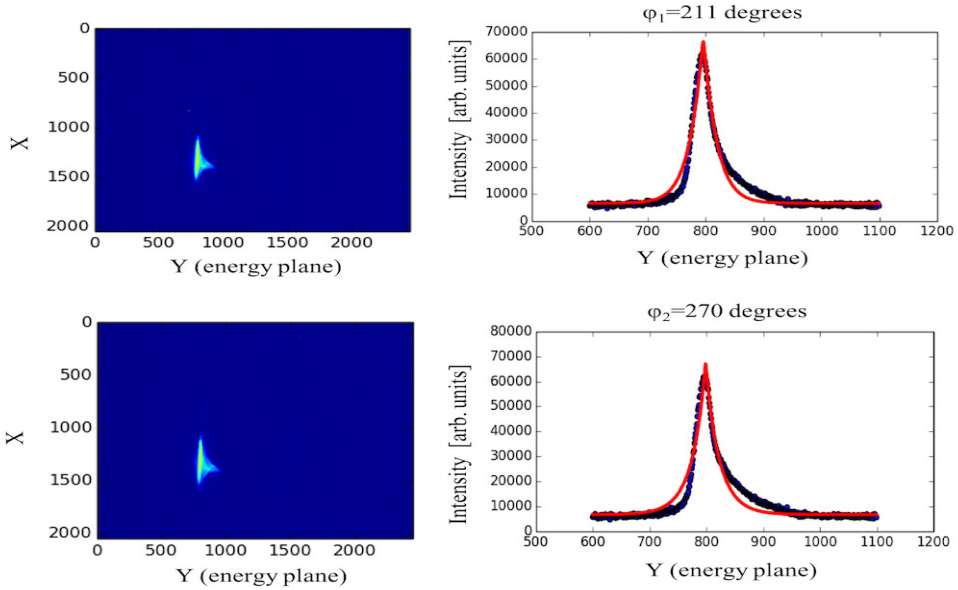

FIGURE 7.2: Vertical beam distributions at the minimum energy spread at X124. They are fitted with the super-gaussian due to the beam tail. Upper plots represents the CC1 chirp and bottom plots shows the CC2 chirp.

vertical rms beam size was reduced to $\sigma_y = 0.25$ mm from $\sigma_y = 0.34$ mm without the additional focusing.

We inserted the slit-mask in the middle of the chicane and set the skew quadrupole magnet current to 0.9 A. Keeping CC2 phase to that corresponding to the minimum energy spread, we took beam profiles scanning the RF phase of CC1 to values (relative to the on-crest phase) of $-29.4°$, $0°$, $10°$, $20°$, $30°$, and the results are shown in Figure

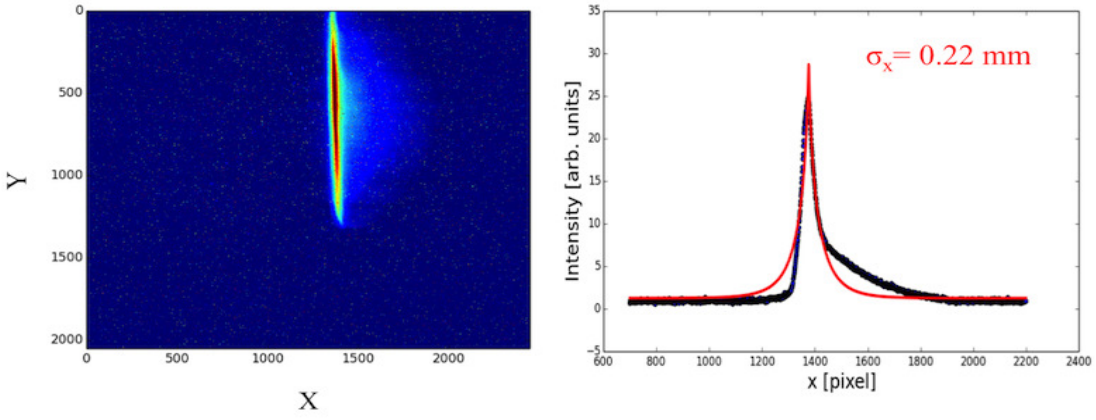

FIGURE 7.3: Beam distributions at the slit-mask (X115) after horizontal beam focus. The RF phases of CC1 and CC2 are set to the minimum energy spread. Left image is the beam distribution and right red plot shows the curve fitting.

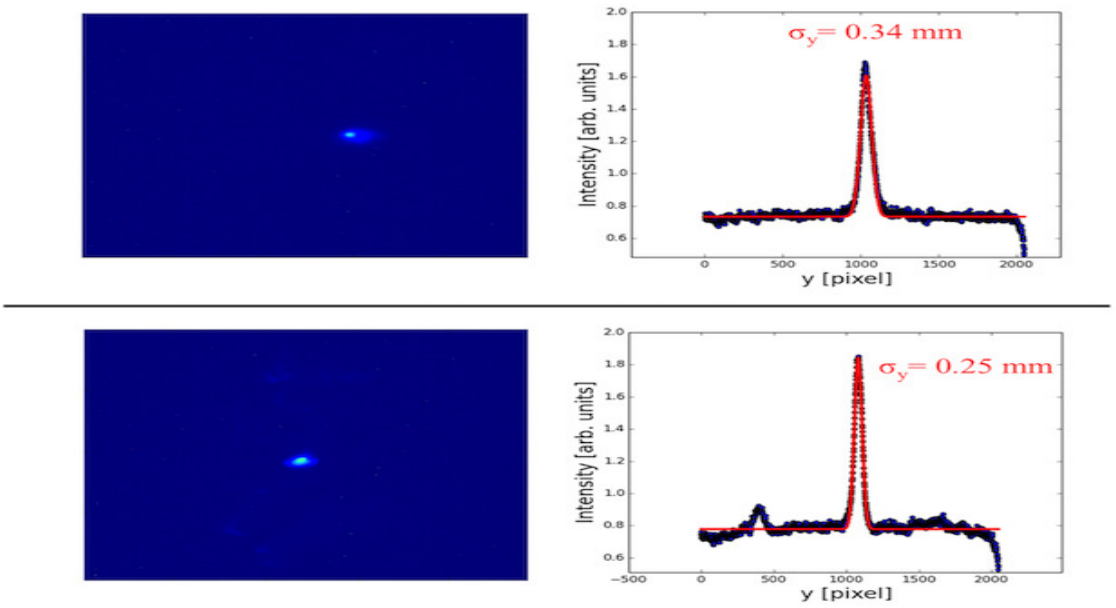

FIGURE 7.4: Vertical beam sizes at X120 before (top) and after (bottom) additional focusing. Left plots represent the beam images and right plots represent the histogram of the vertical distributions.

7.5. Also, Table 7.1 shows the energy chirps corresponding to the CC1 RF phases. The beams are separated in the y-plane, and the vertical spacings are ∼0.8 mm at each phase. Eq. (6.32) derived in Sec. 6.2.2 shows that the vertical spacing is independent of the RF phase and depends on the K-value (current) of the skew quadrupole magnet. We obtained constant vertical spacing for different energy chirps, and hence the vertical spacing is independent of RF phases.

The beam profiles at ±30° and 20° have different σ_x along the vertical axis (energy axis). The bunch head (low energy) at −30° (max. compression) is focused stronger than the bunch tail (high energy), and that is opposite at 20° and 30°. At 0° (minimum energy spread) and 10°, the differences of σ_x along the vertical plane are not seen. Therefore, that can be interpreted as the chromatic aberrations due to large energy spreads.

Next, we scanned the skew quadrupole current for two cases (CC1, CC2)=(0°, +30°) and (+30°, 0°). Figure 7.6 shows the vertical spacing's dependence on the skew quadrupole current in the two cases. The vertical spacing is proportional to the skew quadrupole magnet as we expected in Eq. (6.32) .

TABLE 7.1: Energy chirps corresponding to CC1 RF phases.

CC1 RF phase	-30°	0°	10°	20°	30°
Energy chirp	5.6 m^{-1}	0 m^{-1}	-1.8 m^{-1}	-3.7 m^{-1}	-5.7 m^{-1}

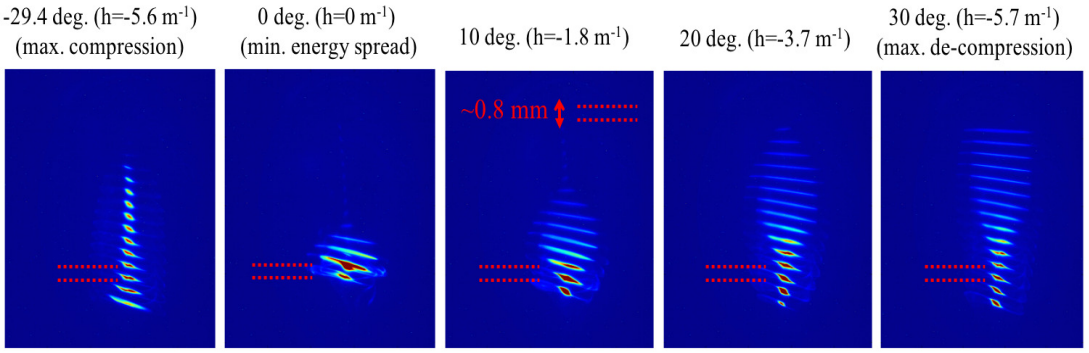

FIGURE 7.5: Beam distributions at X120 at each RF phase of CC1 when the slit-mask is inserted and the skew quadrupole magnet is set to 0.9 A.

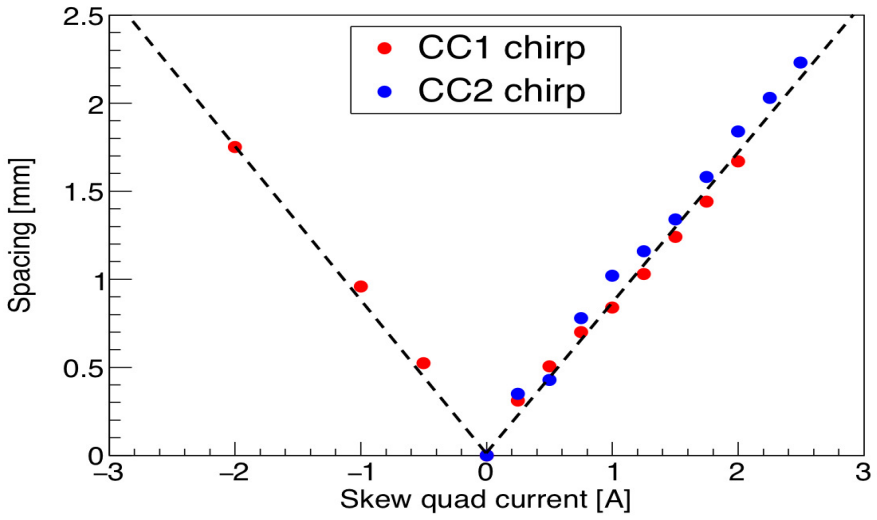

FIGURE 7.6: Vertical spacing depending on the current of the skew quadrupole magnet at (CC1, CC2)=(0°, +30°) and (+30°, 0°).

7.3 Micro-bunched beam measurements with pyrometers

When the electron beam goes through the Al foil installed at X121 (see Fig. 3.2) CTR is emitted and extracted to the pyrometers [IntraTec] through the Martin-Puplett interferometer [92, 95]. The detector's geometry is shown in Figure 7.7. First, we measured TR with the maximum longitudinal compression of the electron beam. Figure 7.8 shows the autocorrelation function and the frequency spectrum detected with pyrometers in this case. Here, we used the fitting function f_{fit} with a low frequency cut-off function

f_{filter} [96, 97]

$$f_{fit}(\omega) = A \cdot f_{filter}(\omega) \left| \exp \frac{-\omega^2 \sigma_b^2}{2} \right|^2 + B, \tag{7.5}$$

$$f_{filter}(\omega) = 1 - \exp\left(-\frac{\omega}{\omega_0}\right)^4, \tag{7.6}$$

where ω_0 is the characteristic cut-off frequency, and A, B are the constants. From Fig. 7.8, we obtained the bunch length of $\sigma_z \sim 0.7$ ps (0.21 mm) for maximum compression [97], which is consistent with the bunch length measured at FAST [98].

We set the RF phase of CC1 to maximum lengthening and measured the autocorrelation function with the pyrometers in the same way. Figure 7.9 shows the autocorrelation functions and frequency spectra for the same condition on different days. The autocorrelation function has two peaks with a time interval of ∼4 ps in the top left plot, and the frequency spectrum in the top right plot has a fundamental frequency of ∼0.3 THz which is consistent with the simulation. However, when we performed the same measurement under the same conditions on a different day, we obtained different results, shown in the bottom plots in Fig. 7.9. The same autocorrelation function was not obtained. This might be due to background radiation from the slit-mask. We did not have in place radiation shielding around the box with the Martin-Puplett interferometer and pyrometers.

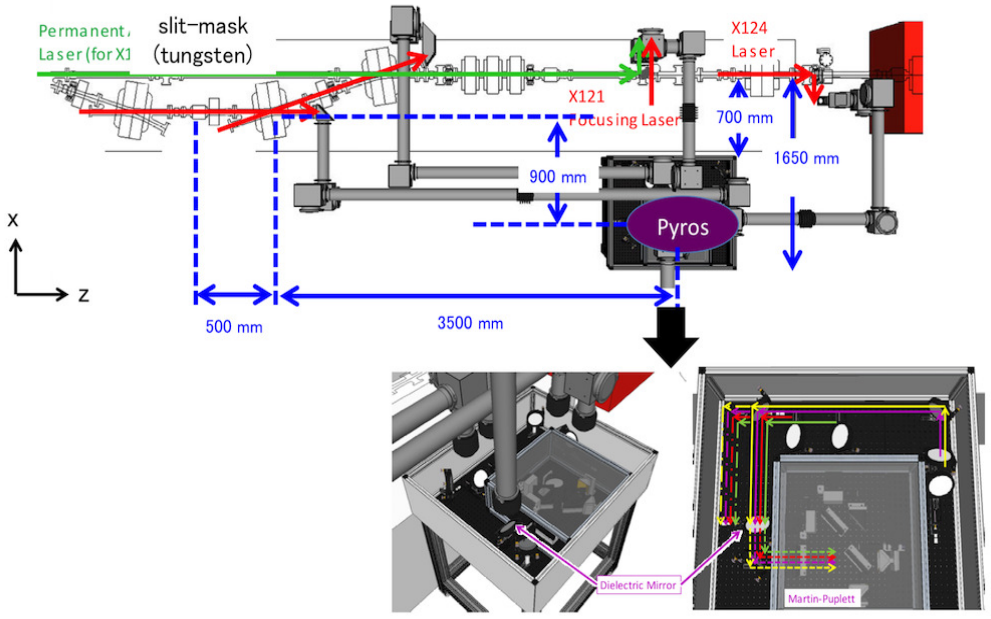

FIGURE 7.7: Beamline geometry and pyrometers [95].

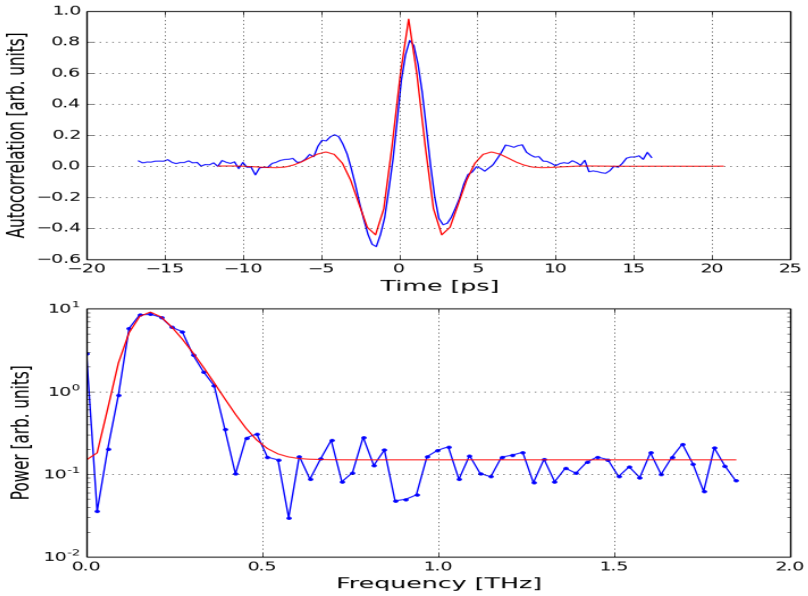

FIGURE 7.8: The autocorrelation function (top) and the frequency spectrum (bottom) for the maximum longitudinal compression of the beam.

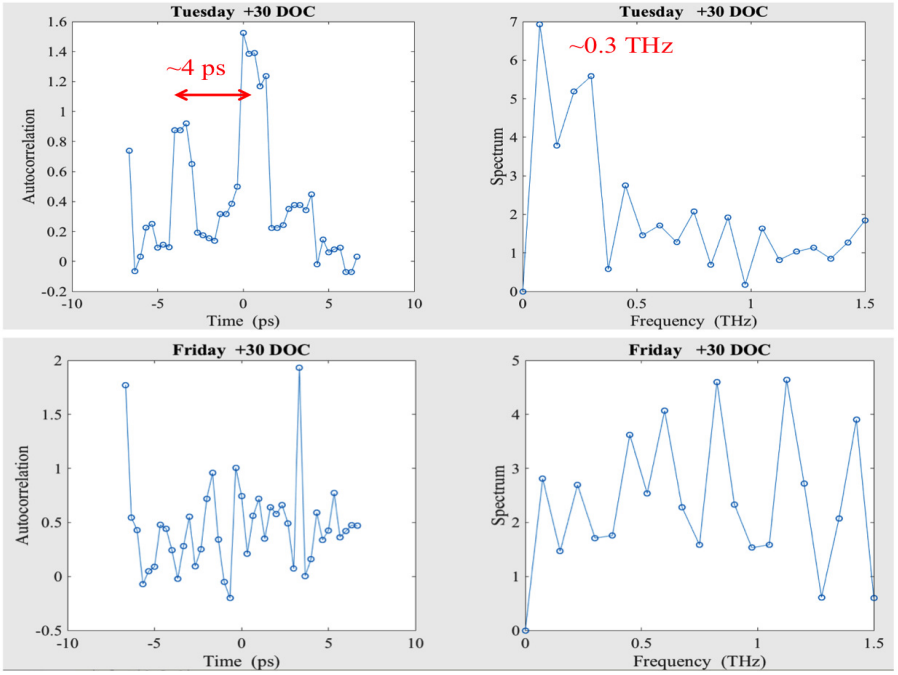

FIGURE 7.9: The autocorrelation functions with pyrometers and the frequency spectra when the electron beam bunch is lengthened. The top plots show the results obtained on 12/1/2017 and the bottom plots show the results obtained on 11/28/2017, under the same conditions.

7.4 Bremsstrahlung from the slit-mask and beam pipe

To identify whether the spectra in Fig. 7.9 are from bremsstrahlung or not, we performed GEANT4 simulations to calculate the flux of different particles generated at the slit-mask and beam pipe in the chicane entering the pyrometers. Since GEANT4 requires the electron beam distributions at the entrance of the slits as the initial condition, we use the distribution obtained with the ELEGANT code. The simulation parameters were as follows: beam energy = 30.4 MeV, the number of electrons = 10^6, and the beam size at the slits $(\sigma_x,\ \sigma_y) = (1.8\,\text{mm},\ 0.2\,\text{mm})$. The number of electrons was about three orders of magnitude smaller than the bunch population in the experiments due to the computational time for the simulations. The detector box was placed at $(x, y, z) = (-0.9\,\text{m}, 0\,\text{m}, 4.0\,\text{m})$ from the slit-mask $((x, y, z) = (0\,\text{m}, 0\,\text{m}, 0\,\text{m}))$ (see Fig. 7.7). Figure 7.10 shows the GEANT4 simulation results of the electron beam's transverse size and energy distributions after going through the slit-mask. The x-y distribution simulated with GEANT4 is consistent with that simulated using ELEGANT. About 5% of the incident electron beam can go through the slits without interacting with the slits. The other particles (95%) of the beam scatter off the slits and the beam pipe, and many photons and particles are generated and become background noise in the detectors.

Figure 7.11 shows the x-y distributions at $z = 3.5$ m for each particle type and the red boxes in Fig. 7.11 represent the place of the detectors. The GEANT4 simulation results show that electrons, photons, neutrons, and positions are emitted from the slit-mask and the beam pipe. The electrons represent secondary particles, which are not the incident electrons going to the slit-mask. The electrons are produced due to the pair production ($\gamma \rightarrow e^- + e^+$), the photoelectric effect, and ionization. Photons are generated

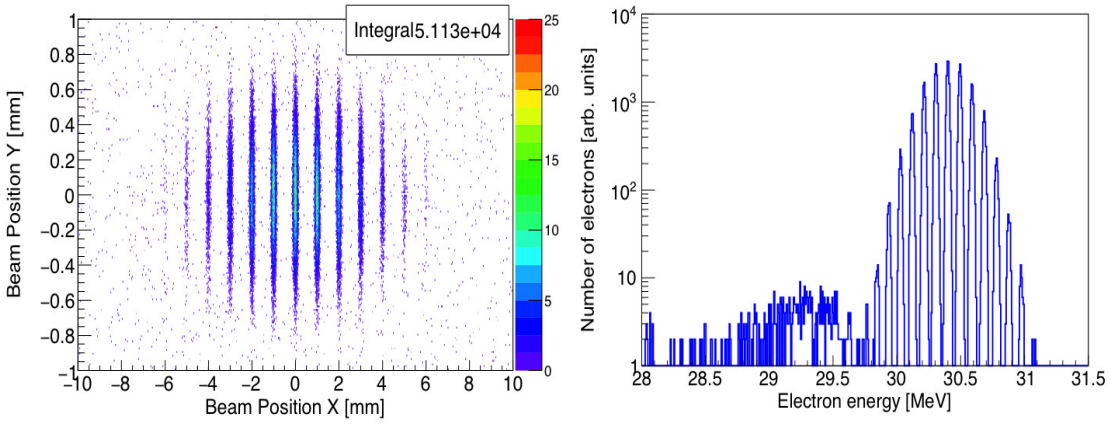

FIGURE 7.10: Electron beam (left) and energy (right) distributions after the slit-mask.

via bremsstrahlung and also from electron-positron annihilation ($e^- + e^+ \rightarrow \gamma + \gamma$). The main source of neutron production is the photonuclear reaction. From Fig. 7.11, electrons, photons, and positrons form the main background sources and should be suppressed to be zero ideally.

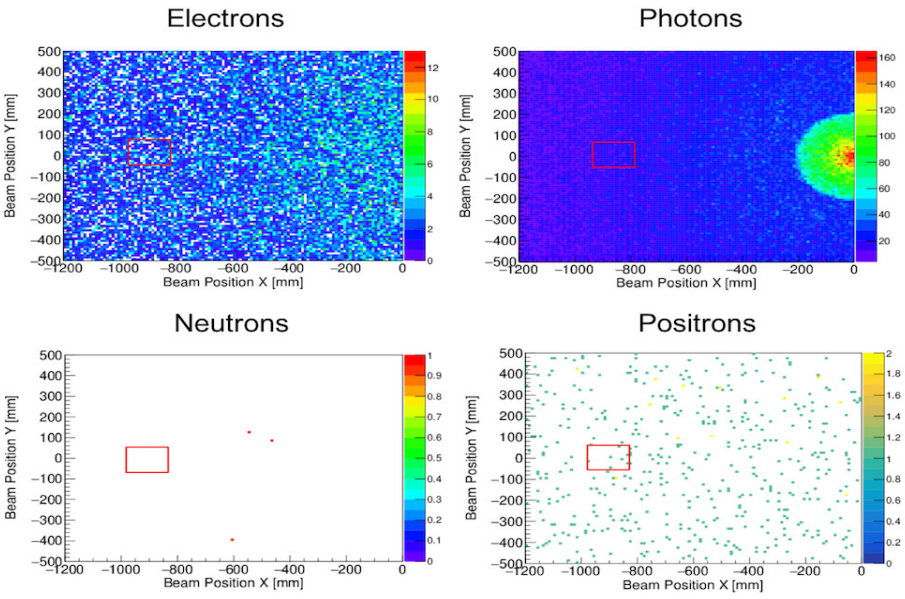

FIGURE 7.11: Transverse distributions of Electrons, photons, neutrons, and positron distributions at z=4 m (around the pyrometers). Red boxes represents detector's position.

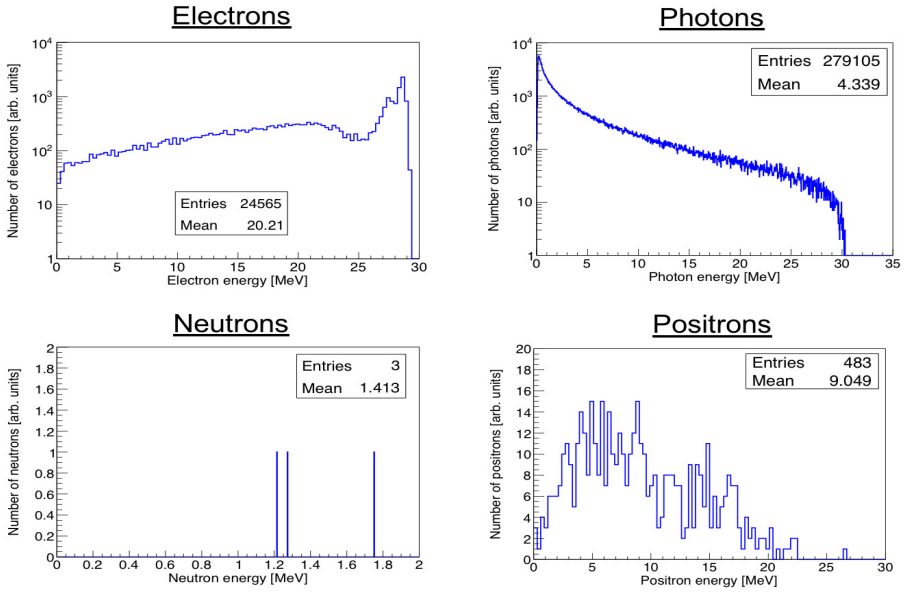

FIGURE 7.12: Energy distributions of Electrons, photons, neutrons, and positron distributions at z=4 m (around the pyrometers).

7.5 Radiation shielding for upcoming THz radiation experiments

To suppress the background for the upcoming THz radiation experiments, radiation shielding is needed at appropriate places. From Fig. 7.10, photons and secondary electrons are the main background source, while the interaction of the photons with the nuclei of the materials causes the positron production. Since the pyrometers may not be sensitive enough to detect the levels of THz radiation expected in the experiment, we will use a more sensitive detection system consisting of a Michelson interferometer and a cryogenically cooled bolometer. This THz detect system is placed upstream of the box with the pyrometers, and it is shown in Figure 7.13.

GEANT4 simulations were performed to determine appropriate thickness and placement of the shielding. Lead bricks will be used for the radiation shielding since the main background is from photons. For the simulations, we assumed four cases (Case A, B, C, and D) for different radiation shielding positions close to the chicane and/or the bolometer. Shielding thicknesses of (x, y, z)=(30 cm, 20 cm, 20 cm) and (30 cm, 10 cm, 50 cm) are assumed to absorb high energy photons and particles. Figure 7.14 shows the simulation geometries for the four cases.

Figure 7.15, 7.16, 7.17, and 7.18 show the electron, photons, positron, and neutron distributions around the bolometer for each case at $z = 3.5$ m around the THz detector system. The red boxes in Fig. 7.15-7.18 represent the window of the bolometer. All particle counts except for photons are zero at the bolometer. The photon count is also zero, except in case B where one photon hits the detector. We note however that

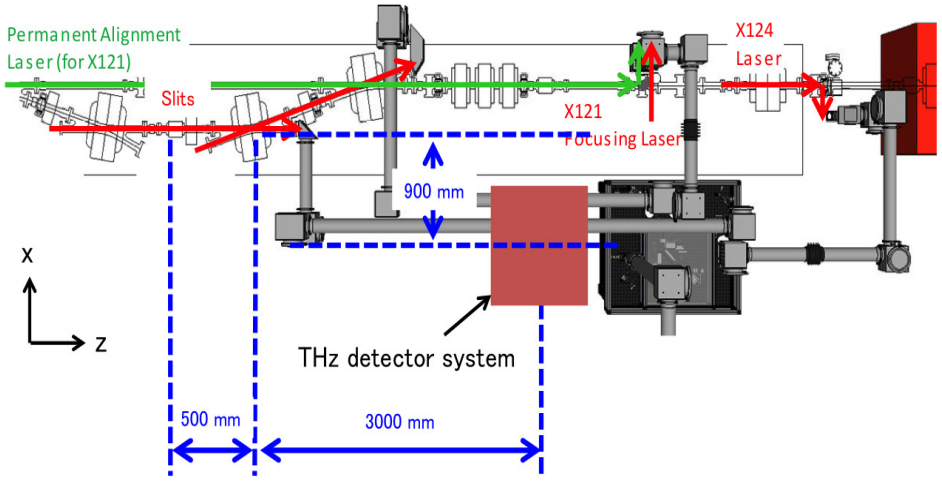

FIGURE 7.13: THz detector system with the Michelson interferometer and a bolometer.

these are low statistics simulations. In the experiment, particle fluxes of all types will be significantly higher. Nevertheless, we can draw the following conclusions from the experiments: 1) Photons are the main background source, so lead bricks should form an effective shield, 2) Cases A and B are more effective at shielding than cases C and D, because they have a larger solid angle coverage of the radiation from the slit mask and the beam pipe. This information will be useful in setting up the initial radiation shielding geometry during the experiments and will be subsequently optimized.

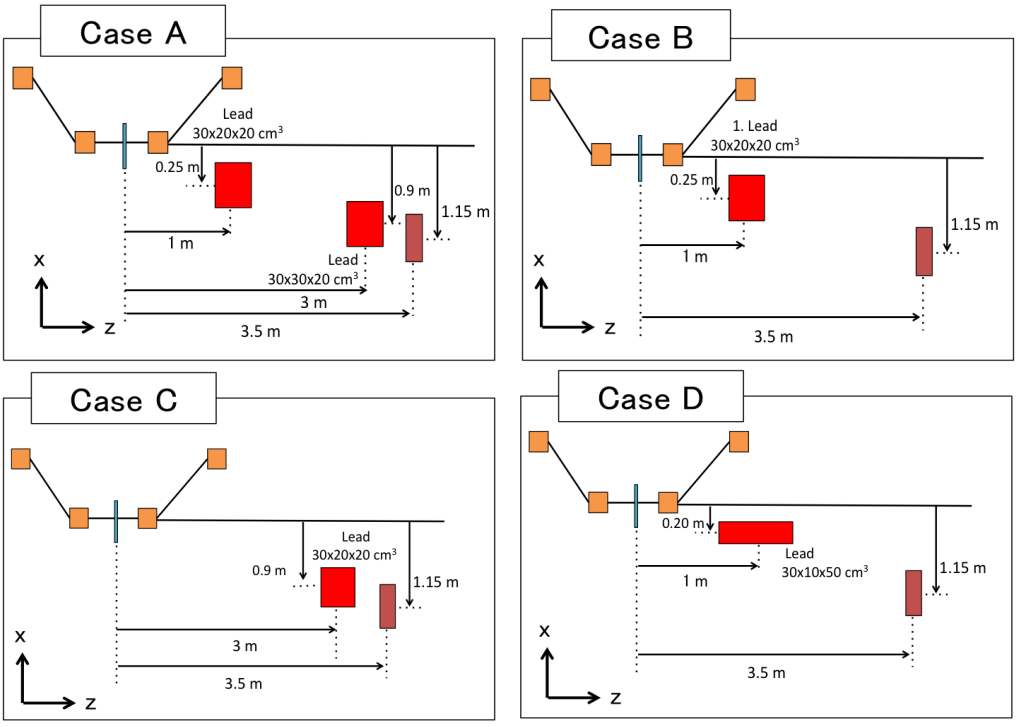

FIGURE 7.14: Simulation geometries for different radiation shielding places. Red boxes and brown boxes represent lead shielding and optical breadboards with the THz detector system, respectively.

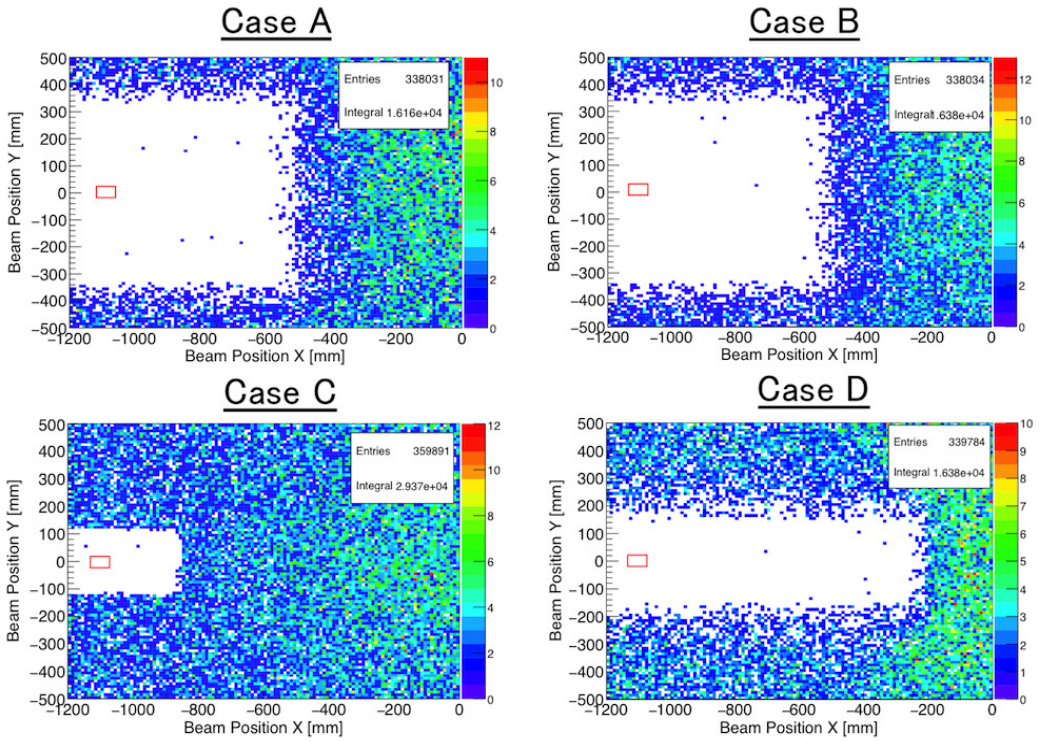

FIGURE 7.15: Electron distributions for each case at the bolometer. The THz detector is placed at red boxes.

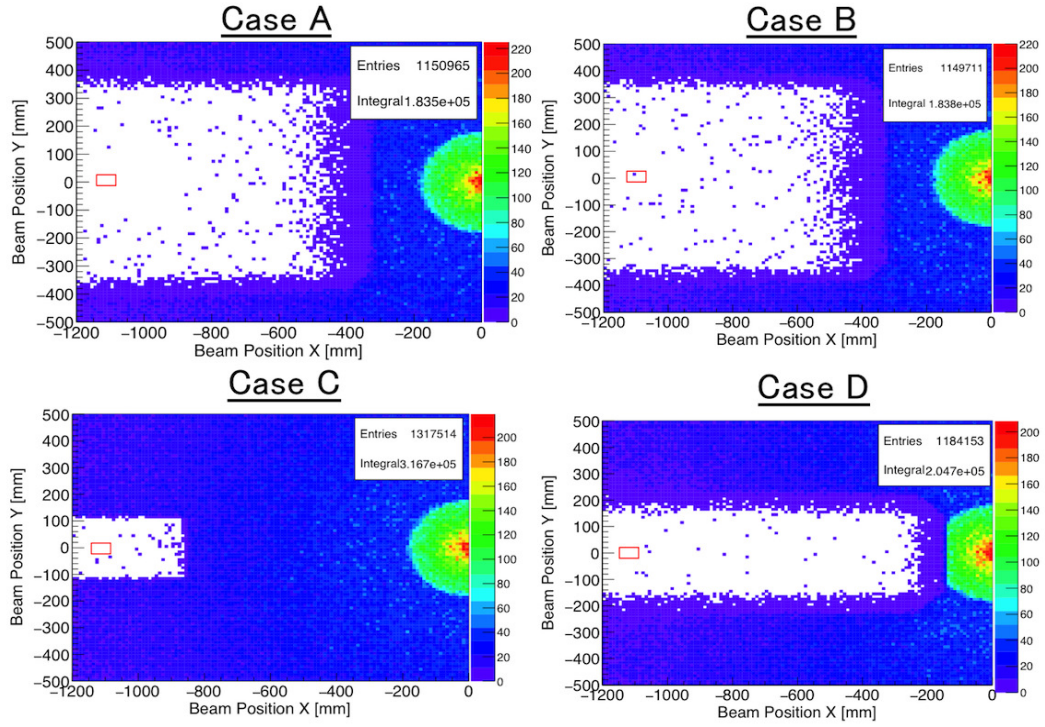

FIGURE 7.16: Photon distributions for each case at the bolometer. The THz detector is placed at red boxes.

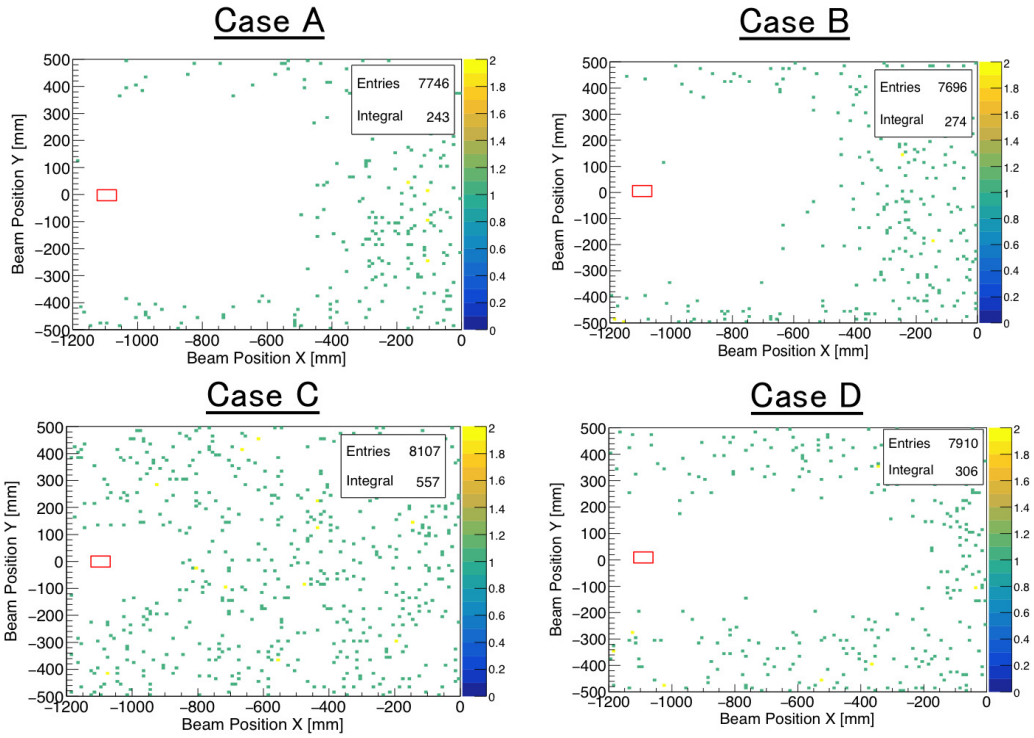

FIGURE 7.17: Positron distributions for each case at the bolometer. The THz detector is placed at red boxes.

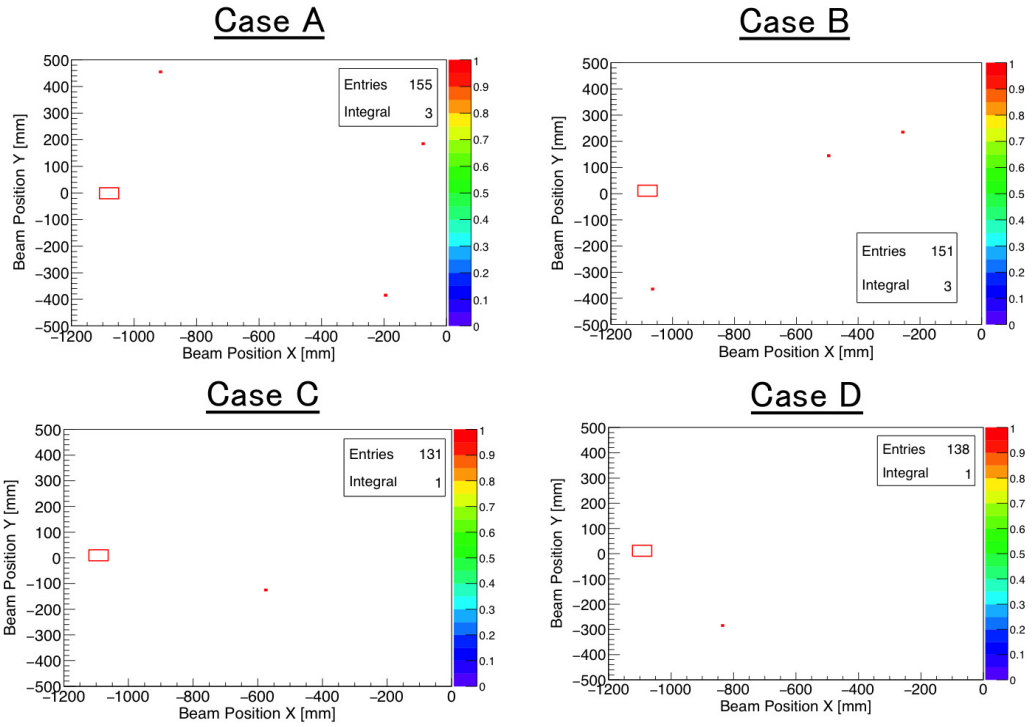

FIGURE 7.18: Neutron distributions for each case at the bolometer. The THz detector is placed at red boxes.

7.6 Experimental setup for upcoming THz radiation experiments

We will detect THz radiation with a Michelson interferometer and a bolometer in the next THz radiation experiments [11]. First, we assembled a Michelson interferometer consisting of an inconel beam splitter whose reflection/transmission ratio is 40%/40% (Edmund Optics), three flat mirrors with a diameter of 3 inches (Edmund Optics), and a parabolic mirror (Edmund Optics) with a focal length of 127 mm for a beam focus to a bolometer window. The one flat mirror is fixed on a movable stage with a slide stroke of 100 mm, and the other ones are fixed on an optical breadboard. The assembled Michelson interferometer is housed inside an aluminum box to prevent the effect of visible light to the interferometer.

We installed the box with the Michelson interferometer upstream of the Martin-Puplett system. Figure 7.19 shows the installed Michelson interferometer. CTR radiated at X121 is transported through a stainless pipe with a diameter of 4 inches to the bolometer. The stainless pipe can also be filled with Nitrogen gas to avoid the absrption of the THz radiation in the air. The alignment is adjusted with a red laser attached to a vacuum window close to X121, and the laser can be transported from X121 to the exit of the Michelson interferometer, see the bottom left image in Fig. 7.19.

Figure 7.20 shows the helium-cooled bolometer (HDL-5 model, IRLabs) which we will use. This bolometer is the same one used for THz radiation experiments using an RF deflector (transverse-longitudinal emittance exchanger) at the A0 photo-injector [11]. The helium and nitrogen tank capacities of this bolometer are 1.2 L and 0.8 L, respectively, and the bolometer can be cooled down to 4 K. Then, the standard holding time is over 20 hours at 4 K. This bolometer is installed next to the Michelson interferometer box, see Fig. 7.19. Also, radiation shielding will be placed around the interferometer box and the bolometer to suppress photons and secondary particles radiated from the slit-mask and the beam pipe in the beamline.

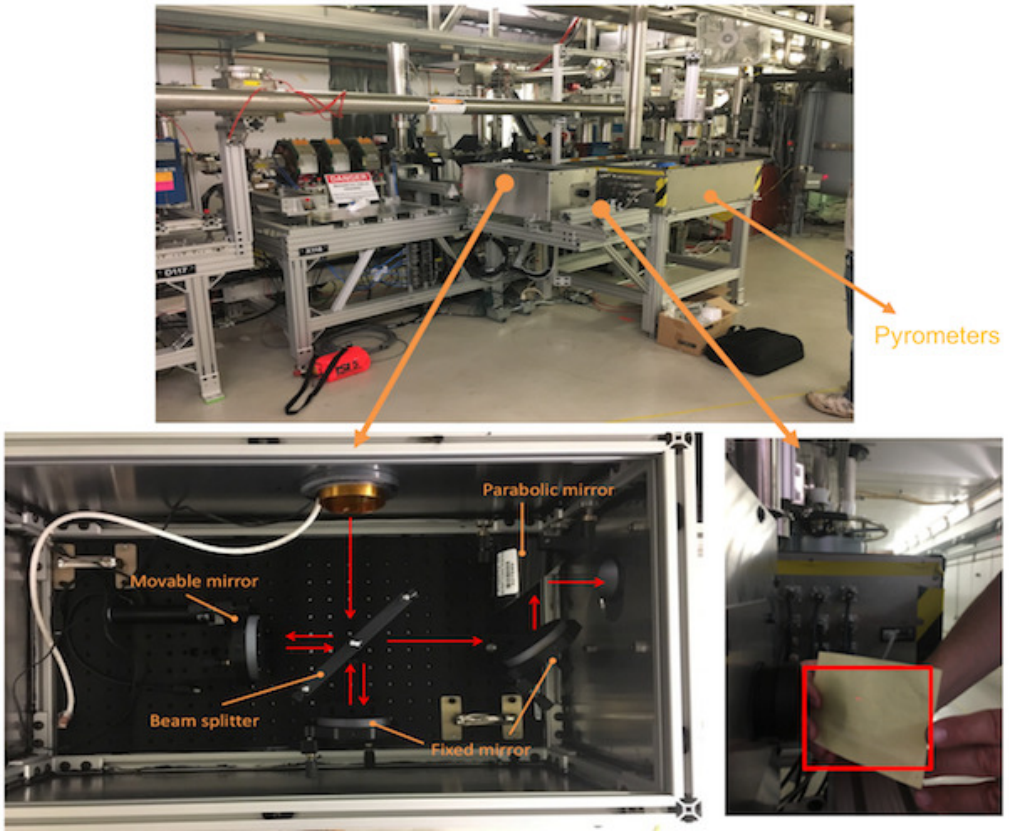

FIGURE 7.19: The Michelson interferometer installed upstream of the Martin-Puplett interferometer.

FIGURE 7.20: A He-cooled bolometer (HDL-5 model, IRLabs). The left picture represents a window of the bolometer.

7.7 Summary of THz radiation experiments

We performed the first set of THz radiation experiments with 30 MeV electron beams at the FAST facility. First, we measured the uncorrelated energy spread at a higher energy of 34 MeV and obtained the energy spread of 0.055%. It is equivalent to δ=0.37% at 5 MeV after the RF gun. This value is about two times larger than that of our expectation value of <0.2%. To decrease the energy spread, the commissioning of the RF gun such as the tuning of the RF gun phase and improvement of the longitudinal profile of the laser needs to be done.

We accelerated the electron beams with RF phases relative to the minimum energy spread of (-30°, 0°, 10°, 20°, 30°) in both cavities, and turned on a skew quadrupole magnet after inserting a slit-mask in the middle of the chicane. At the screen monitor X120 downstream of the chicane, vertically separated electron beams could be measured for each RF phase. The vertical spacings of the micro-bunched beams did not change and also was constant for the different energy chirps, which is in agreement with that of Eq. (6.32). Moreover, when we varied the current of the skew quadrupole magnet at (CC1, CC2)=(0°, +30°) and (+30°, 0°), the vertical separations are proportional to the current, and there is not much difference between the CC1 chirp and the CC2 chirp. This result is also consistent with that of our simulations (see Fig. (6.10)).

We emitted CTR by sending micro-bunched beams to an Al foil downstream of the chicane. When the electron beam was maximally compressed longitudinally without the slit-mask, the autocorrelation function was measured using the THz detector system which combined two pyrometers and a Martin-Puplett interferometer. From the obtained data, the minimum bunch length was about 0.7 ps (0.21 mm), which is in reasonable agreement with bunch length measured before [98]. Although we inserted the slit-mask and tried to measure the autocorrelation at the maximum bunch lengthening mode, reproducible data were not obtained. From the simulations with GEANT4, we expect that many photons, secondary electrons, and positrons were generated from the slit-mask and beam pipe, and they went to the detector. Therefore, we concluded that bremsstrahlung from the slits and the beam pipe was the main source of the detected radiation.

We will measure THz radiation during the next experiments at the FAST facility. We will install radiation shielding using lead bricks and a new detector system consisting of a bolometer and a Michelson interferometer. Simulations with GEANT4 showed that the shielding with a thickness (z-direction) of least 200 mm and placed around the slit-mask and the THz detector is effective in significantly reducing the background at the detector.

Chapter 8

Optics design and simulations for Channeling Radiation

We performed simulations and experiments of Channeling radiation (CR) using an electron beam of an energy of 43 MeV and a single diamond crystal with a thickness of 168 μm. First, this section briefly presents the energy, yield, and brilliance of CR. When an electron beam travels with a sufficiently small transverse momentum with respect to a crystal plane, the electrons can be captured in bound states of the crystal's transverse potential, and consequently emit CR. Electron motion in the crystal is similar to that in an undulator, and the vibration period is very short, therefore, high energy X-rays can be emitted using a comparatively low energy electron beam. In other words, photon energy radiated from an electron beam traveling a crystal, which is not so high, is shifted to the higher energy due to the Doppler effect in the forward direction. An important requirement for CR is that the electron beam divergence at the crystal must be smaller than the critical angle θ_c [99]. If beam divergences are larger than the critical angle, electrons in the crystal have too large a transverse momentum to be captured by the crystal potential; this is called de-channeling. The critical angle θ_c for CR is given by

$$\theta_c = \sqrt{\frac{2\gamma V_{max}}{mc^2(\gamma^2 - 1)}} \sim \sqrt{\frac{2V_{max}}{mc^2\gamma}}, \tag{8.1}$$

where V_{max} is the transverse potential of a crystal, m is the electron mass, c is the speed of light, and γ is the Lorentz factor. For an electron energy of 43 MeV and a diamond crystal with the (110) plane, the critical angle $\theta_c = 1.1$ mrad using Eq. (8.1).

The energy spectrum of CR for electron energies below 100 MeV, derived by solving Schrodinger equation, is discrete [19–22]. Electrons bound by the potential of a crystal plane or axis have discrete energy levels, and spontaneous transitions between the energy

states generate quasi-monochromatic CR. On the other hand for electron energies above ∼100 MeV, the energy spectrum of CR can be described by classical electrodynamics, and it is broad and continuous [99]. The CR energies for electron energies below 100 MeV are given by [99]

$$E_\gamma = 2\gamma^2 \frac{(\epsilon_i - \epsilon_f)}{(1+\gamma^2\theta^2)}, \tag{8.2}$$

where θ is the angle of the emitted photon from the incident electron, ϵ_i and ϵ_f are the energy eigenvalues of electrons in energy levels i and f. This equation also shows that the CR energy can be tuned by changing the electron energy since $E_\gamma \propto \gamma^2$. The CR spectrum calculations reported here were done using a Mathematica notebook which was significantly corrected and modified from the published version [100], this modified version was used to successfully compare simulations with experimental results from a previous channeling experiment [34]. The CR energies for a diamond crystal and 43 MeV electron energy are shown in Table 8.1 for photons emitted at an angle of 0 degrees with respect to the incident electron beam.

The photon yield for states $i \to f$ per steradian per photon energy per electron is written as [20, 34, 100, 101]

$$\begin{aligned}\frac{d^2N}{d\Omega dE_\gamma}(i\to f) &= \frac{\alpha_f \lambda_f^2}{\pi^{5/2}\hbar c} 2\gamma^2(\epsilon_n - \epsilon_m)|\langle\psi_f|\frac{\partial}{\partial x}|\psi_i\rangle|^2 \int_0^d \exp[-\mu(E_\gamma)(d-z)]P_n(z) \\ &\times \int_0^\infty dt \frac{t^{-1/2}(1+2\alpha^2 t)(\Gamma_T/2)e^{-t}}{[(1+2\alpha^2 t)E_\gamma - E_0]^2 + [(1+2\alpha^2 t(\Gamma_T/2))]^2},\end{aligned} \tag{8.3}$$

where α_f is the fine structure constant, λ_c the Compton wavelength of the electron, ϵ_n, ϵ_m, the energies of the state n, m, d the crystal thickness, $\mu(E_j)$ the photon absorption coefficient, E_γ the photon energy, Γ the total line width of the transition $n \to m$, E_0 photon energy at zero angle, $\alpha = \gamma\theta_{MS}$: the multiple scattering angle, $P_n(z)$ the occupation probability of channeling state n at crystal depth z, and $\psi_{(m,n)}$ the eigenfunction of state m, n.

Also, $P_n(\theta)$ is [100, 102]

$$P_n(\theta) = |\langle\psi|\exp(ik_x x)\rangle|^2 = \frac{1}{d_p}\left|\int_{-d_p/2}^{d_p/2} \psi_i \exp ik_x x dx\right|^2. \tag{8.4}$$

One of the requirements for high intensity photons is to make $P_n(\theta)$ large. We calculated the occupation of different channeling states with Eq. (8.4). Figure 8.1 shows the initial populations as a function of the beam divergence at the crystal entrance for states of n=0, 1, 2, and 3 when the electron beam is incident at a zero angle to the crystal. Black, red, blue, and green lines are for n=0, 1, 2, and 3, respectively. The beam divergence except for the state of $n = 1$ should be low to generate high intensity photons. In the

state of n=1, the initial population has a distribution with a peak at a beam divergence of about 0.35 mrad.

The photon yields for beam divergences of 0.1 mrad, 0.3 mrad, 0.9 mrad, and 1.1 mrad at the crystal were calculated, and the results are shown in Figure 8.2. The energy widths are about 10% for the different divergences, and photon intensities are higher for smaller beam divergences. A crystal thickness is the important parameter to generate a high photon yield and needs to be determined considering the absorption length of a photon, the occupation length, de-channeling, and re-channeling. Although the emission of the maximum photon yield requires ∼300 μm thickness [34], here we use a diamond crystal of 168 μm.

In general, the quality of X-ray sources such as synchrotron radiation and XFEL is evaluated with the spectral brilliance [photons/s/mrad^2/mm^2/0.1%bandwidth]. The average brilliance of CR emitted from electrons can be expressed as [34]

$$B_{av} = \frac{I_{av}}{e}\frac{\gamma^2 Y(\sigma'_e)^2 10^{-3}}{\epsilon_N^2 \Delta E_\gamma/E_\gamma} Erf\left[\frac{\theta_c}{\sqrt{2}\sigma'_e}\right] \text{ photon/s/(mm} - \text{mrad)}^2/0.1\%\text{BW}, \quad (8.5)$$

where I_{av} is the average electron beam current, e is the elementary electron charge, Y is the total photon yield per electron, ϵ_N is the normalized emittance, θ_c is the critical angle, see Eq. (8.1), $\Delta E_\gamma/E_\gamma$ is the relative width of the X-ray line, σ'_e is the electron beam divergence, and Erf is the error function. According to the Eq.(8.5), the average brightness is proportional to $1/\sigma^2$, which shows that beam sizes at a crystal location should be small to generate high brightness CR.

TABLE 8.1: X-ray energies generated for a diamond crystal and 43 MeV electrons.

Transition	X-ray energy [keV]
$1 \rightarrow 0$	110
$2 \rightarrow 1$	67.5
$3 \rightarrow 2$	51

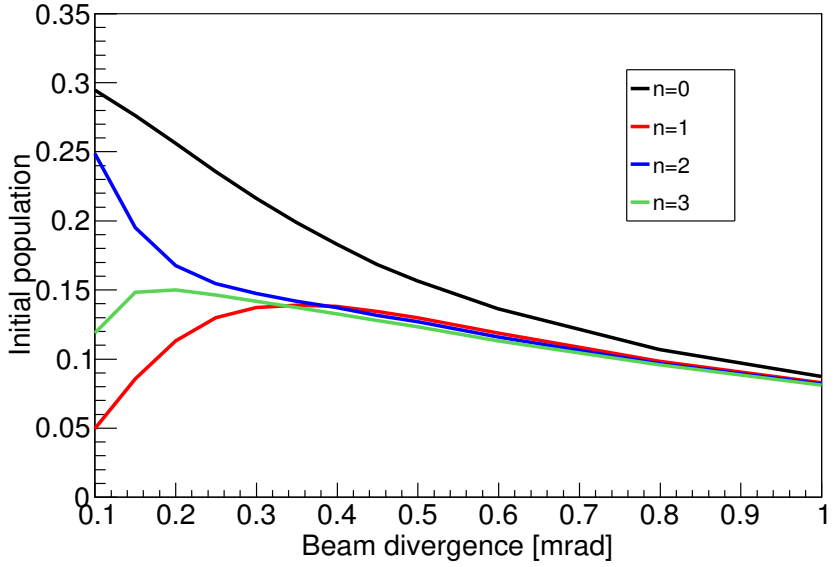

FIGURE 8.1: Initial population depending on beam divergences for different states of n=0, 1, 2, and 3 at incident angle of 0 degree.

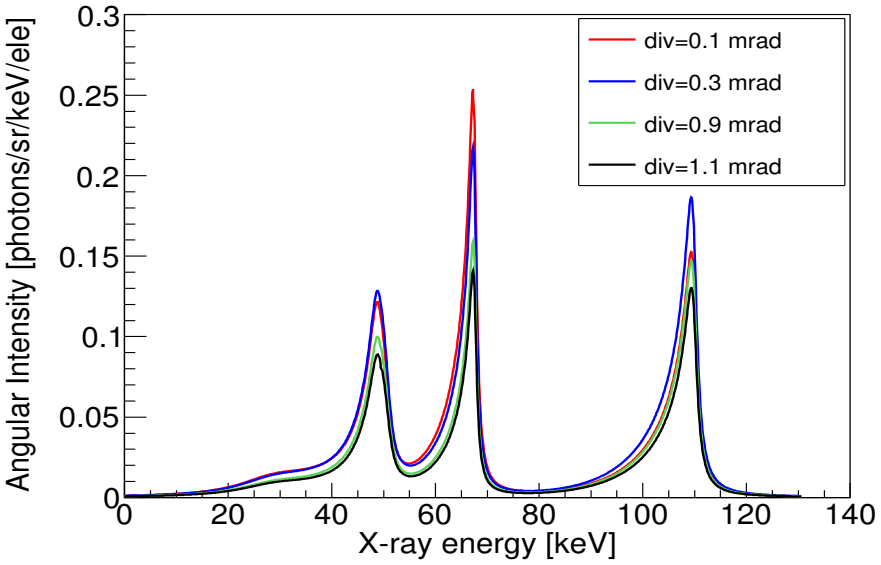

FIGURE 8.2: Photon yields for beam divergences of 0.1, 0.3, 0.9, and 1.1 mrad.

8.1 Beam optics solutions for CR

In this section, we present optics solutions for charges of 1, 20, and 200 pC (1) high brightness solutions with low beam sizes and divergences close to the critical angle (consistent with the beam emittance) and (2) high yield solutions with a large beam size and low divergences at the crystal. Electron beam dynamics from the photocathode to downstream of the second superconducting cavity (8m) was simulated, including space charge effects, using the tracking program ASTRA [103] for bunch charges of 1 pC, 20 pC, and 200 pC. Table 8.2 shows the Twiss parameters, the normalized emittances, and the energy spreads for 1, 20, and 200 pC. The similar low emittance beams were obtained in PITZ (DESY) [50] where the same photocathode and RF gun are employed.

TABLE 8.2: Twiss parameters, normalized emittances, and energy spread for 1, 20, and 200 pC at 8 m from the photocathode, from ASTRA simulations.

Charge [pC]	ϵ [μm-rad]	α_x (=α_y)	β_x (=β_y) [m]	$\Delta E/E$ [%]
1	0.02	-43.3	309.5	0.1
20	0.19	-3.8	21.3	0.1
200	0.52	-3.6	18.9	0.2

8.1.1 Beam optics solutions for high brightness CR

(1) For bunch charges of 1, 20, and 200 pC, the beam optics from downstream of CC2, the second superconducting cavity, to the beam dump was simulated with initial parameters in Table 8.2 using SAD (Strategic Accelerator Design) computer code [104]. Figure 8.3 shows the optics functions obtained by minimizing the beam size at the crystal for bunch charges of 1, 20, and 200 pC. Green and red boxes show quadrupole magnets and bending magnet respectively, and blue and red lines represent the horizontal and vertical planes respectively. The optics matching was done with two sets of triplet magnets; (Q108, Q109, Q110) and (Q118, Q119, Q120). Their polarities are (+, -, +) and (-, +, -); + and - means horizontal and vertical focusing, respectively. The quadrupole magnets used in matching are constrained to a maximum gradient of 6 T/m. Starting with the initial conditions shown in Table 8.2, the minimum beta functions at the crystal are 3 mm, 3 mm, and 5 mm for 1, 20 and 200 pC. Table 8.3 shows the minimum beam sizes, beam divergences, and beta functions at the crystal for three charges. The beta functions (and beam sizes) are largest in the final quadrupole magnets before the crystal, however, the beam sizes are much smaller than the radius of the beam pipe.

The calculated beam sizes ($\sigma_{x,y} = \sqrt{\epsilon_{x,y}\beta_{x,y}}$) for minimum beta functions are quite different from those obtained by particle tracking. The tracking includes chromatic effects. Figure 8.4 shows beam sizes at the crystal as functions of the beta functions for the different charges calculated with both methods. The dots are the beam sizes obtained by particle tracking, and lines are the beam sizes from the analytical calculation. When an electron beam is strongly focused by quadrupole magnets, the focus point is different for different electron energies because a low energy electron is bent more than a high energy electron. As the result of these chromatic aberrations, the transverse beam sizes at the crystal become larger than those obtained by analytical calculation. Assuming sextupole magnets cannot be placed in the chicane to correct the chromaticity, the only other option to keep chromatic effects small is that the electron beams have a sufficiently small energy spread. Figure 8.5 shows the beam sizes at the crystal depending on momentum spread simulated by particle tracking when the beta functions for 20 pC are 3 mm at the crystal. The energy spread affects the horizontal size more due to strong horizontal focus in the last triplet magnet. Also, this shows that momentum spread should be less than 0.1% at the crystal. The energy spread expected for (1, 20) pC is about 0.1% but larger for 200 pC. Therefore, the effect of the chromatic aberration should not be significant for the two lower chargers.

The beam divergences at the crystal for 1, 20 and, 200 pC are 0.3, 0.9, and 1.1 mrad, respectively. For the different charges, 94% (1 pC), 50% (20 pC), and 34% (200 pC) of particles in a bunch satisfy the channeling condition of the critical angle, and the other particles pass through the crystal without channeling. Table 8.4 shows the spectral brilliances at each bunch charge. Although the brilliances decrease at the high charges, the brilliances of 10^{10} [photons/s/mrad^2/mm^2/0.1%bandwidth] can be obtained.

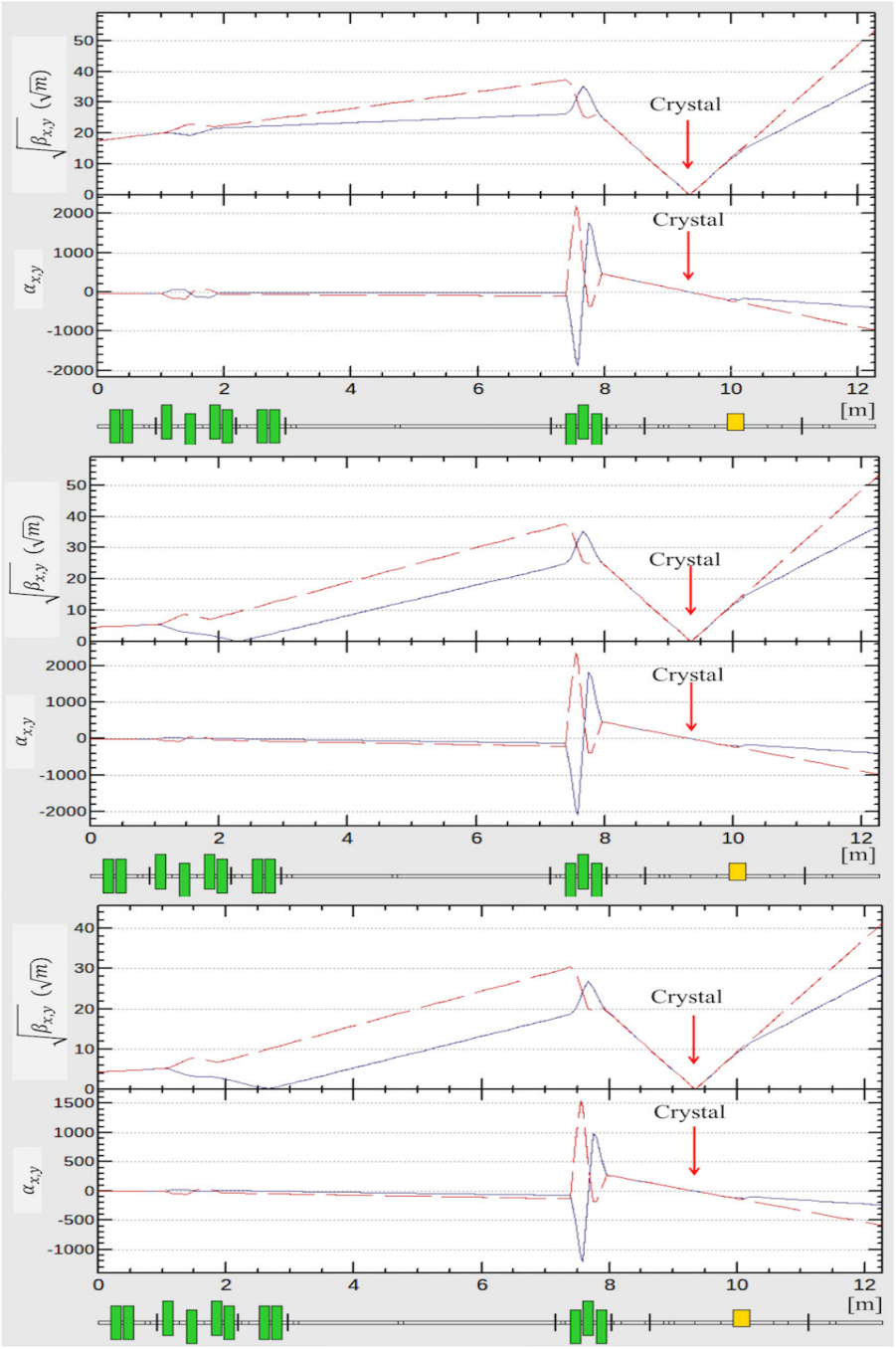

FIGURE 8.3: Optics functions of the transport line when beam sizes at crystal are minimum for 1 pC, 20 pC, and 200 pC. Top: 1 pC, Middle: 20 pC, Bottom: 200 pC. Blue and red lines show the horizontal and vertical planes. Green and yellow boxes represent quadrupole and dipole magnets respectively.

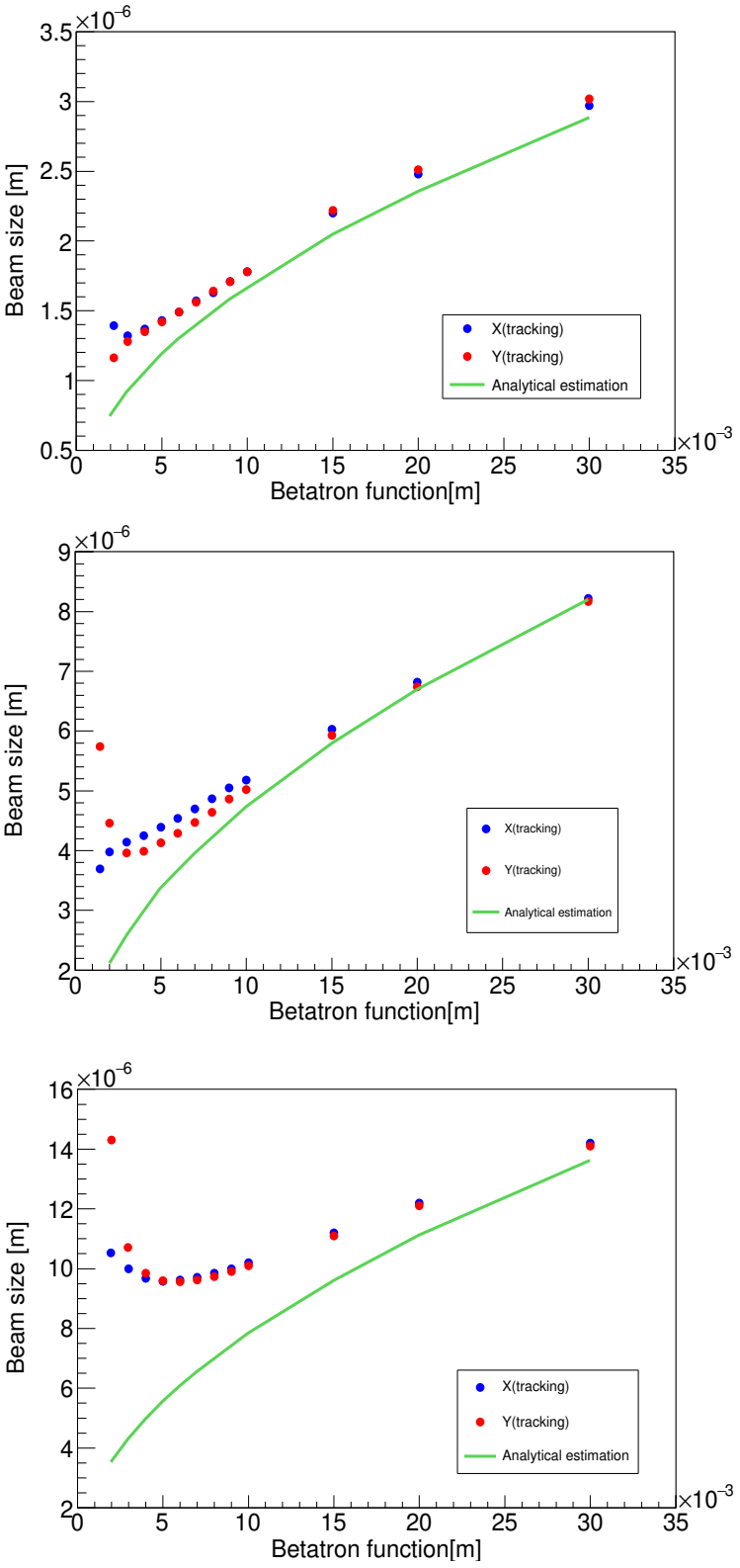

FIGURE 8.4: Beam sizes at the crystal depending on the beta functions for 1 pC, 20 pC, and 200 pC. Top: 1 pC, Middle: 20 pC, Bottom: 200 pC. Blue and red dots show horizontal and vertical beam sizes obtained from particle tracking. Green lines are the beam sizes from analytical calculation without chromatic effects. The rms energy spreads for these bunch charges are shown in Table 8.2.

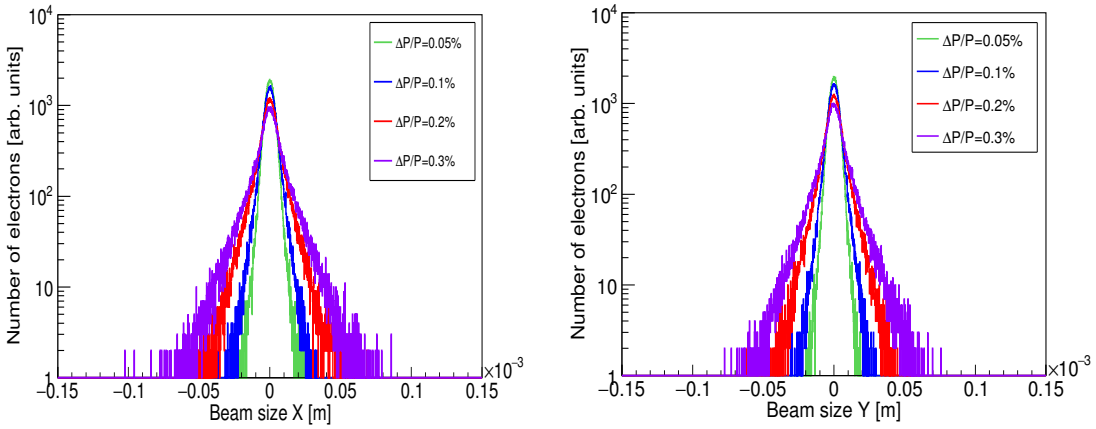

FIGURE 8.5: Beam size distributions at the crystal for different momentum spreads for 20 pC when the beta functions at the crystal are 3 mm. Left: horizontal plane, right: vertical plane.

TABLE 8.3: Minimum beam sizes, beam divergences, and beta functions at the crystal for the different charges. Initial conditions are shown in Table 8.2.

Charge [pC]	β_x $(=\beta_y)$ [mm]	σ_x, σ_y [μm]	σ'_x, σ'_y [mrad]
1	3	(1.3, 1.3)	(0.3, 0.3)
20	3	(4.1, 4.0)	(0.9, 0.9)
200	5	(9.6, 9.6)	(1.1, 1.1)

TABLE 8.4: Spectral brilliances at each bunch charge for high brightness solutions. The brilliance unit is [photons/s/mrad^2/mm^2/0.1%bandwidth].

	Brilliance		
Charge [pC]	50 keV	70 keV	110 keV
1	3.3×10^{11}	7.4×10^{11}	1.0×10^{12}
20	5.6×10^{10}	1.2×10^{11}	1.9×10^{11}
200	6.7×10^{10}	1.4×10^{11}	2.2×10^{11}

TABLE 8.5: Photon fluxes at each bunch charge for high brightness solutions.

	Photon flux [photons/s]		
Charge [pC]	50 keV	70 keV	110 keV
1	2.4×10^{5}	5.4×10^{5}	7.6×10^{5}
20	3.7×10^{6}	8.0×10^{6}	1.2×10^{7}
200	3.3×10^{7}	7.0×10^{7}	1.1×10^{8}

8.1.2 Beam optics solutions for high yield CR

(2) To produce high yield CR, the beam divergence at the crystal should be much smaller than the critical angle from Eq. (8.3) and (8.4) as mentioned before. This means that beam size at the crystal will be large due to the conservation of beam emittance. Hence the chromatic aberration can be ignored (see Fig. 8.4). We simulated the beam optics so that the electron beam has divergences of 0.1 mrad and there is an optics waist (twiss parameter $\alpha_{x,y} = 0$) at the crystal for each charge. The optics functions along the beamline are shown in Figure 8.6. The beam optics simulated for each charge is different due to different initial twiss parameters but shows the same behavior. For charges of 1 pC, 20 pC, and 200 pC, the beam sizes at the crystal are 2.9 μm, 22 μm, and 61 μm, respectively. Table 8.6 shows beam sizes and beta functions for a beam divergence of 0.1 mrad at the crystal. The beam sizes obtained from the analytical calculation of the betatron beam size without chromatic effects are consistent with those from particle tracking. Using the nominal machine parameters mentioned in Table 3.1, the photon fluxes at a beam divergence of 0.1 mrad are calculated, and the results shown in Table 8.7. The photon flux of about 10^8 photons/s at 110 keV is obtained at 200 pC. When a bunch charge of 1 nC and a bunch frequency of 5 MHz are used, the photon flux of 10^9 photons/s can be achieved.

TABLE 8.6: Beam sizes and beta functions for a beam divergence of 0.1 mrad at the crystal.

Charge [pC]	β_x (=β_y) [m]	σ_x=σ_y [μm]
1	0.03	29
20	0.22	22
200	0.61	61

TABLE 8.7: Photon fluxes at each bunch charge for a beam divergence of 0.1 mrad at the crystal.

	Photon flux [photons/s]		
Charge [pC]	50 keV	70 keV	110 keV
1	2.2×10^5	6.4×10^5	6.2×10^5
20	4.4×10^6	1.3×10^7	1.2×10^7
200	4.4×10^7	1.3×10^8	1.2×10^8

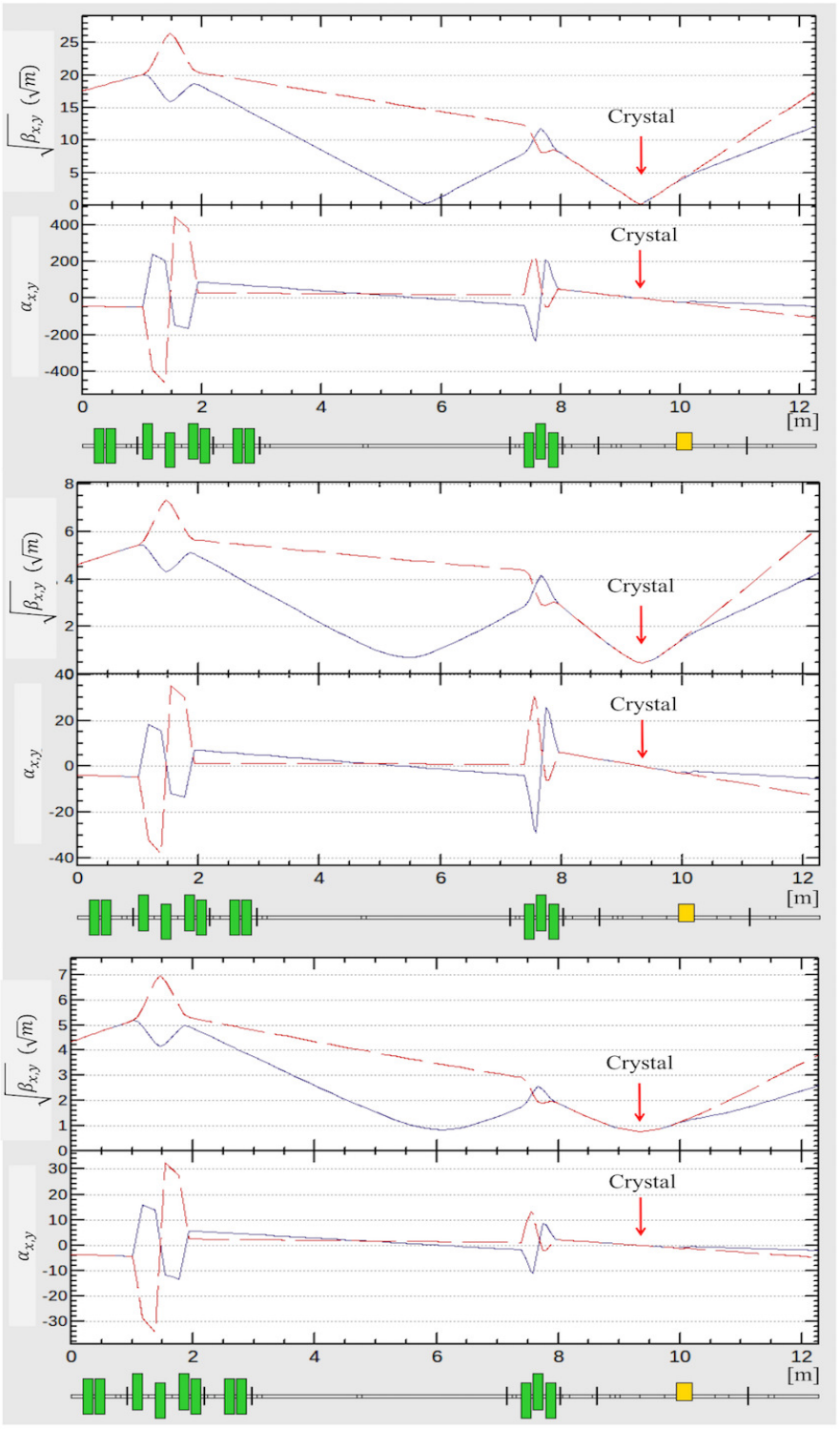

FIGURE 8.6: Beam optics for the high yield solution along the transport line from the last cavity to the beam dump. The beam divergences at the crystal are matched to 0.1 mrad in each case. Top: 1 pC, Middle: 20 pC and Bottom: 200 pC. Blue and red lines show the horizontal and vertical planes. Green and yellow boxes represent quadrupole and dipole magnets respectively.

8.2 Beam optics solutions with misalignment and magnetic field error

In this section, we discuss error corrections of quadrupole magnets with misalignments and magnetic field errors. These magnets with misalignments and magnetic errors, give the beam dipolar and quadrupolar kicks with different strengths, and cause different focusing, beam deflections and excitations of betatron oscillations and unwanted dispersions. Therefore, beam optics must be simulated including these effects. In the FAST linac, corrector magnets such as steering magnets and skew magnets for corrections of the errors have been installed.

Misalignments and magnetic errors, assuming that they follow a Gaussian random distribution with a cutoff of 3σ, are set in all quadrupole magnets, and the optics calculations are done with 10 different error seeds. The RMS values of misalignments and gradient errors set in the quadrupole magnets are shown in Table 8.8. We assume that the rms errors are as follows: alignment: 0.2 mm, gradient: 0.3%, and rotation: 0.2 mrad in each plane. The orbits are corrected with 7 steering magnets and 11 BPMs. Figure 8.7 shows the central orbits for the high brightness optics and the high yield divergence optics with and without orbit corrections for a charge of 200 pC. Green lines show the central orbit without the correction. When the orbits are not corrected with the steering magnets, the horizontal orbit error is over 3 mm in the second triplet where beam sizes are maximum and the vertical orbit error is about 2 mm at the crystal.

Figure 8.8 shows the central orbits of electron beams for the high brightness optics and the high yield optics along the beamline after the orbit correction. Blue and red lines are the average orbits of horizontal and vertical, respectively. The error bars are the standard deviations of orbits. After the orbit correction, the deviations of the two solutions from a central orbit at the crystal can be reduced to about ± 0.2 mm for 200 pC. Table 8.9 shows beam sizes and beta functions achieved at the crystal for the high brightness optics using quadrupole magnets with errors. The beam sizes at the crystal for 200 pC are about 11 μm.

TABLE 8.8: Alignment and field errors for the quadrupole magnets.

Alignment error		Gradient error	Rotation error
ΔX [mm]	ΔY [mm]	ΔK/K	$\Delta\theta$ [mrad]
0.2	0.2	0.003	0.2

TABLE 8.9: Beam sizes and beta functions at the crystal achieved for the high brightness optics using the quadrupole magnets with the misalignments and field errors.

Charge [pC]	β_x (=β_y) [m]	σ_x, σ_y [μm]
1	5	(1.8±0.4, 1.7±0.3)
20	6	(5.2±0.8, 5.0±0.8)
200	8	(10.5±0.9, 10.3±0.8)

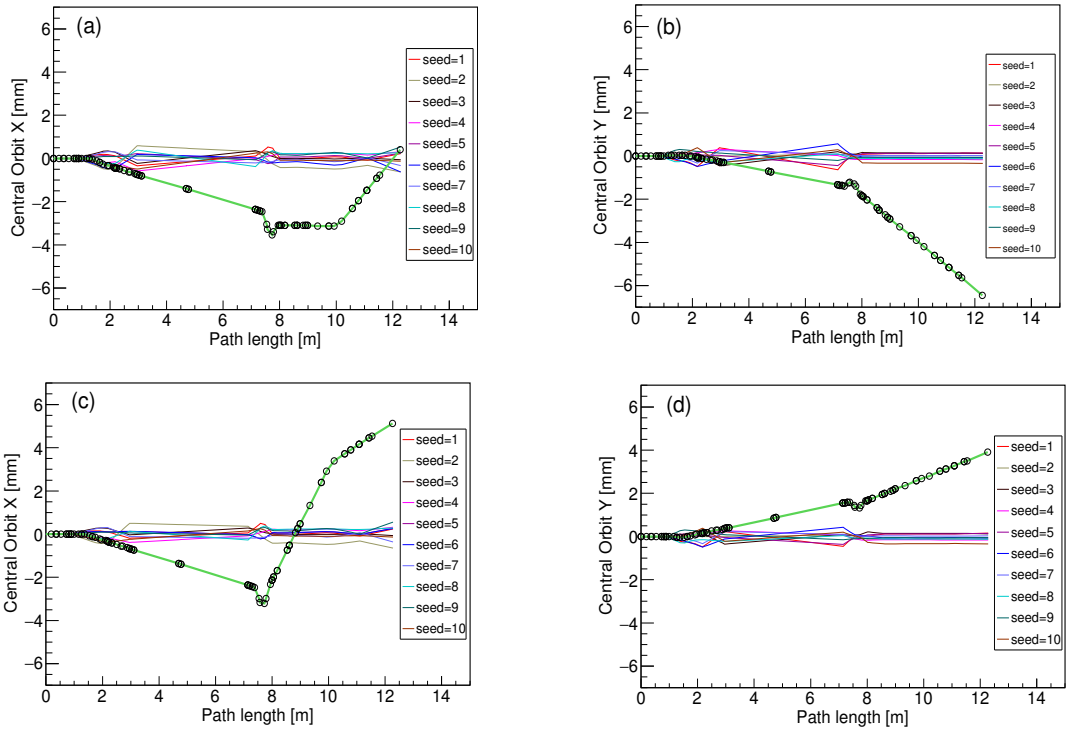

FIGURE 8.7: Orbit corrections with steering magnets for the high brightness optics (upper plots (a) and (b)) and the high yield optics (bottom plots (c) and (d)) for 200 pC. Left: horizontal, Right: vertical. Green lines show before corrections. 10 seeds are used.

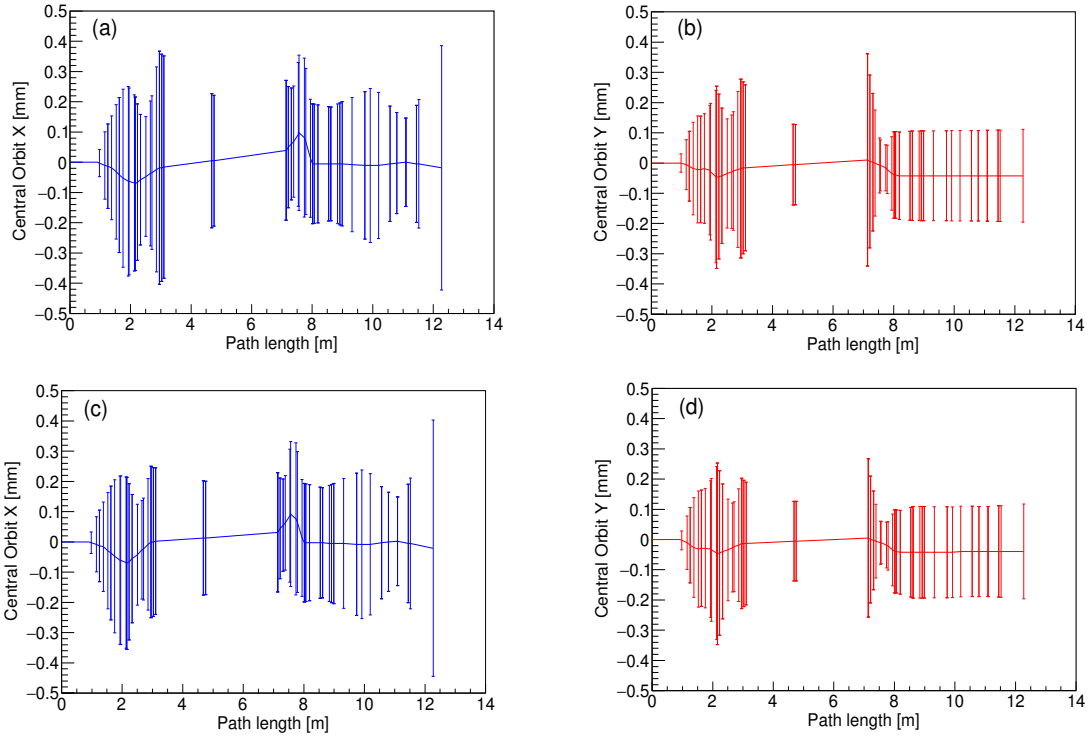

FIGURE 8.8: Transverse central orbit along the beamline for the high brightness optics (upper plots (a) and (b)) and the yield optics (bottom plots (c) and (d)) after the orbit correction for 200 pC. 10 seeds are used. Blue and red lines show average orbits in the horizontal and vertical planes, and black lines show the standard deviations for 10 seeds.

8.3 Background from bremsstrahlung

Bremsstrahlung (BS) X-rays are produced when relativistic electrons passing through a crystal are scattered by the atomic nuclei. The spectrum of BS is continuous, covering a wide energy range from microwave to hard X-rays. The maximum BS energy can extend to nearly the electron energy. BS is generally background in CR experiments since it is emitted in the same forward direction as CR with respect to the incident electron beam. In order to examine the effect of BS in our CR experiment, we estimated the photon count and the energy distribution of the background registered in the detector with GEANT4 [72] simulations. The X-ray detector with an aperture of 3×3 mm^2 is assumed to be located at 1.5 m from the target crystal so that the detector's acceptance is 2 mrad. The layout showing the X-ray detector and simulation geometry is shown in Figure 8.9. In the simulations, 10^8 particles (20 pC/bunch) with an energy of 43 MeV and a diamond crystal with a thickness of 168 μm are used. The number of particles is chosen considering the run time in GEANT4.

Figure 8.10 shows the scattering angles of photons emitted from electron beams going through the diamond crystal in the forward direction and in the detector. The left plot in Fig. 8.10 shows the angular distribution in the forward direction, while the right plot shows the angular distribution in the detector, and the red line shows the Gaussian fit. The standard deviation of the angular distribution of photons emitted in the forward direction is about 49 mrad, while the rms beam size obtained from the Gaussian fit is 1σ = 13 mrad, which is good agreement with the BS scattering angle $1/\gamma$ = 12 mrad. This shows that the angular distribution of all the scattered BS photons is very non-Gaussian, but the distribution within the detector's acceptance is nearly uniform.

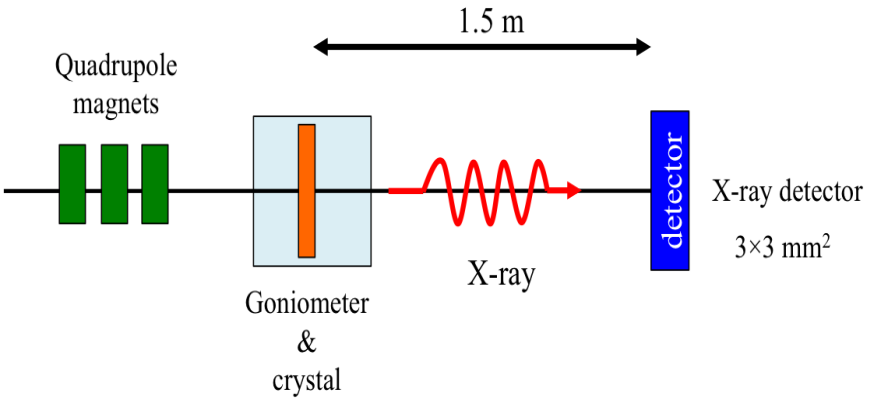

FIGURE 8.9: Layout showing goniometer and the detector.

From Fig. 8.10, about 10^6 photons (or about 10^{-2} photons/electron) are emitted in the forward direction, and $\sim 10^4$ photons of them go into the detector. Also, the photon count hitting the detector as a function of beam size for different beam divergences at the crystal is plotted in Figure 8.11. For the electron beam size below 0.1 mm at the crystal, the number of photons going into the detector is substantially constant at $\sim 10^4$ particles. However, it decreases when the electron beam size is over 0.1 mm. The photon beam size σ_2 at the X-ray detector can be written as

$$\sigma_2 = \sqrt{\sigma_1^2 + L^2 \sigma_1'^2}, \tag{8.6}$$

where σ_1 is the photon beam size, σ_1' (=13 mrad) is the photon beam divergence at the diamond crystal, and L (=1.5 m) is the distance between the crystal and the X-ray detector. The number of photons per beam area at the X-ray detector location is proportional to $\frac{1}{\pi\sigma_2^2} = (1/\pi(\sigma_1^2 + L^2\sigma_1'^2))^2$. Therefore, the photon count I going into the X-ray detector with the detector area S(=9 mm^2) is

$$I \propto \frac{S}{\pi\sigma_2^2} = \frac{S}{\pi(\sigma_1^2 + L^2\sigma_1'^2)}. \tag{8.7}$$

This photon count I is shown as a function of the beam size at the crystal in the right plot in Figure 8.12. The number of photons hitting the detector decreases for the beam size σ_1 of over 0.1 mm, which is consistent with simulation results with GEANT4 shown in the left plot in Figure 8.12. In our CR experiment for an electron bunch charge of 20 pC, we expect about 10^4 background BS photons per electron bunch will be registered in the detector, since the beam size at the crystal is desired to be below 0.1 mm. Also, the ratio of background photons in the detector to incident electrons is approximately 10^{-4}, therefore, about 5×10^2 and 10^5 photons per bunch for bunch charges of 1 pC and 200 pC respectively will be registered as background. Table 8.10 shows the expected number of background photons registered in the detector.

TABLE 8.10: The number of background photons registered in the detector for three charges.

Charge [pC]	Number of photons
1	$\sim 5\times10^2$
20	$\sim 10^4$
200	$\sim 10^5$

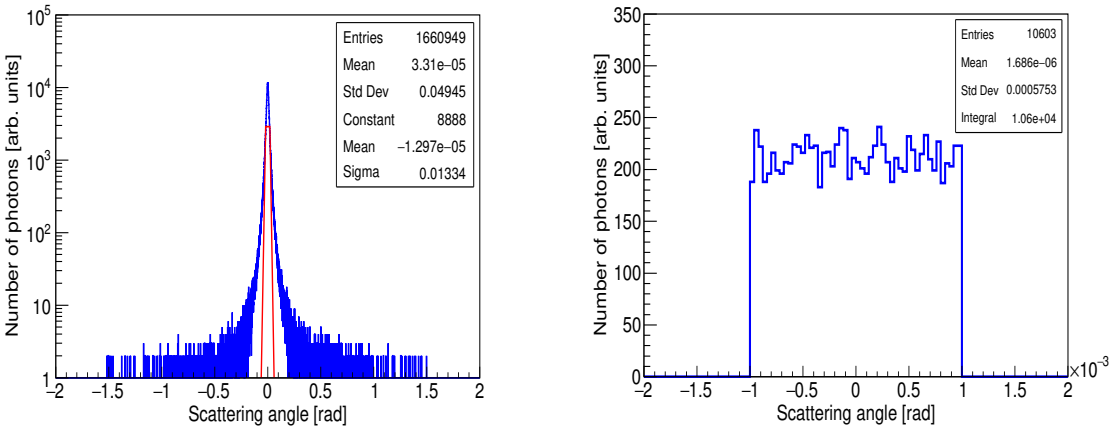

FIGURE 8.10: Angular distributions of photons emitted in the forward direction and in the detector with an acceptance of 2 mrad. Left: the angular distribution in the forward direction. Right: the angular distribution in the detector.

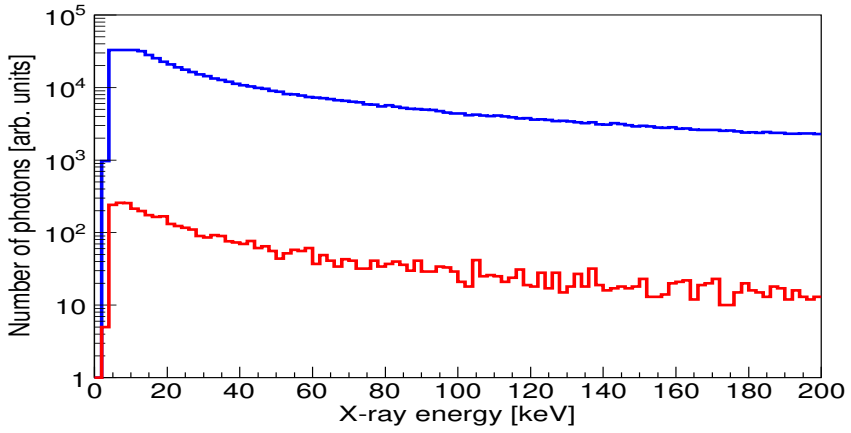

FIGURE 8.11: Bremsstrahlung spectra in the forward direction (blue) and in the detector (red).

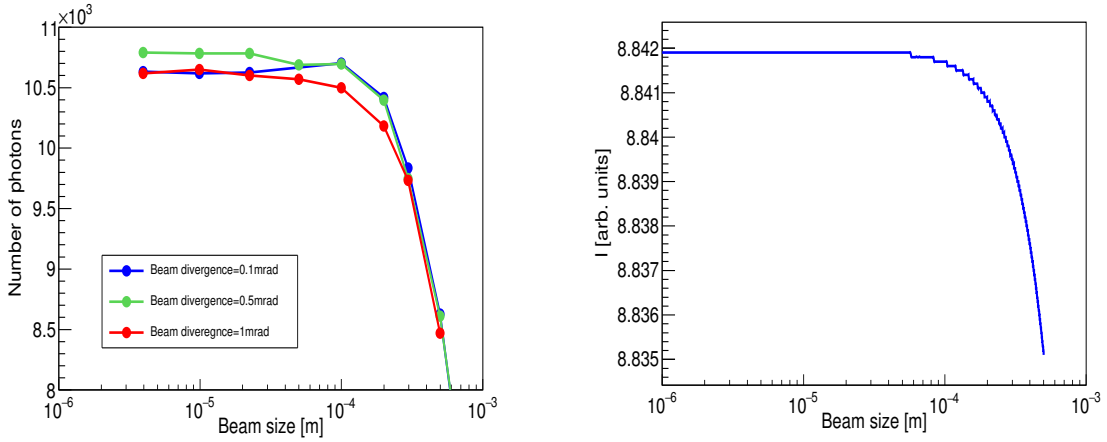

FIGURE 8.12: Number of photons hitting the detector depending on beam divergences and beam sizes of incident electrons. Left plot is simulation results with GEANT4 and right plot is analytical calculation with Eq. (8.7)

The BS energy distributions in the forward direction and in the detector are shown in Figure 8.11. The energy distributions for the two cases have the almost same behavior, which indicates that the BS photon energy does not depend on its emitted angle. Moreover, in order to investigate the dependence of the BS energy distributions on electron energies, we simulated them with electron energies of 43 MeV, 60 MeV, 80 MeV, and 100 MeV using GEANT4. The number of photons and the energy spectra in the forward direction are shown in Table 8.11 and Figure 8.13, respectively. The photon distributions are shown to the maximum of 200 keV (left plot) and 100 MeV (right plot). The left plot shows that the maximum yield occurs close to 10 keV for all the electron energies and the distribution from about 40 keV to 200 keV is nearly the same for the different electron energies. The right plot shows that the photon spectra extend to the electron beam energy in all cases. Table 8.11 shows that the total number of BS photons produced in the forward direction is unchanged for different electron energies, because the differential cross section χ of BS can be approximately written as [105]

$$\frac{\partial\chi}{\partial(\hbar\omega)} \simeq \frac{16}{3}\alpha r_e Z^2 \ln\left(\frac{233}{Z^{1/3}}\right), \tag{8.8}$$

where α is the fine-structure, r_e is the classical electron radius, and Z is the atomic number of the crystal. This shows that the photon yield, obtained by integrating over all photon energies, is independent of the electron energy.

The expected channeling spectra, including the background, when a 43 MeV electron beam is incident on a 168 μm thick diamond crystal parallel to the (110) planes, are shown in Figure 8.14. The CR yields without the background are calculated with Eq. (8.3), and then the process of de-channeling and re-channeling in a crystal are taken into account. This model affects populations in bound states and leads to reduce photon yields. The CR photon count including this process can be calculated using a free parameter n_f. The appropriate n_f was decided from photon yields obtained in CR experiments at the ELBE facility [34]. The "CR_high" label in Fig. 8.13 corresponds to the result for a case without dechanneling $n_f = 21$, "CR_mid" is the result for the case $n_f = 17$ estimated from the experimental values, and "CR_low" is a more conservative result with $n_f = 13$ corresponding to a lower yield. The X-rays with discrete energies of 110 keV (transition: 1→0), 67.5 keV (transition: 2→1) and 51 keV (transition: 3→2) are generated at the angle of 0 degree. The ratios of CR signal for CR_mid ($n_f = 17$) to the BS background are about 8 at 110 keV, 7 at 67.5 keV, and 4 at 51 keV. These theoretical values of signals to backgrounds imply that the CR signal should be clearly observable at the higher energy CR spectral lines.

TABLE 8.11: Number of photons generated in the forward direction for different electron energies of 43 MeV, 60 MeV, 80MeV, and 100 MeV. Ratio means Number of photons/Number of photons at 43 MeV

Electron energy [MeV]	Number of photons	Ratio
43	1,660,949	1.00
60	1,711,277	1.03
80	1,745,297	1.05
100	1,764,527	1.06

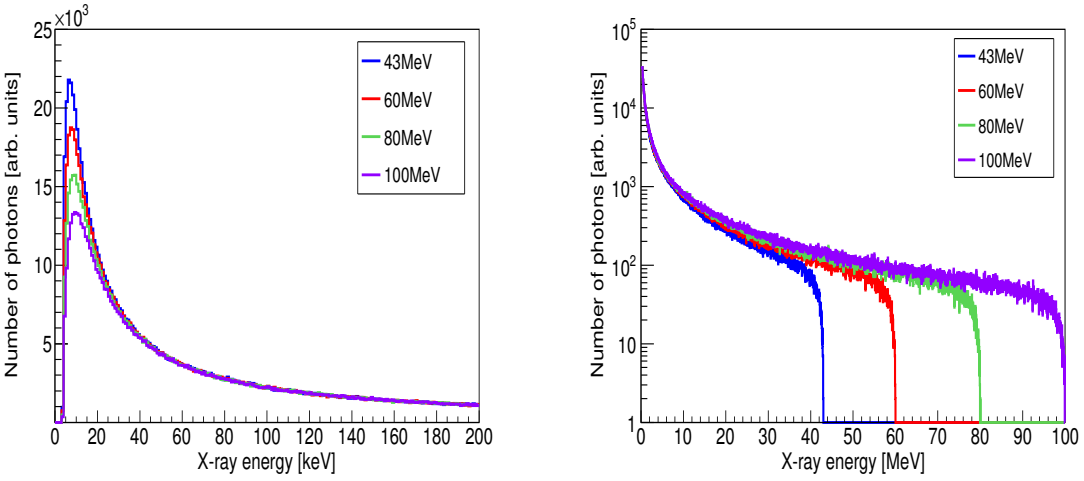

FIGURE 8.13: Bremsstrahlung spectra for different electron energies of 43 MeV, 60 MeV, 80 MeV, and 100 MeV. Left: the energy spectra for 0-200 keV. Right: the energy spectra for 0-100MeV.

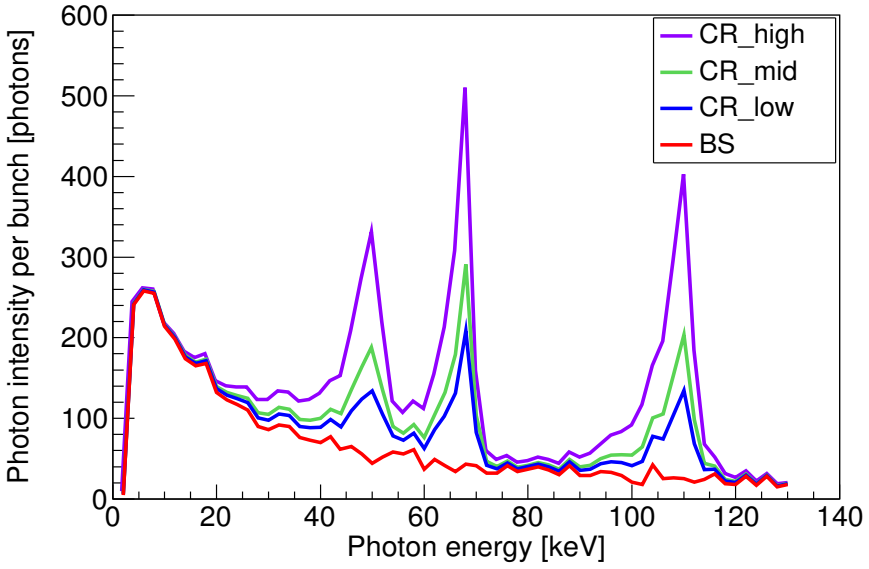

FIGURE 8.14: The expected X-ray spectrum including the background for difference estimates of the CR photon number.

8.4 Electron beam distributions after crystal

This section describes electron beam sizes and beam divergences after the electron beam passes through the diamond crystal with and without channeling. This beam experiences multiple scattering events with atomic nuclei, and the beam divergence grows after passing through the crystal. Therefore, the electron beam emittance increases, which could cause particles loss from scraping at the beam pipe. The multiple scattering depends on whether the beam is channeled or not in the crystal. The rms scattering angle θ for an electron that is not channeled depends on the crystal thickness L, its atomic number Z, its mass number A, and the electron momentum p, as [106, 107]

$$\theta = \frac{13.6[\text{MeV}]}{\beta cp}\sqrt{\frac{L}{L_{rad}}}\left[1 + 0.038\ln(\frac{L}{L_{rad}})\right], \tag{8.9}$$

$$L_{rad} = \frac{716.4[\text{g/cm}^2]\cdot A}{Z(Z+1)\ln(287/\sqrt{Z})}, \tag{8.10}$$

where βc is the velocity of the electrons, L_{rad} the radiation length of the crystal. The rms scattering angle after an electron of 43 MeV passes through a 168 μm thick diamond crystal can be computed to be about 8.3 mrad. However, the beam divergence for a channeled electron has been shown to be about 0.2 - 0.6 times smaller than that obtained from Eq. (8.9) [34, 108]. Using recently added modules in GEANT4 [72, 109], we estimated the scattering angles and energy spreads of the electron beam passing through the crystal under both channeling and non-channeling conditions.

The angular scattering of the electron after the crystal calculated using GEANT4 is shown in Figure 8.15. The initial beam divergence at the crystal is set to be 0.1 mrad, and 10^5 electrons are used in both cases. The left plot in Fig. 8.15 shows the angular distribution of electrons at the crystal entrance and the right plot shows the distribution after the crystal with and without channeling. The standard deviation of the entire distribution (including the tails) without channeling is about 10.1 mrad, about 100 times larger than that before the crystal. On the other hand, the standard deviation of the distribution after channeling is 7.7 mrad, or approximately 0.8 times the value without channeling. The beam divergence after the electron beam is channeled in the crystal become smaller than that after without channeling. Figure 8.16 shows the beam sizes of electrons at a monitor in front of the detector, after with and without channeling in the crystal. The beam monitor is assumed to be at 1.5 m from the crystal. Without channeling in the crystal, the beam sizes at the monitor are (X, Y) = (15.4 mm, 15.2 mm) while with channeling, they decrease to (11.3 mm, 11.1 mm). There is a small shift in the horizontal position of the centroid with and without channeling, but this could be an artifact of the relatively small number of particles used in the simulation.

When relativistic electrons pass through the crystal, the energy loss is caused by the ionization loss and radiation loss (bremsstrahlung). The critical energy E_c when the two energy losses are equal is written as [106]

$$E_c\,[\mathrm{MeV}] = \frac{610\,[\mathrm{MeV}]}{Z + 1.24}, \tag{8.11}$$

where Z is the atomic number of the crystal. This equation means that the ionization loss is dominant for an electron beam with energy below the critical energy. The critical energy E_c for a diamond crystal of $Z = 6$ is 84 MeV, which means that the ionization loss contributes strongly to the electron energy loss in our CR experiment with a 43 MeV electron beam. The ionization loss can be analytically calculated by the Bethe-Bloch equation [106]

$$-\frac{dE}{dx} = 0.1535\,[\mathrm{MeV/gcm^2}]\frac{Z}{A}\frac{\rho}{\beta^2}\left[\frac{1}{2}\ln\left(\frac{2m_e c^2\beta^2\gamma^2 T_{max}}{I^2}\right) - \beta^2 - \frac{\delta(\beta\gamma)}{2}\right], \tag{8.12}$$

$$T_{max} = \frac{2m_e c^2\beta^2\gamma^2}{1 + 2\gamma m_e/M + (m_e/M)^2}, \tag{8.13}$$

$$I = 16Z^{0.9}\,[\mathrm{eV}], \tag{8.14}$$

where ρ the crystal density, βc the velocity of an electron beam, Z atomic number, A atomic mass, m_e electron rest mass, I the excitation potential, and δ density effect correction. An experimental energy loss for a thin crystal would be smaller than that calculated by Eq. (8.12), because the Bethe-Bloch equation describes the mean energy loss and the energy loss obtained from experiments follows the Landau distribution [106]. Using Eq. (8.12), the mean energy loss for an electron beam of 43 MeV and a 168 μm thick diamond crystal can be computed to be about 100 keV, about 0.2% of the initial electron energy. Figure 8.17 shows the electron energy distributions after channeling and without channeling calculated with GEANT4. The green curve in Fig. 8.17 is the initial energy distribution of electrons with an energy spread of 0.1%, the blue curve is the energy distribution after the crystal without channeling, and the red curve is after channeling. For the case without channeling, the energy distribution has a peak at 42.9 MeV and the energy loss is about 100 keV. On the other hand, for the case with channeling, the peak is at 42.95 MeV and the energy loss is about 50 keV.

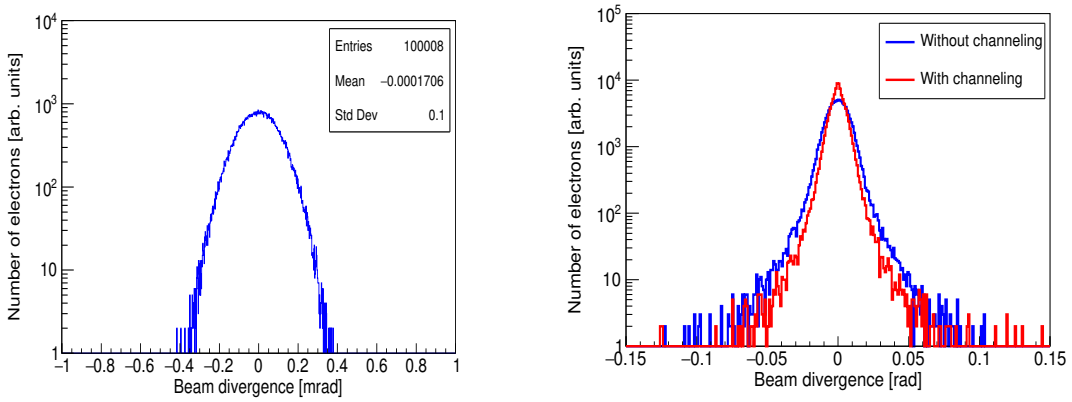

FIGURE 8.15: Angular distributions of a 43 MeV electron beam before and after going through the diamond crystal with the thickness of 168 μm. Left plot [mrad scale]: the distribution at the crystal entrance. Right plot [rad scale]: the beam distribution with and without channeling. Standard deviations with and without channeling are 7.7 mrad and 10.1 mrad, respectively.

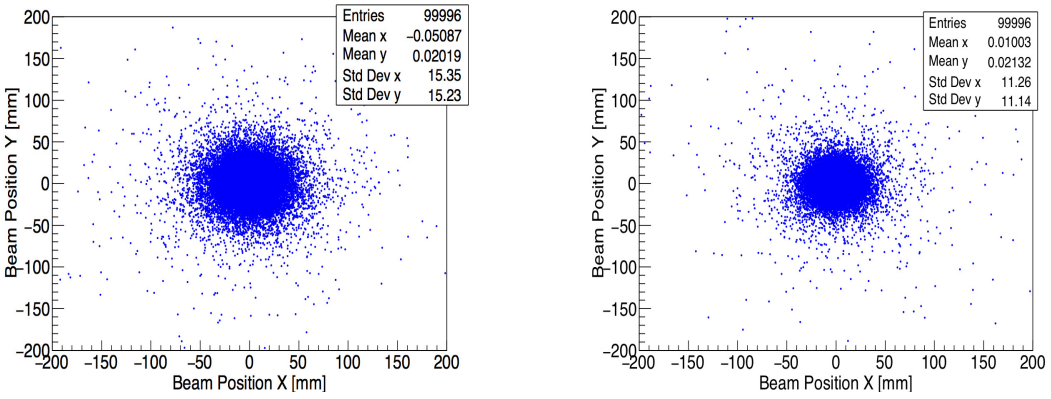

FIGURE 8.16: Beam positions and sizes (x, y) after the non-channeled (left) and the channeled (right) electron beam in the diamond crystal.

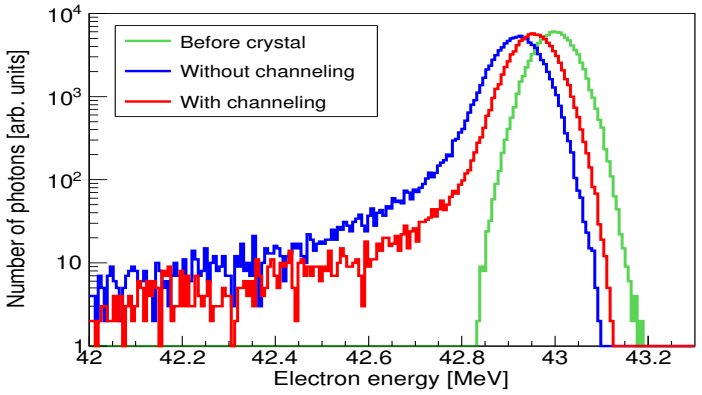

FIGURE 8.17: Energy distributions of the electron beam before and after the diamond crystal. The green curve shows the initial energy distribution. The red and blue curves are the distribution with channeling and without channeling, respectively.

8.5 Compton scattering for X-ray detector

The experimental layout in Fig. 3.2 shows an X-ray detector downstream of the crystal. This configuration will be used at low bunch charges when the photon rate emitted into the detector's acceptance is about 1 photon per bunch. At higher bunch charge and the nominal laser frequency of 3 MHz, the photon rate will be high enough to cause photon pile-up in this detector. Two or more photons arriving within the detector's response time (about 25 μs) will be registered as a single photon with an energy which is the sum of all the photon energies leading to a wrong spectrum. In this section, we discuss the use of a second X-ray detector placed orthogonal to the beamline which will detect photons Compton scattered from a plastic plate in order to avoid this pile-up effect.

In our experiment, with a laser pulse repetition rate of 3 MHz, and for 1 pC/bunch, the number of electrons going into the diamond crystal per second can be computed using Table 8.10

$$500\,[\text{photons}] \times 3 \times 10^{6}\,[\text{Hz}] \times 10^{-3}\,[\text{s}] \times 5\,[\text{Hz}] = 7.5 \times 10^{6}\,[\text{photons/s}], \tag{8.15}$$

Table 8.12 shows the expected photon counts per second hitting the detector for each charge. This estimate considers only the BS background, which indicates that the pile-up will be caused even when a bunch charge of 1 pC is used.

For the pile-up rejection, it is important to reduce the photon flux going into a detector. Commonly, for low photon energies, the number of photons hitting a detector can be reduced using an attenuator such as Al and Brass, and we can extract the true photon rate by calculating the number of photons absorbed into the attenuator with the absorption data which is supplied by NIST [110]. By contrast, for high photon energies, using attenuators is not effective due to a low absorption cross sections at high energies. This will be true in our experiment with expected CR photon energies ranging from 50 keV to 110 keV. Thus, we will utilize Compton scattering that can significantly reduce the photon rate for high photon energies [22, 36].

Compton scattering results from the interaction of a photon with free electrons in a material substance. The scattered photons experience energy loss, resulting in shifts to longer wavelength. The differential cross section for the Compton scattering is given by the Klein-Nishina formula:

$$\frac{d\sigma}{d\Omega} = \frac{r_e^2}{2}\frac{1}{[1+hv_0[1-\cos\theta]]^2}\left(1+\cos^2\theta+\frac{(hv_0)^2(1-\cos\theta)^2}{1+hv_0(1-\cos\theta)}\right), \tag{8.16}$$

$$hv = \frac{hv_0}{1+\left(\frac{hv_0}{m_e c^2}\right)(1-\cos\theta)}, \tag{8.17}$$

where r_e is the classical radius of the electron, $h\nu_0$, $h\nu$ are the energies of the incident and scattered photons respectively, and θ is the scattering angle. In order to know the relation of a photon's cross-section, scattering angle, and final energy, the differential cross section and photon energy as a function of scattering angle for incident photon energies of 50 keV, 70 keV, and 110 keV are plotted in Figure 8.18 using Eq. (8.16) and (8.17). Most photons are scattered in the forward and backward direction to the incident photons. Since the differential cross section has a minimum at 90 degrees, the detector should be placed orthogonal to the beamline (incident photons). Figure 8.19 shows the layout of the second X-ray detector. X-ray energies of 110 keV, 70 keV, and 50 keV scattered at 90 degrees have their energies shifted to 90 keV, 60 keV, and 45 keV, respectively, because the photons lose energy to the scattering electrons.

TABLE 8.12: The number of background photons per second registered in the detector for three charges.

Charge [pC]	Photons/s
1	7.5×10^6
20	1.5×10^8
200	1.5×10^9

Figure 8.20 shows the three major types of photon interactions with matter [111]. Since photons with energies of 110, 70, and 50 keV are expected in our CR experiment, the target material should have an atomic number below 30 owing to the dominance of Compton scattering in this energy range. In order to select appropriate materials to use in our experiment, we have tried diamond, Al, Si, PMMA, and PVC plates, each with a thickness of 2 mm. Photon counts in the X-ray detector were simulated using GEANT4. As an initial condition, 10^9 photons with an energy of 70 keV and an energy spread of 10% were used. The detector with the aperture of 3×3 mm^2 is assumed to be located at

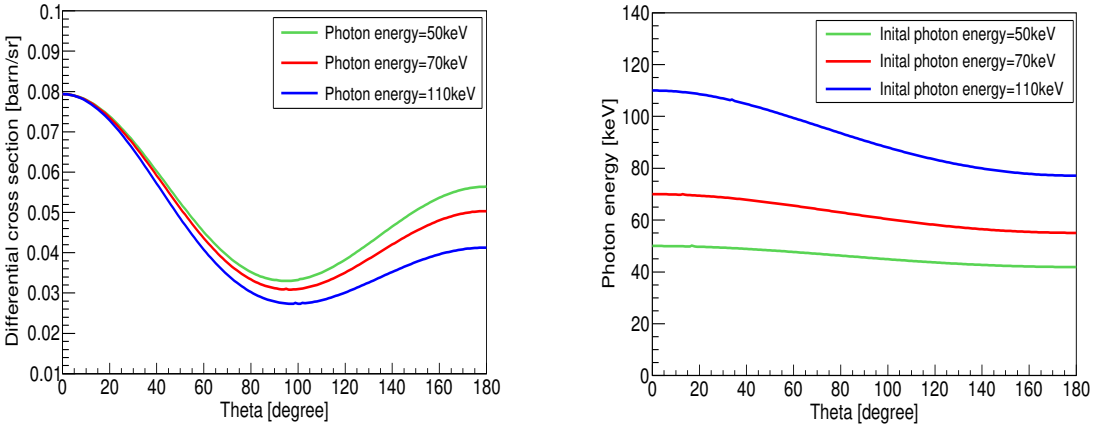

FIGURE 8.18: Differential cross-section (upper) and photon energy (lower) depending on scattering angle.

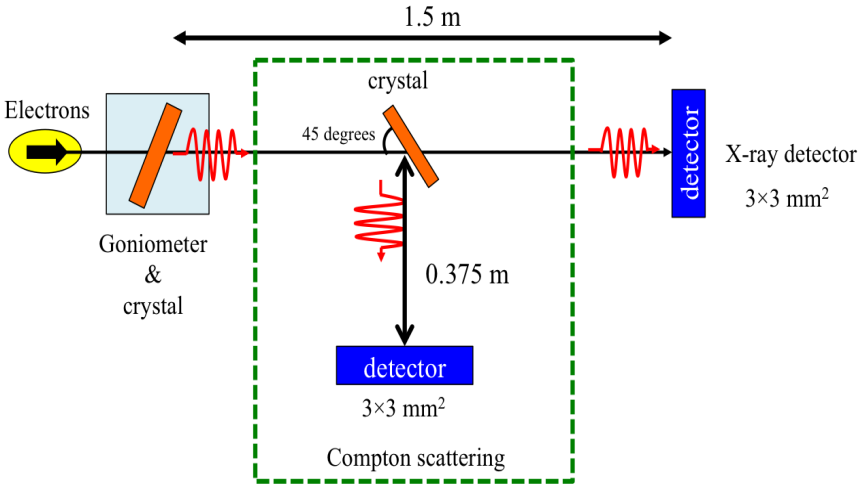

FIGURE 8.19: Layout of the detector.

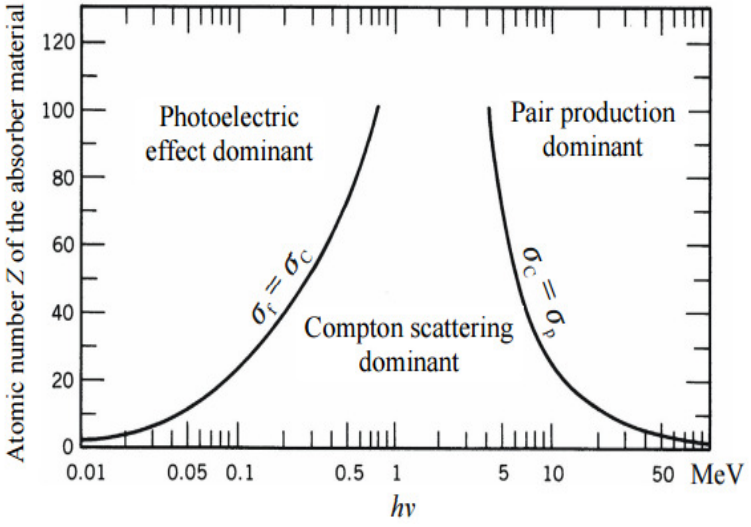

FIGURE 8.20: Three major types of photon interaction with matter [111]. The curves demarcate the regions where each effect is dominant.

0.375 m from the Compton scattering plate, see Fig. 8.19. Figure 8.21 shows the number of Compton scattered photons and their energies hitting the detector for the different materials. In GEAN4 simulations, Rayleigh scattering is ignored due to the high incident photon energies (>50 keV). Photons with energies of 60 keV and energy spreads of 10% are scattered in the detector; the simulated energies agree with the analytical calculation with Eq. (8.17). The Compton scattered photon count decreases with an increase of the atomic number Z due to the absorption within the material. Also, materials of high atomic number produce electrons by the photoelectric effect. For the organic materials, the number of photons in the detector decreases by seven orders of magnitude, therefore, we decided to use PVC or PMMA as the material for Compton scattering.

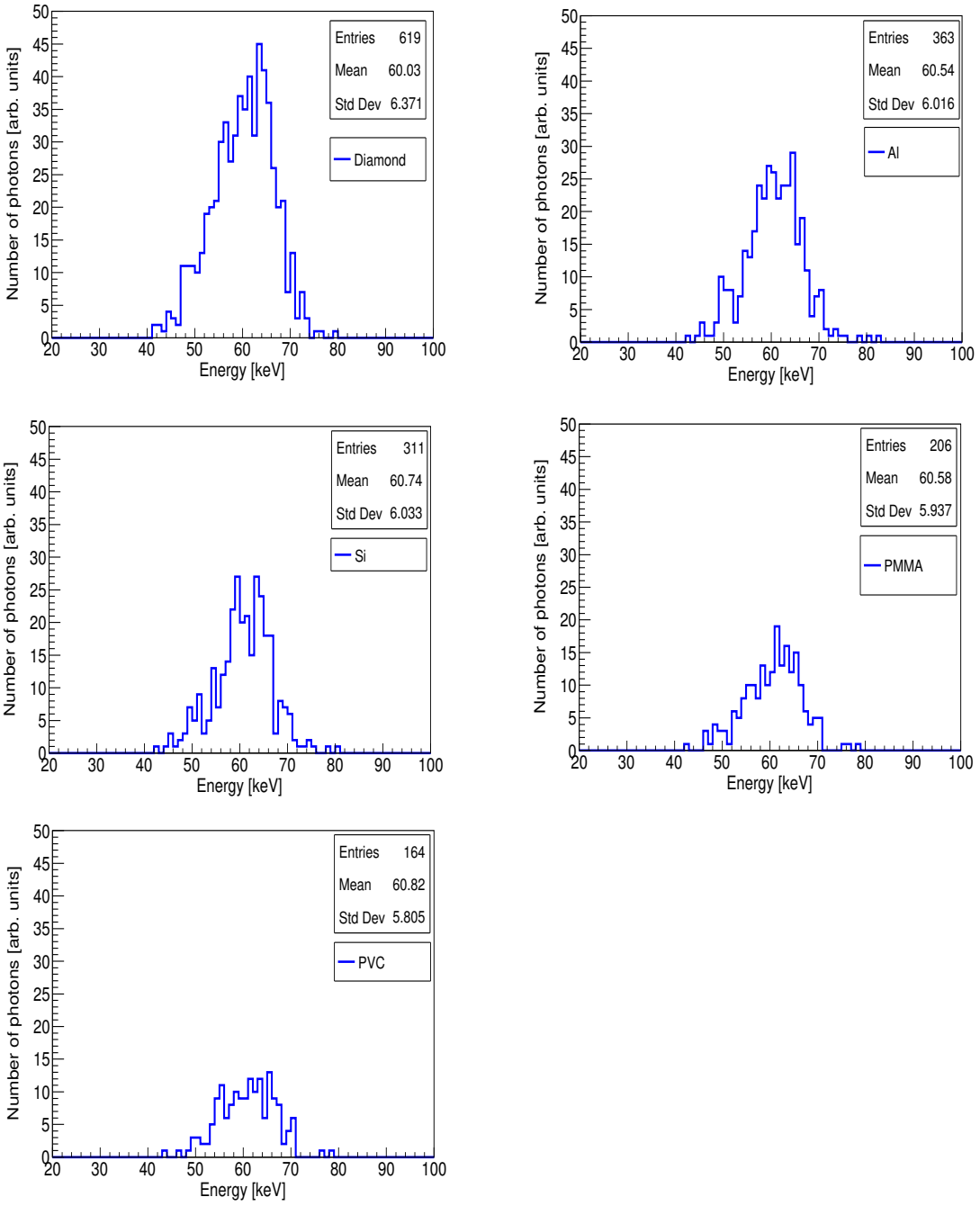

FIGURE 8.21: The number of Compton scattered photons and the energy in the detector for different crystals.

Chapter 9

Channeling Radiation Experiments

We performed CR experiments at the FAST facility in 2016. In this section, we first discuss specifications of the goniometer and the two X-ray detectors and the experimental conditions of the beam emittance and the beam optics, and then the experimental results are shown.

9.1 Setup for CR experiments

The goniometer for the CR experiments was installed between X120 and X121 (see Fig. 3.2). The goniometer stage can be rotated around vertical and horizontal axes and can slide horizontally. The movable target holder houses: (1) a clear aperture, (2) a diamond crystal, and (3) a 50 μm thick Al foil. The hole is used when the crystal is not needed. The diamond crystal is inserted when the CR experiments. Intercepting the beam with the foil generates bremsstrahlung that can be used to calibrate the detection system. The bremsstrahlung also provides a coarse calibration signal to center the beam on the foil and indirectly on the crystal as the foil and the crystal are inserted using a calibrated stepping motor. Figure 9.1 shows the goniometer. As we mentioned in chapter 8, quasi-monochromatic X-rays with an energy range of 50 keV-110 keV are radiated for ~43 MeV electron beams and the beam propagates parallel to the (110) plane in diamond. To detect X-rays with an energy of over 100 keV, we use two identical CdTe (Cadmium Telluride) detectors (Amptek Inc.) which can measure X-rays with an energy range of 5-150 keV. They are installed in the forward direction and at 90 degrees with respect to incident electron beams. Also, the two detectors are surrounded by radiation shielding using lead bricks to reduce the bremsstrahlung background from the

beam pipe and the diamond crystal. The layout of the CR experiments is shown in Figure 9.2.

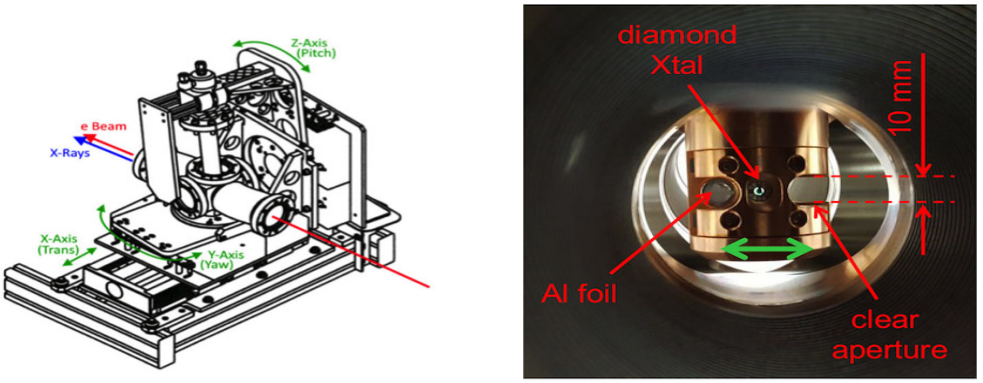

FIGURE 9.1: The goniometer with the Al foil and the diamond crystal, and the clear aperture installed in the beamline. Left and right figures represent appearance of the goniometer and the housing of the crystal in the goniometer, respectively.

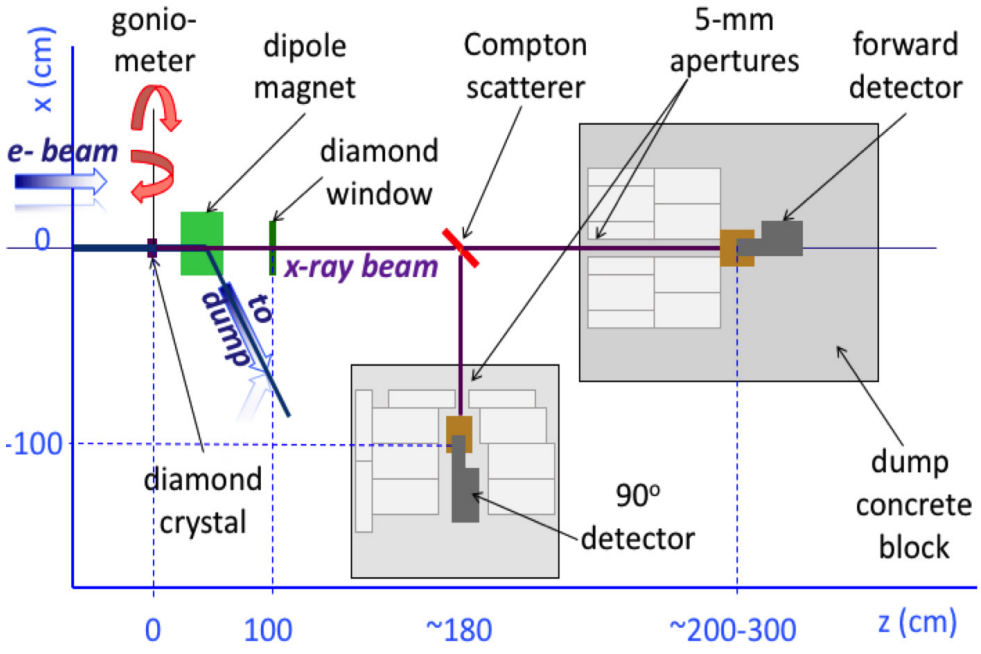

FIGURE 9.2: Layout of the CR experimental setup.

9.2 CR experiments

The electron beams produced at the photocathode are accelerated to ∼5 MeV in the RF gun. However, the dark current from the RF gun and the photocathode [112–114], measured with a Faraday cup placed between the RF gun and CC1, reaches into 5 μA at a beam energy of 4.3 MeV. Figure 9.3 shows the dark current as a function of the electron gun energy. The dark current could be suppressed to about 0.3 μA by reducing the accelerating voltage in the RF gun so that the electron beam energy after the gun was ∼3 MeV. However, that also caused emittance growth due to the space charge effect. We also inserted a gun collimator to dump as much dark current as we could, but the dark current at small transverse amplitudes was not reduced sufficiently. Since the main beam is accelerated with the on-crest RF phases in the CC1&2 cavities, the energy of the dark current should be smaller than that of the main electron beam after CC2. Therefore, we decided to scrape the dark current in the chicane using the difference of the energies between the dark current and the main electron beam.

The solenoid coils around the RF gun were tuned so that the beam emittances are minimized after CC2, and then the normalized beam emittances were (ε_x, ε_y)=(∼7.7 μm, ∼5.6 μm) at a charge of 200 pC. These beam emittances are larger than those for the simulation with ASTRA and THz experiments mentioned in Sec. 7.1 and 8.1. To be close to the ideal emittances, we need to tune the solenoid coils and the laser. The beam sizes ($\sigma_{x,y}$) need to be focused at the diamond crystal. Figure 9.4 shows the beta functions from CC2 to the beam monitor X121 (after the crystal) for the high brightness optics and the normal beam optics. The beam sizes at X120 (before the crystal) were focused to 160 μm from 1 mm in the normal optics. We inserted the diamond crystal in the beamline and measured photon counts with the two X-ray detectors varying the bunch

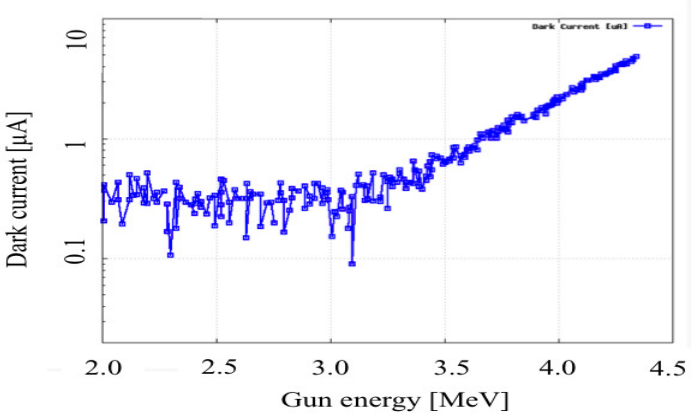

FIGURE 9.3: Dark current as a function of the gun energy.

charge. The results are shown in Figure 9.5. In the forward detector, the count decreased as the bunch charge was lowered to 50 fC. Reductions in the counts at the Compton detector were observed down to bunch charges of 10 pC. That can be interpreted to mean that the pile-up is caused mainly by the dark current since the photon countss did not fall at lower bunch charges. Therefore, we determined to use a bunch charge of 50 fC in operation which is a ultra-low bunch charge.

We sent electron beams through the chicane to suppressing the dark current from the diamond crystal and tried to detect channeling radiation. Figure 9.6 shows the radiation energy spectra measured with the forward (green dots) and the Compton (blue dots) detectors. In the forward detector, there are three sharp peaks at 75 keV, 90 keV, and 110 keV and a broad peak at 75 keV. From Fig. 8.14 in simulations, CR radiation should have three peaks at 50 keV, 70 keV, and 110 keV for a 43 MeV electron beam in the diamond crystal. The measured peaks are not consistent with those expected in simulations. In the Compton detector, there is a sharp peak at 75 keV, which is also not in agreement with the simulated results.

To identify where the peaks come from, GEANT4 simulations for materials of lead (radiation shielding), stainless steel (the beam pipe), Niobium (superconducting structures) were performed, and the result for the stainless steel is shown in Figure 9.7. In Fig. 9.7, the red line represents the spectrum measured in the Compton detector, and the blue line shows bremsstrahlung from stainless steel with a thickness of 1.7 mm. The observed

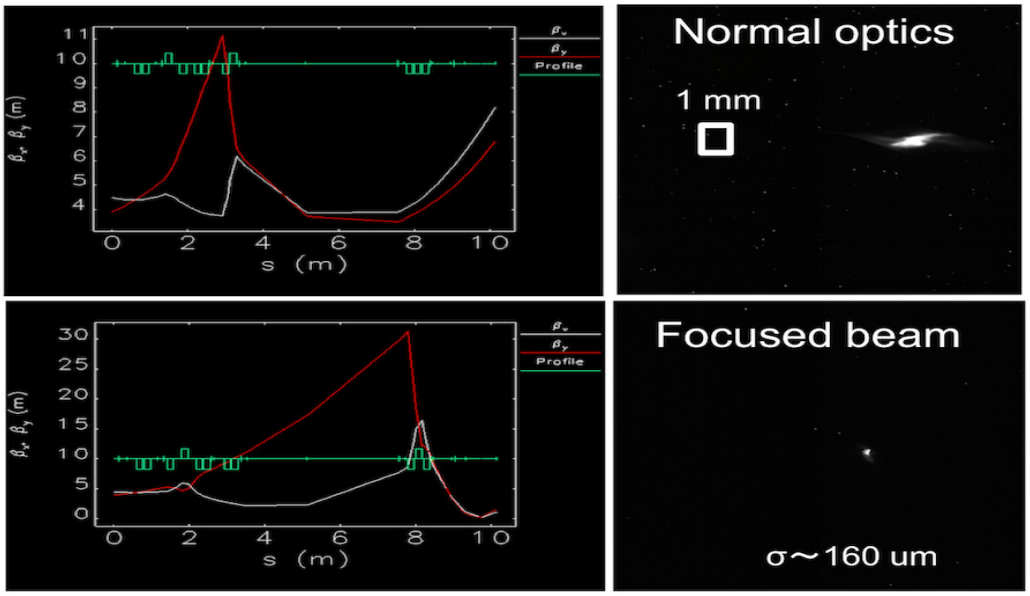

FIGURE 9.4: Beam optics before (upper) and after (bottom) the beam focus at the diamond crystal. Left plots shows the beta functions and right images are beam distributions at the beam monitor X120.

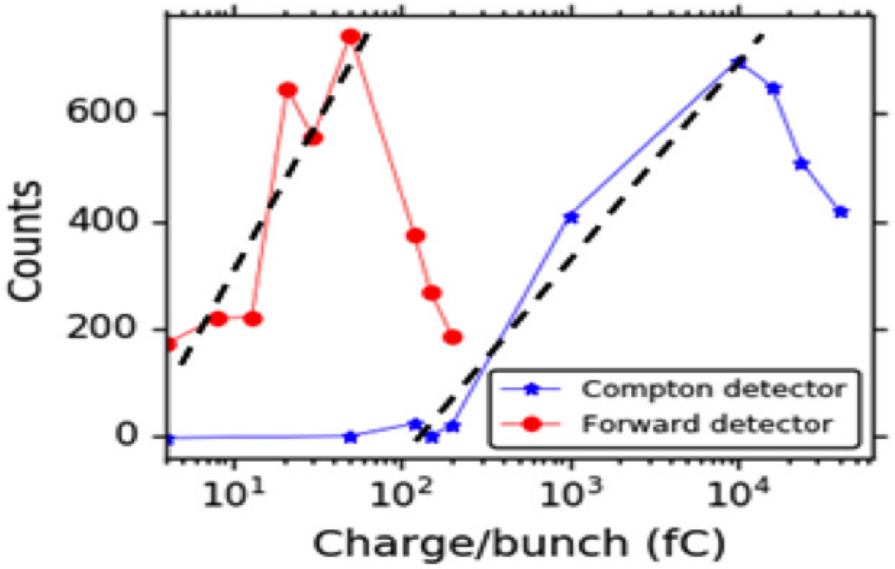

FIGURE 9.5: The two detector counts depending on a bunch charge current. Red and blue lines show the forward and the Compton detectors, respectively.

broad peak around 70 keV is consistent with the result from the GEANT4 simulations. Regarding the three sharp peaks, we checked the characteristic X-ray energies for each material [115]. Lead bricks, placed around the two detectors as radiation shielding, has the characteristic X-ray energy of 74.2 keV [115]. A sharp peak appears at about 75 keV in the forward X-ray detector, and it can be said that they are from the lead bricks around the X-ray detectors.

We checked that the charge loss of the main beam did not happen in the middle of the beamline using two current monitors installed after the RF gun and before the beam dump. Therefore, we think that bremsstrahlung with a broad peak at 75 keV was radiated from the beam pipe in the chicane hit by the dark current and goes into the two X-ray detectors. Also, the bremsstrahlung interacted with the radiation shielding of lead bricks around the two detectors, as a result the characteristic X-rays are emitted. Figure 9.8 shows the mechanism of the sharp and broad peaks at around 75 keV. The source of the other sharp peaks at 90 keV and 110 keV detected in the forward detector is not clear as there are no characteristic X-ray energies corresponding to the materials which are in the beamline.

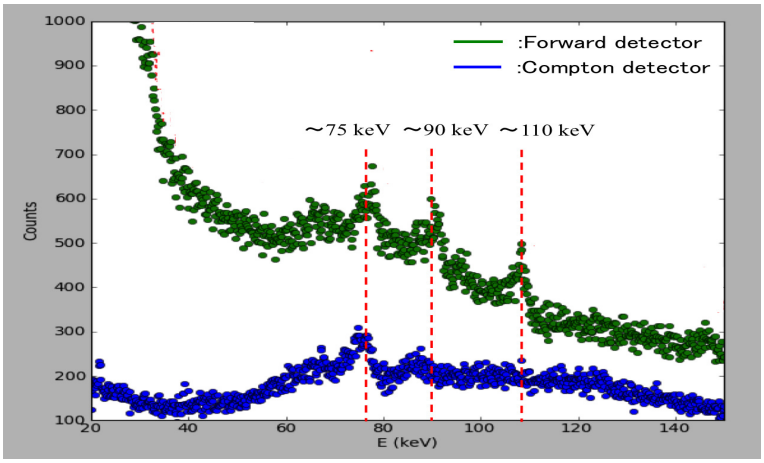

FIGURE 9.6: Radiation spectra measured with the forward (green dots) and the Compton (blue dots) detectors. The forward detector detected radiation with three peaks at 75 keV, 90 keV, and 110 keV. The Compton detector detected radiation with a peak at 75 keV on a broad peak around 75 keV.

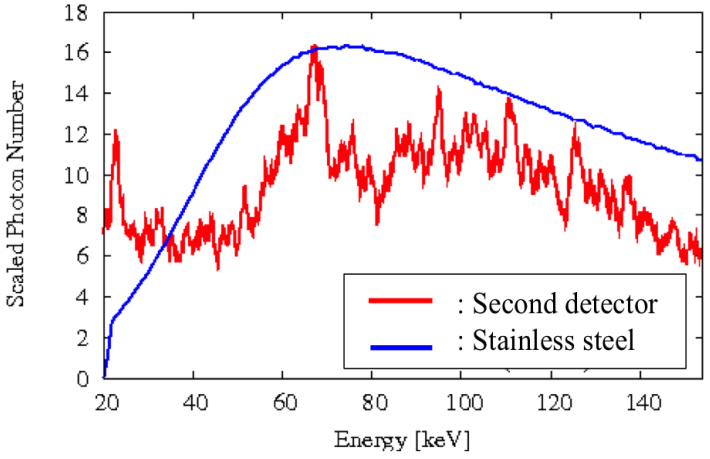

FIGURE 9.7: Radiation spectrum going into the Compton detector (red line) and bremsstrahlung spectra from the stainless steel with a thickness of 1.7 mm simulated with GEANT4.

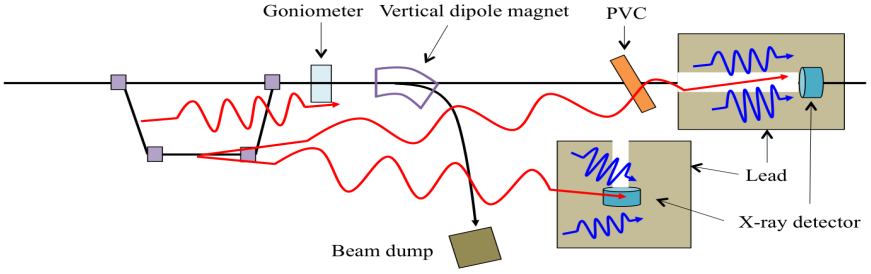

FIGURE 9.8: Bremsstrahlung (red lines) from the beam duct in the chicane and characteristic X-rays (blue lines) from lead going into the X-ray detectors.

9.3 Summary of CR experiments

We performed the CR experiments using 43 MeV electron beams at the FAST facility. The dark current was reduced to ∼5 μA after the RF gun. Although the dark current could be mitigated by reducing the accelerating voltage in the RF gun, the emittance growth was caused due to the space charge. Therefore, we suppressed the dark current in the chicane using the difference of the energies between the dark current and the main electron beam.

After the electron beam was focused to be below 160 μm at the diamond crystal, we scanned the bunch charge from a few fC to 20 pC and measured X-rays hitting the two CdTe detectors (forward and Compton detectors). The pile-up was caused at over 50 fC for the forward detector and at overt 10 pC for the Compton detector. Therefore, we performed CR experiments with the ultra-low charge of 50 fC.

We detected three peaks at 75 keV, 90 keV, and 110 keV with the forward detector. The expected energies are 51 (transition: 3→2), 67.5 (transition: 2→1), and 110 keV (transition: 1→0), and these measured energies except for 110 keV are different from the calculated energies. Also, the Compton detector detected photons with a broad peak at around 75 keV, which is also different from our expected energies.

To identify where the photon energies came from, we performed GEANT4 simulations with materials of lead (radiation shield around the detectors), Nb (superconducting cavity), and stainless steel (beam pipe). As a result, we concluded that the broad peaks at 75 KeV in the two detectors are from bremsstrahlung emitted from the stainless steel, and the sharp peak at 75 keV is from the characteristic X-rays of lead from [115]. We checked that the main electron beams could be sent to the beam dump without particle loss using the current monitor before the beam dump. Therefore, the dark current hits the beam pipe in the chicane and bremsstrahlung with a broad peak at 75 MeV are radiated. The bremsstrahlung passing through the lead shielding around the detectors enters the detectors. Moreover, the characteristic X-rays are emitted while the bremsstrahlung goes through the shielding and hit the forward detector.

Chapter 10

Conclusions

The purpose of this thesis is to propose and demonstrate a compact and frequency (energy) tunable THz/hard X-ray sources. We have described two radiation sources of THz radiation and hard X-ray through theory, simulations, demonstration experiments. Our proposed radiation sources can produce 1) narrow-band THz waves with a frequency of over 1 THz using a slit-mask and 2) quasi-monochromatic hard X-rays in an energy range from 40 keV to 110 keV, using a single diamond crystal at a 50 MeV class photo-injector with a magnetic chicane.

We create micro-bunched beams using the slit-mask installed in the chicane and generate THz radiation as CTR by sending the beam to an Al foil. The advantage of this method is that frequency can be controlled by varying the RF phases in accelerating structures.

We showed the theory and the simulations related to the production of micro-bunched beams and observing the micro-bunching on a transverse screen with a skew quadrupole magnet, and also presented the expected frequency spectra. As the result of the simulations, we found that narrow-band frequencies with 0.30 THz - 4 THz can be generated for an round beam ($\varepsilon_y/\varepsilon_x = 1$). When a flat beam with an emittance ratio of $\varepsilon_y/\varepsilon_x = 200$ is used, the intensity at the maximum frequency was increased.

The energy density generated from CTR is about 0.15 μJ/THz at the first harmonic frequency of $\sim$0.8 THz. To amplify the energy density, we considered the use of a small wiggler. When the micro-bunched beam passes through the wiggler, the energy density is about 500 times higher.

Moreover, we performed the demonstration experiments to verify the theory and simulations on the micro-bunched beams. The results of the experiments were in agreement with the theory and simulations. On the other hand, we could not obtain the

reproducible frequency spectra. By GEANT4 simulations, we identified that the cause is bremsstrahlung from the slit-mask and beam pipe. Therefore, for the upcoming THz radiation experiments, we will add radiation shielding and a new THz detector system which consists of a Michelson interferometer and a cryogenic bolometer which can sensitively measure THz radiation.

As for hard X-rays, we employed Channeling radiation (CR) which can generate the hard X-rays with a low energy electron beam. Although the yields of CR with ∼50 MeV electron beams has already simulated in [34], we simulated bremsstrahlung background from a diamond crystal, beam optics to emit the high yields and high brightness, and the X-ray detector system to avoid pile-up.

The expected energies of CR are 50 keV, 68 keV, and 110 keV, which comparable with the energies emitted at a few GeV class synchrotron radiation source. Also, to use CR as an imaging source, the photon yield of over 10^9 is required. The yield of CR is 10^8 photon/s at a bunch charge of 200 pC, therefore, for example, when a bunch charge of over 1 nC and a bunch frequency of 5 MHz are used in operation, the photon flux of over 10^9 photon/s can be achieved.

We performed the demonstration experiments of CR with 43 MeV electron beams, however, the expected energy spectrum could not be obtained due to the pile-up of the detectors. We did simulations with GEANT4 and identified that the X-ray detectors measured bremsstrahlung radiated from beam pipe caused by the dark currents, and also detected the characteristic X-rays of lead around the detectors emitted by the bremsstrahlung. For the next CR experiments, we need more radiation shielding around the detectors and around the chicane, or may need to put the detectors at other places.

Bibliography

[1] A.-S Muller and M Schwarz. An Introduction to Beam Physics. In *Synchrotron Light Sources and Free-Electron Lasers*. Springer, 2015.

[2] H. Hama, M Yasuda, M Kawai, F Hinode, K Nanbu, and F Miyahara. Intense coherent terahertz generation from accelerator based sources. *Nuclear Instruments and Methods A*, 637:557, 2011.

[3] S Antipov, SV Baryshev, R Kostin, S Baturin, J Qiu, C Jing, C Swinson, M Fedurin, and D Wang. Efficient extraction of high power THz radiation generated by an ultra-relativistic electron beam in a dielectric loaded waveguide. *Applied Physics Letters*, 109:142901, 2016.

[4] E Chiadroni et al. Characterization of the THz radiation source at the Frascati linear accelerator. *Review of Scientific Instruments*, 84:022703, 2013.

[5] G Lawrece Carr, Michael C Martin, Wayne R McKinney, K Jordan, George R Neil, and Gwyn P Williams. High-power terahertz radiation from relativistic electrons. *Nature*, 420:153, 2002.

[6] A Gopal et al. Observation of gigawatt-class THz pulses from a compact laser-driven particle accelerator. *Physical Review Letters*, 111:074802, 2013.

[7] S Antipov, M Babzien, C Jing, M Fedurin, W Gai, A Kanareykin, K Kusche, V Yakimenko, and A Zholents. Subpicosecond bunch train production for a tunable mJ level THz source. *Physical Review Letters*, 111:134802, 2013.

[8] Ziran Wu, Alan S Fisher, John Goodfellow, Matthias Fuchs, Dan Daranciang, Mark Hogan, Henrik Loos, and Aaron Lindenberg. Intense terahertz pulses from SLAC electron beams using coherent transition radiation. *Review of Scientific Instruments*, 84:022701, 2013.

[9] E Chiadroni et al. The SPARC linear accelerator based terahertz source. *Applied Physics Letters*, 102:094101, 2013.

[10] Siriwan Krainara, Toshiteru Kii, Hideaki Ohgaki, Sikharin Suphakul, and Heishun Zen. Development of Compact THz Coherent Undulator Radiation Source at Kyoto University. In *38th Int. Free Electron Laser Conf.(FEL'17), Santa Fe, NM, USA, August 20-25, 2017*, pages 158–161. JACOW, Geneva, Switzerland, 2018.

[11] P Piot, Y-E Sun, T.J Maxwell, J Ruan, A.H Lumpkin, M.M Rihaoui, and R Thurman-Keup. Observation of coherently enhanced tunable narrow-band terahertz transition radiation from a relativistic sub-picosecond electron bunch train. *Applied Physics Letters*, 98:261501, 2011.

[12] Masayoshi Tonouchi. Cutting-edge terahertz technology. *Nature photonics*, 1:97, 2007.

[13] Norihiro Sei, Hiroshi Ogawa, Takeshi Sakai, Ken Hayakawa, Toshinari Tanaka, Yasushi Hayakawa, and Kyoko Nogami. Millijoule terahertz coherent transition radiation at LEBRA. *Japanese Journal of Applied Physics*, 56:032401, 2017.

[14] S Casalbuoni, B Schmidt, P Schmüser, V Arsov, and S Wesch. Ultrabroadband terahertz source and beamline based on coherent transition radiation. *Physical Review Special Topics-Accelerators and Beams*, 12:030705, 2009.

[15] D Xiang and G Stupakov. Enhanced tunable narrow-band THz emission from laser-modulated electron beams. *Physical Review ST - Accelerators and Beams*, 12:080701, 2009.

[16] Z Zhang, L Yan, W Du, Land Huang, C Tang, and Z Huang. Generation of high-power tunable terahertz radiation from laser interaction with a relativistic electron beam. *Physical Review ST - Accelerators and Beams*, 20:050701, 2017.

[17] S. Antipov et al. IOTA (Integrable Optics Test Accelerator): facility and experimental beam physics program. *Journal of Instrumentation*, 12:T03002, 2017.

[18] Darren Crawford et al. First beam and high-gradient cryomodule commissioning results of the Advanced Superconducting Test Accelerator at Fermilab. In *Proceedings of IPAC2015*, page 1831, Richmond, VA, USA, 2015.

[19] Khalid Chouffani, Herbert Überall, Harald Genz, P Hoffmann Stascheck, Uwe Nething, and Achim Richter. Low energy channeling radiation experiments in a germanium crystal. *Nucl. Instrum. Methods Phys. Res., Sect. B*, 152:479–493, 1999.

[20] H Genz, L Groening, P Hoffmann-Stascheck, A Richter, M Höfer, J Hormes, U Nething, JPF Sellschop, C Toepffer, and M Weber. Channeling radiation of

electrons in natural diamond crystals and their coherence and occupation lengths. *Physical Review B*, 53:8922, 1996.

[21] RK Klein, JO Kephart, RH Pantell, H Park, BL Berman, RL Swent, S Datz, and RW Fearick. Electron channeling radiation from diamond. *Physical Review B*, 31: 68, 1985.

[22] W Wagner, B Azadegan, M Sobiella, J Steiner, K Zeil, and J Pawelke. An intense channeling radiation source. *Nucl. Instrum. Methods Phys. Res., Sect. B*, 266: 327–334, 2008.

[23] F Curtis Michel. Intense coherent submillimeter radiation in electron storage rings. *Physical Review Letters*, 48(9):580, 1982.

[24] T Nakazato, M Oyamada, N Niimura, S Urasawa, O Konno, A Kagaya, R Kato, T Kamiyama, Y Torizuka, T Nanba, et al. Observation of coherent synchrotron radiation. *Physical review letters*, 63(12):1245, 1989.

[25] X Su, D Wang, Q Tian, Y Liang, L Niu, L Yan, Y Du, W Huang, and C Tang. Widely tunable narrow-band coherent Terahertz radiation from an undulator at THU. *Journal of Instrumentation*, 13(01):C01020, 2018.

[26] P Muggli, V Yakimenko, M Babzien, E Kallos, and KP Kusche. Generation of trains of electron microbunches with adjustable subpicosecond spacing. *Physical Review Letters*, 101:054801, 2008.

[27] P Muggli, B Allen, VE Yakimenko, J Park, M Babzien, KP Kusche, and WD Kimura. Simple method for generating adjustable trains of picosecond electron bunches. *Physical Review Special Topics-Accelerators and Beams*, 13:052803, 2010.

[28] Jayakar Thangaraj and Philippe Piot. THz-radiation production using dispersively-selected flat electron bunches. *arXiv preprint arXiv:1310.5389*, 2013.

[29] JU Andersen, KR Eriksen, and E Laegsgaard. Planar-channeling radiation and coherent bremsstrahlung for MeV electrons. *Physica Scripta*, 24:588, 1981.

[30] RK Klein, JO Kephart, RH Pantell, H Park, BL Berman, RL Swent, S Datz, and RW Fearick. Electron channeling radiation from diamond. *Physical Review B*, 31 (1):68, 1985.

[31] M Gouanere, D Sillou, M Spighel, N Cue, MJ Gaillard, RG Kirsch, J-C Poizat, J Remillieux, BL Berman, P Catillon, et al. Planar channeling radiation from 54-110-mev electrons in diamond and silicon. *Physical Review B*, 38(7):4352, 1988.

[32] JO Kephart, BL Berman, RH Pantell, S Datz, RK Klein, and H Park. Thermal-vibrational amplitudes of silicon determined by channeling-radiation measurements. *Physical Review B*, 44(5):1992, 1991.

[33] M Gouanere, D Sillou, M Spighel, N Cue, MJ Gaillard, RG Kirsch, J-C Poizat, J Remillieux, BL Berman, Ph Catillon, et al. Sharp-line and broad-continuum radiation from electrons channeled in diamond. *Nuclear Instruments and Methods in Physics Research*, 194(1-3):225–228, 1982.

[34] Tanaji Sen and Christopher Lynn. Spectral brilliance of channeling radiation at the ASTA photoinjector. *Int. J. Mo Phys. A*, 29:1450179, 2014.

[35] D Mihalcea, DR Edstrom, P Piot, W Rush, and T Sen. Channeling Radiation Experiment at Fermilab ASTA. In *Proceedings of IPAC2015*, pages 95–98, Richmond, VA, USA, 2015.

[36] AA Vieira, Arlene Linke, Elisabeth Mateus Yoshimura, RA Terini, and Silvio Bruni Herdade. A portable compton spectrometer for clinical x-ray beams in the energy range 20–150 kev. *Applied Radiation and Isotopes*, 69(2):350–357, 2011.

[37] Martin Reiser. *Theory and design of charged particle beams*. John Wiley & Sons, 2008.

[38] Helmut Wiedemann. *Particle accelerator physics*. Springer, 2015.

[39] Shyh-Yuan Lee. *Accelerator physics*. World Scientific Publishing Company, 2011.

[40] Martin Berz, Kyoko Makino, and Weishi Wan. *An Introduction to Bream Physics*. CRC Press, 2015.

[41] Klaus Wille. *The physics of particle accelerators: an introduction*. Clarendon Press, 2000.

[42] Donald A Edwards and Michael J Syphers. *An introduction to the physics of high energy accelerators*. John Wiley & Sons, 2008.

[43] Michiko G Minty and Frank Zimmermann. *Measurement and control of charged particle beams*. Springer Science & Business Media, 2013.

[44] Peter Forck. Lecture notes on beam instrumentation and diagnostics. *Joint Universities Accelerator School (JUAS 2010)*, 2011.

[45] K Kubo. How to calculate "intrinsic" emittances from 4-dimensional beammatrix. *ATF99-02*, 1999.

[46] A Faus-Golfe, J Navarro, N Fuster Martinez, J Resta Lopez, and J Giner Navarro. Emittance reconstruction from measured beam sizes in ATF2 and perspectives for ILC. *Nuclear Instruments and Methods in Physics Research Section A: Accelerators, Spectrometers, Detectors and Associated Equipment*, 819:122–138, 2016.

[47] Eduard Prat and Masamitsu Aiba. Four-dimensional transverse beam matrix measurement using the multiple-quadrupole scan technique. *Physical Review Special Topics-Accelerators and Beams*, 17(5):052801, 2014.

[48] C Xiao, M Maier, XN Du, P Gerhard, L Groening, S Mickat, and H Vormann. Rotating system for four-dimensional transverse rms-emittance measurements. *Physical Review Accelerators and Beams*, 19(7):072802, 2016.

[49] B Dwersteg, K Flöttmann, J Sekutowicz, and Ch Stolzenburg. RF gun design for the TESLA VUV Free Electron Laser. *Nuclear Instruments and Methods in Physics Research Section A: Accelerators, Spectrometers, Detectors and Associated Equipment*, 393:93–95, 1997.

[50] M Krasilnikov, F Stephan, G Asova, H-J Grabosch, M Groß, L Hakobyan, I Isaev, Y Ivanisenko, L Jachmann, M Khojoyan, et al. Experimentally minimized beam emittance from an l-band photoinjector. *Physical Review Special Topics-Accelerators and Beams*, 15(10):100701, 2012.

[51] Aliaksei Halavanau, Jibong Hyun, P Piot, T Sen, D Mihalcea, and C Thangaraj. Magnetized and Flat Beam Experiment at FAST. Technical Report FERMILAB-CONF-17-172-APC, 2017.

[52] P Piot, CR Prokop, Y-E Sun, D Mihalcea, and BE Carlsten. Flat electron bunch compression at the advanced superconducting test accelerator. Technical Report FERMILAB-CONF-13-192-APC, 2013.

[53] J Zhu, P Piot, D Mihalcea, and CR Prokop. Formation of compressed flat electron beams with high transverse-emittance ratios. *Physical Review Special Topics-Accelerators and Beams*, 17(8):084401, 2014.

[54] CR Prokop, P Piot, BE Carlsten, and M Church. Beam dynamics performances and applications of a low-energy electron-beam magnetic bunch compressor. *Nuclear Instruments and Methods in Physics Research Section A: Accelerators, Spectrometers, Detectors and Associated Equipment*, 719:17–28, 2013.

[55] Paul J Emma. Bunch Compressor Beamlines for the Tesla and S Band Linear Colliders. Technical Report SLAC-PUB-10013, Stanford Linear Accelerator Center, Menlo Park, CA (US), 2003.

[56] P Emma, K Bane, M Cornacchia, Z Huang, H Schlarb, G Stupakov, and D Walz. Femtosecond and subfemtosecond X-ray pulses from a self-amplified spontaneous-emission–based free-electron laser. *Physical review letters*, 92(7):074801, 2004.

[57] M Schreck and P Wesolowski. Analytical bunch compression studies for a linac-based electron accelerator. *Physical Review Special Topics-Accelerators and Beams*, 18(10):100101, 2015.

[58] Pedro Castro. Beam trajectory calculations in bunch compressors of TTF2. Technical Report DESY-TECHNICAL-NOTE-2003-01, Dt. Elektronen-Synchrotron DESY, 2003.

[59] Dinh Cong Nguyen, John W Lewellen IV, and Leanne D Duffy. RF Linac for High-Gain FEL Photoinjectors. Technical Report LA-UR-14-23995, Los Alamos National Lab.(LANL), Los Alamos, NM (United States), 2014.

[60] John Byrd. Bunch Compressors. *UPSAS Lectures, June*, 2010.

[61] Philip Duke. *Synchrotron radiation: production and properties*, volume 3. Oxford University Press, 2009.

[62] Helmut Wiedemann. Synchrotron radiation. In *Particle Accelerator Physics*, pages 647–686. Springer, 2003.

[63] Ya S Derbenev, EL Saldin, VD Shiltsev, and J Rossbach. Microbunch radiative tail-head interaction. Technical report, 1995.

[64] M Borland. Simple method for particle tracking with coherent synchrotron radiation. *Physical Review Special Topics-Accelerators and Beams*, 4(7):070701, 2001.

[65] R Hajima. Emittance compensation in a return arc of an energy-recovery linac. In *Free Electron Lasers 2003*, pages 335–339. Elsevier, 2004.

[66] Simone Di Mitri and Max Cornacchia. Merit functions for the linac optics design for colliders and light sources. *Nuclear Instruments and Methods in Physics Research Section A: Accelerators, Spectrometers, Detectors and Associated Equipment*, 735:60–65, 2014.

[67] Ryoichi Hajima. A first-order matrix approach to the analysis of electron beam emittance growth caused by coherent synchrotron radiation. *Japanese journal of applied physics*, 42(8A):L974, 2003.

[68] Florian Lohl. Measurements of the transverse emittance at the VUV-FEL. Technical Report DESY-TESLA-FEL-2005-03, 2005.

[69] Jea Arthur, J Schmerge, R Tatchyn, A Fisher, T Kotseroglou, J Sheppard, K van Bibber, M Pietryka, ET Scharlemann, S Lidia, et al. Linac coherent light source (LCLS) design study report. Technical Report SLAC-0521, 1998.

[70] P Emma. Chirping the LCLS electron beam. Technical Report SLAC-TN-05-037, Stanford Linear Accelerator Center (SLAC), Menlo Park, CA, 2005.

[71] Simone Di Mitri. Bunch length compressors. *CERN Yellow Reports: School Proceedings*, 1:363, 2018.

[72] GEANT4. http://geant4.cern.ch.

[73] Kirk Bertsche, Paul Emma, and Oleg Shevchenko. A simple, low cost longitudinal phase space diagnostic. Technical Report SLAC-PUB-13614, Stanford Linear Accelerator Center (SLAC), 2009.

[74] Michael Borland. ELEGANT: A flexible SDDS-compliant code for accelerator simulation. Technical report, Argonne National Lab., IL (US), 2000.

[75] Y-E Sun, Philippe Piot, K-J Kim, Nikolas Barov, Steven Lidia, James Santucci, Rodion Tikhoplav, and Jason Wennerberg. Generation of angular-momentum-dominated electron beams from a photoinjector. *Physical Review Special Topics-Accelerators and Beams*, 7(12):123501, 2004.

[76] Ph Piot, Y-E Sun, and K-J Kim. Photoinjector generation of a flat electron beam with transverse emittance ratio of 100. *Physical Review Special Topics-Accelerators and Beams*, 9(3):031001, 2006.

[77] Kwang-Je Kim. Round-to-flat transformation of angular-momentum-dominated beams. *Physical Review Special Topics-Accelerators and Beams*, 6(10):104002, 2003.

[78] Yin-e Sun. Angular-momentum-dominated electron beams and flat-beam generation. Technical Report FERMILAB-THESIS-2005-17, Fermi National Accelerator Lab.(FNAL), Batavia, IL (United States), 2005.

[79] E Thrane, N Barov, D Mihalcea, Y Sun, K Bishofberger, D Edwards, H Edwards, S Nagaitsev, J Santucci, J Corlett, et al. Photoinjector Production of a Flat Electron Beam. In *Proceedings of XXI International Linac Conference*, 2002.

[80] Kwang-Je Kim. RF and space-charge effects in laser-driven RF electron guns. *Nuclear Instruments and Methods in Physics Research Section A: Accelerators, Spectrometers, Detectors and Associated Equipment*, 275(2):201–218, 1989.

[81] S Lederer, G Asova, JW Baehr, K Boyanov, C Boulware, HJ Grabosch, M Haenel, Y Ivanisenko, S Khodyachykh, S Korepanov, et al. Investigations on the Thermal Emittance of Cs2Te Photocathodes at PITZ. *Proceedings of FEL07, Novosibirsk, Russia*, 2007.

[82] Klaus Flöttmann. Note on the thermal emittance of electrons emitted by Cesium Telluride photo cathodes. Technical report, SCAN-9708052, 1997.

[83] Shaoheng Wang. Correction of nonlinear distortion in high-transverse-emittance ratio-beam production with linear accelerator. *Physical Review Special Topics-Accelerators and Beams*, 11(5):054201, 2008.

[84] A Murokh, JB Rosenzweig, M Hogan, H Suk, G Travish, and U Happek. Bunch length measurement of picosecond electron beams from a photoinjector using coherent transition radiation. *Nuclear Instruments and Methods in Physics Research Section A: Accelerators, Spectrometers, Detectors and Associated Equipment*, 410 (3):452–460, 1998.

[85] A Tremaine, J Rosenzweig, S Anderson, P Frigola, M Hogan, A Murokh, C Pellegrini, D Nguyen, and R Sheffield. Measured free-electron laser microbunching using coherent transition radiation. *Nuclear Instruments and Methods in Physics Research Section A: Accelerators, Spectrometers, Detectors and Associated Equipment*, 429(1-3):209–212, 1999.

[86] Y Liu, David B Cline, XJ Wang, M Babzien, JM Fang, and V Yakimenko. Microbunching diagnostics for the IFEL by coherent transition radiation. In *AIP Conference Proceedings*, volume 398, pages 664–672. AIP, 1997.

[87] Kwang-Je Kim. Characteristics of synchrotron radiation. In *AIP Conference Proceedings*, volume 184, pages 565–632. AIP, 1989.

[88] James A Clarke. *The science and technology of undulators and wigglers*. Number 4. Oxford University Press on Demand, 2004.

[89] Steven L Hulbert and Jill M Weber. Flux and brightness calculations for various synchrotron radiation sources. *Nuclear Instruments and Methods in Physics Research Section A: Accelerators, Spectrometers, Detectors and Associated Equipment*, 319(1-3):25–31, 1992.

[90] Lars Frohlich. Bunch length measurements using a Martin-Puplett interferometer at the VUV-FEL. Technical Report DESY-THESIS-2005-011, 2005.

[91] Marc Alexander Geitz. Investigation of the transverse and longitudinal beam parameters at the TESLA test facility linac. Technical Report DESY-THESIS-1999-033, 1999.

[92] R Thurman-Keup, G Kazakevich, and R.P Fliller. Bunch length measurement at the Fermilab A0 photoinjector using a Martin-Puplett interferometer. Technical report, FERMILAB-PUB-08-115-AD., 2008.

[93] Erik Bründermann, Heinz-Wilhelm Hübers, and Maurice FitzGerald Kimmitt. *Terahertz techniques*, volume 151. Springer, 2012.

[94] F-J Decker. Beam distributions beyond RMS. In *AIP Conference Proceedings*, volume 333, pages 550–556. AIP, 1995.

[95] R Thurman-Keup, AH Lumpkin, and J Thangaraj. Terahertz and optical measurement apparatus for the Fermilab ASTA injector. Technical report, Fermi National Accelerator Lab.(FNAL), Batavia, IL (United States), 2014.

[96] Darren Crawford et al. Measurement of coherent transition radiation in the THz region from extremely short electron bunch. In *Proceedings of the 13th Annual Meeting of Particle Accelerator Society of Japan*, page 19, Chiba, Japan, 2016.

[97] Pavel Evtushenko, James Coleman, Kevin Jordan, J Michael Klopf, George Neil, and GP Williams. Bunch length measurements at the JLab FEL using coherent transition and synchrotron radiation. In *AIP Conference Proceedings*, volume 868, pages 193–201. AIP, 2006.

[98] Randy Thurman-Keup, AH Lumpkin, and Jayakar Thangaraj. An optical and terahertz instrumentation system at the FAST linac at Fermilab. *arXiv preprint arXiv:1803.01026*, 2018.

[99] JU Andersen, E Bonderup, and RH Pantell. Channeling radiation. *Ann. Rev. Nucl. Part. Sci.*, 33:453–504, 1983.

[100] Behnam Azadegan. A Mathematica package for calculation of planar channeling radiation spectra of relativistic electrons channeled in a diamond-structure single crystal (quantum approach). *Comp. Phys. Comm*, 184:1064–1069, 2013.

[101] B Azadegan, L Sh Grigoryan, J Pawelke, and W Wagner. Investigation of planar electron channelling radiation generated in quartz single crystals. *Journal of Physics B: Atomic, Molecular and Optical Physics*, 41:235101, 2008.

[102] Behnam Azadegan. *Investigation of Planar Channeling Radiation on Diamond and Quartz Crystals at Electron Energies between 14 and 34 MeV and Probing the Influence of Ultrasonic Waves on Channeling Radiation.* PhD thesis, 2007.

[103] ASTRA. http://www.desy.de/∼mpyflo/.

[104] SAD. http://acc-physics.kek.jp/SAD/.

[105] Jackson. Classical Electrodynamics, 2001.

[106] Juerg Beringer, JF Arguin, RM Barnett, K Copic, O Dahl, DE Groom, CJ Lin, J Lys, H Murayama, CG Wohl, et al. Review of particle physics. *Phys. Rev. D*, 86:010001, 2012.

[107] Gerald R Lynch and Orin I Dahl. Approximations to multiple Coulomb scattering. *Nucl. Instrum. Methods Phys. Res., Sect. B*, 58:6–10, 1991.

[108] B Azadegan, W Wagner, and J Pawelke. Dependence of the linewidth of planar electron channeling radiation on the thickness of the diamond crystal. *Phy. Rev. B*, 74:045209, 2006.

[109] E. Bagli. Private communication, 2017.

[110] NIST. https://physics.nist.gov/PhysRefData/FFast/html/form.html.

[111] Robley Dunglison Evans and RD Evans. *The atomic nucleus*. McGraw-Hill New York, 1955.

[112] JH Han, J Bahr, H-J Grabosch, M Krasilnikov, V Miltchev, A Oppelt, B Petrosyan, S Riemann, L Staykov, F Stephan, et al. Dark current and multipacting in the photocathode rf guns at PITZ. In *Particle Accelerator Conference, 2005. PAC 2005. Proceedings of the*, pages 895–897. IEEE, 2005.

[113] L Monaco, P Michelato, C Pagani, P Pierini, D Sertore, JH Han, S Schreiber, DESY Hamburg, Germany M Krasilnikov, and F Stephan. Dark current investigation of FLASH and PITZ RF Guns. *EPAC06, Edinburgh, UK*, 2006.

[114] A Oppelt, K Abrahamyan, O Aldrian, G Asova, J Bähr, G Dimitrov, HJ Grabosch, L Hakobyan, J Ivanisenko, S Khodyachykh, et al. Tuning, conditioning, and dark current measurements of a new gun cavity at PITZ. *FEL06, Berlin, Germany*, 2006.

[115] Joyce Alvin Bearden. X-ray wavelengths. *Reviews of Modern Physics*, 39(1):78, 1967.